PEEL HERE

File

1

SOVIET ATOMIC ENERGY

АТОМНАЯ ЭНЕРГИЯ

(ATOMNAYA ÉNERGIYA)

TRANSLATED FROM RUSSIAN
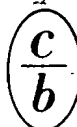
SOVIET ATOMIC ENERGY

SOVIET ATOMIC ENERGY

A translation of *Atomnaya Énergiya*

CONTENTS

Engl./Russ.

CONTENTS

(continued)

Engl./Russ.

STABILITY OF THE COOLANT CIRCULATION IN A MODEL OF THE AST-500 REACTOR

V. P. Zaval'skii, L. L. Kobzar',
P. A. Leppik, and V. V. Maimistov

UDC 621.039.55

The stability of the coolant flow rate is the most important factor for the reliable operation of the AST reactor (pressure vessels cooled by water in natural circulation conditions). The special features of this type of **reactors** are the relatively low pressure, considerable underheating of the water up to saturation at the core inlet, the low bulk steam content at the core outlet, and the high individual tractive sections above the fuel-element assemblies, which with **defined conditions** can lead to the onset of self-excited fluctuations of the coolant flow rate.

A considerable number of papers has been devoted to the problem of thermohydraulic stability in the Soviet and foreign literature (e.g., [1, 2]). A number of computational procedures exist, some of which have been used in numerical programs for computers [3, 4]. In the present paper, one of the possible species of instability is considered — general circuit thermohydraulic instability. The purpose of the investigations carried out was to obtain experimental data in conditions maximally approximating natural, and to confirm the existing computational procedures and programs.

In order to conduct the experimental investigations, a large-scale model of the natural circulation circuit of the AST-500 reactor (model AST-500) was built in the I. V. Kurchatov Institute of Atomic Energy. The height of the model corresponds to the height of the reactor, but the surface areas of the straight-through sections of the parts of the circulation circuit are reduced in it by a factor of approximately 300.

The AST-500 model is one of the experimental parts of the KS test rig [5]. The primary circuit of the test rig serves as the secondary circuit of the model. The primary circuit of the model is the coolant natural circulation circuit. Model AST-500 (Fig. 1) incorporates a rising section and two descending lines. In moving upwards, the coolant passes successively through the heat release zone 1 and a tractive section consisting of the simulators of the individual 2 and common tractive sections 3, and enters the overflow zone 4. Here separation of the coolant phases takes place: The liquid, through the overflow pipe 5, enters the built-in heat exchangers 8 and descends through the pipelines 10 to the inlet to the heat release zone; the steam rises into the pressure compensator 6, and thence, through the steam pipes 7, it moves to the condenser sections of the heat exchangers 8, located above the level of the phase separation.

The heat release zone of the model is represented by a bundle incorporating 61 elements: 55 fuel-element simulators and six control and safety rods. The former are made of tubes with an outside diameter of 13.5 mm, and the latter are unheated rods with a diameter of 18 mm. The arrangement of the elements in the bundle is staggered and the distance between their centers is 17.8 mm. The "above-key" diameter of the bundle is 143 mm and the surface area of the straight-through section is 8313 mm^2. The length of the heat release zone is 3 m.

In the tractive section — a tube with an internal diameter of 197 mm and a length of ∿7 m — a special impeller (of plates and blind tubes) is located, by means of which the individual tractive section of the fuel-element assembly of the AST-500 reactor is simulated. The pressure compensator is made of tubes with an internal diameter of 295 mm and a length of more than 4 m.

In the heat exchangers, the water of the secondary circuit 9 circulates through the Field tubes. The primary circuit coolant is in the intertube space. The surface area of the straight-through section of the heat exchanger is 8920 mm^2 and the overall height is 7.5 mm. The internal diameter of the steam pipelines and descending pipes is 96 mm. A Venturi nozzle 11 is installed in the descending pipelines, which serves for measuring the coolant flow rate, and also renewable throttling disks 12. Four types of disks were used in the ex-
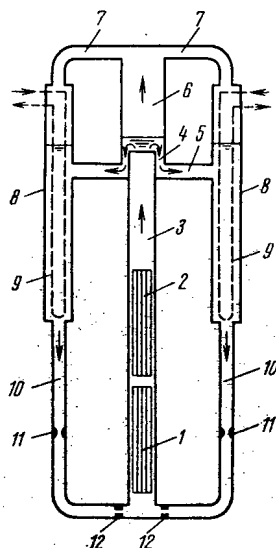
Fig. 1. Diagram of model AST-500.

periments. The data for the disks, with diameters of the transfer openings of 48 and 32 mm, will be given below. For the former disk, the hydraulic resistance coefficient ξ, scaled to the average coolant velocity in the descending pipeline, is equal to 16.6, and for the latter it is 98. The total height of the model exceeds 15 m.

The experimental investigations of the stability of the coolant circulation were conducted in the following way. With a constant pressure P, different combinations of the water temperature at the inlet to the heat release zone t_{in} and the power of the electric heater N (with simulation of the nominal regime of the AST-500 reactor, N = 1600 kW) were created. For each version of the geometry (hydrodynamic characteristics) of the circulation circuit, specified values of the coolant flow rate and the equilibrium bulk steam content (relative enthalpy) at the outlet from the heat release zone, x_{out}, correspond to the three regime parameters; P, t_{in}, and N. The type of regime (stable or unstable) was determined by the results of visual observation for the readings of two pen recorders of the type KSD, which record the flow rate of the water in the descending pipeline.

In the case of large negative values of x_{out}, when the water was in the single phase state in the whole of the circuit, the circulation was always stable. With increase of x_{out} and with increase of N or t_{in}, the natural circulation flow rate increased. With certain combinations of N and t_{in}, entry into the region of instability was recorded. The boundary values were assumed to be the values of the parameters for which periodic fluctuations of the flow rate developed, with amplitude A, amounting to ∿3% of its average value. Fluctuations with this relative amplitude could be distinguished visually on a background of hf pulsations with a smaller amplitude. With further increase of x_{out}, the value of A started to increase, and then, after reaching a maximum, it decreases to a value comparable with the amplitude of the hf pulsations. Examples of the dependence of the amplitude of the flow rate pulsations A and x_{out} are shown in Fig. 2.

In the course of the experiments, performed over a wide range of values of the regime parameters (in the article the experimental and calculated data are given only for P = 2 MPa), regions were detected which characterized a significant coolant flow rate instability. The relative amplitude of the coolant flow rate fluctuations attained 40% in individual regimes. With increase of the degree of throttling of the flow before the heat release zone, the value of A decreased markedly (with the value of x_{out} remaining unchanged). After installing disks with a diameter of the transfer opening of 27.7 mm ($\xi \approx 200$), no unstable regimes, in general, could be recorded.

For the graphical representation of the region of instability it is convenient to plot the value of x_{out} along one of the coordinate axes — the principal parameter determining the circulation instability. Examples of the region of instability are shown in Fig. 3 in the coordinates x_{out}, N. The values of x_{out} at the limits of instability were found by means of extrapolation of the averaged lines of the function $A(x_{out})$, similar to those shown in Fig. 2, before intersection with the abscissa axis (from the tangent at points with A = 3%). The region of instability in the coordinates x_{out}, N has the shape of a wedge, which enlarges with

Fig. 2

Fig. 3
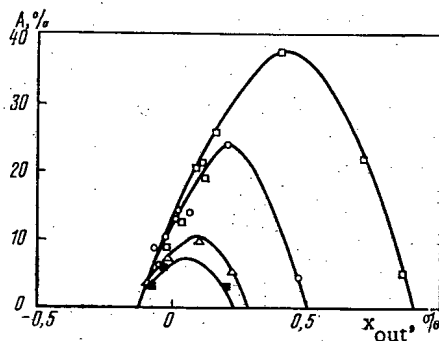
Fig. 2. Dependence of the amplitude of the coolant flow rate fluctuations on the steam content at the end of the heat release zone, for $N = 2000$ (□), 1600 (○), and 1200 (△) kW (a disk with diameter of the transfer opening 48 mm) and 2000 (■) kW (a disk with diameter of the transfer opening 32 mm).
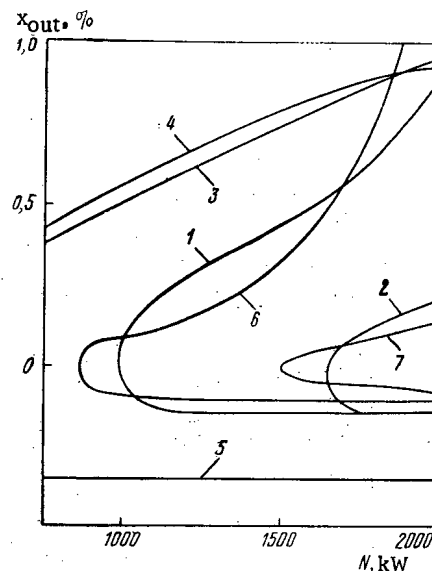
Fig. 3. Boundaries of the regions of stable and unstable regimes: 1, 2) experiment for disks with diameters of the transfer openings of 48 and 32 mm, respectively; 3, 4) calculation [6, 7] of the uper boundary of instability for disks with diameters of the transfer openings of 48 and 32 mm; 5) calculation [6, 7] of the lower boundary of instability from the data of an analysis of the static characteristics for disks with diameters of the transfer openings of 48 and 32 mm.

increase of N. The lower and upper side of the wedge will be designated the lower and upper instability boundaries, respectively. Between them is located a region of unstable regimes, and beyond the upper and lower boundaries there are regions of stable regimes.

An important problem of the investigations was the verification of the computational program RUKKRETS-1 [6, 7], designed for the analysis of the instability of pressurized boiling reactors and which allows the boundaries of regions of linear instability to be determined, and also the characteristic periods of pulsations. Before the numerical analysis of the circulation stability in the AST-500 model, it was necessary to verify and, in case of necessity, to refine the empirical relations containing in the program: the relations for calculating the bulk steam content, taking account of the nonequilibrium steam in the heat release zone and at the start of the tractive section; the relations for calculating the true volume steam content; and also certain formulas used in the thermohydraulic calculation of the circulation circuit. With correction of these relations, coincidence was ensured with the experimental data of the calculated values of the true volume steam contents, pressure drops in individual sections of the circuit, and the resulting characteristics — the natural circulation flow rate. It will be supposed below that the calculated and experimental values of the natural circulation flow rate and, consequently, also the value of x_{out} with given values of P, N, and t_{in}, coincide.

A comparison of the results of the calculation by the RUKKRETS-1 program with the experimental results shows that the theoretical region of linear instability is wider than the region of the instability regimes in practice (see Fig. 3). In this case the divergence in the boundary of these regions is the more significant, the greater the degree of throttling of the flow at the inlet to the heated zone and the less the thermal loading. The reason for this divergence (up to 0.5% for x_{out}) obviously consists in that with increase of ξ and decrease of N, the amplitude of the periodic coolant flow rate self-fluctuations in the unstable regimes decreases. The appearance of these self-fluctuations on the background of random pulsations of the coolant flow rate, which are natural for regimes with boiling, becomes

641
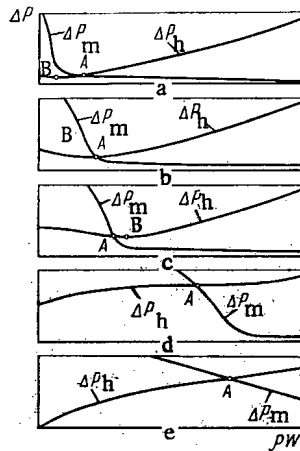
Fig. 4. Dependence of the total hydraulic resistance of the circulation circuit ΔP_h and the motive pressure heat ΔP_m on the mass coolant velocity ρw in the case of a constant heat release intensity: A is the point corresponding to the natural circulation regime; B is the minimum of the function $\Delta P_h(\rho w)$; a-e) $t_{in_1} < t_{in_2} < \ldots < t_{in_5}$; a) stable regime with low values of t_{in}; b) lower boundary of stability; c) unstable regime; d) upper boundary of stability; e) stable regime with high values of t_{in}.

inconvenient. For a more accurate determination of the agreement between the calculated boundary of linear instability and the experimental data, it is necessary to involve special statistical methods.

In the experiments conducted, the period of the flow rate fluctuations amounted to 7-39 sec. It decreased with increase of x_{out} and it increases with increase of the hydraulic resistance of the circulation circuit. The calculated values of the period of the flow rate fluctuations, determined by the RUKKRETS-1 program, coincide well with the experimental data. The relative deviation does not exceed 30%.

In addition to the verification of the RUKKRETS-1 numerical program, an attempt was made to relate the estimate of the circulation stability with certain special static hydraulic characteristics of the circuit. In order to determine the hydraulic characteristics, the components of the pressure drop over the whole circuit were calculated for values of the coolant flow rate close to the ideally possible for natural circulation. Two parameters were considered: the hydraulic characteristics of the circulation circuit — the dependence on the coolant flow rate of the sum of the hydraulic losses over the closed circuit (losses caused by friction and local resistances) — and the characteristics of the "motor" — the dependence of the coolant flow rate of the motive pressure head, determined by the difference in the weights of the coolant columns in the descending and ascending lines. The point of intersection of these characteristics determines the natural circulation flow rate.

An analysis of the static hydraulic characteristics of the circulation circuit of the model showed that on the graph for the unstable regimes recorded in the experiments, the point of intersection of the hydraulic characteristics curve and the line of motive pressure heads, determining the natural circulation regime, is located on the descending section of the hydraulic characteristics curve (Fig. 4). For the ascending section of the hydraulic characteristics curve, stable natural circulation regimes are characteristic. At the lower boundary of stability, the point of intersection A (see Fig. 4) coincides with the point of the minimum of the hydraulic characteristic curve B. At the upper boundary of stability, the hydraulic characteristic curve is "straightened out" (the "bulging" vanishes).

It follows from Fig. 4 that the region of instability, found on the basis of the analysis of the static hydraulic characteristics of the circulation circuit, coincides satisfactorily with the region of instability yielded by the experimental determination.

It should be noted that the empirical dependence of the circulation stability on the special features of the static hydraulic characteristics of the circuit obtained has been established only for the experimental model considered and cannot pretend to be generalized.

The investigations conducted allow the following conclusions to be drawn:

with a defined combination of regime parameters in the model AST-500 reactors, a general-circuit thermohydraulic instability begins;

by means of a change of the stream content of the coolant at the outlet from the heat release zone and the degree of throttling of the flow ahead of it, stable regimes can be maintained both for power of the electrical heating corresponding to nominal reactor power of the AST-500, and with lesser and higher thermal loadings;

the RUKKRETS-1 program [6, 7], with the static relations corrected by the results of the experiment, for the true values of the steam content gives a satisfactory representation of the boundaries of the region of unstable regimes in a large-scale model of the AST-500, and a quite good forecast of the possible periods of fluctuations of the coolant flow rate. The specified conservatism in the estimates of the width of the region of unstable regimes (up to 0.5% on α_{out}) obviously can be justified by the necessity of having certain engineering problems with respect to power when designing the facilities;

an estimate is possible of the instability of the coolant circulation in the AST-500 model by means of an analysis of the special features of the static characteristics of the circuit;

when using the results obtained, it is necessary to take into account that in actual facilities there is a height and radial nonuniformity of heat release in the core, and also a quite powerful interaction between the thermohydraulic and neutron-physical processes. In consequence of this, the upper boundary of the region of instability with respect to x_{out} is shifted relative to that which is obtained in conditions where heat release is nonuniform over the height and constant in time (see [4] for more detail).

LITERATURE CITED

1. F. M. Mitenkov et al., At. Energ., 52, No. 4, 227 (1982).
2. K. Fukuda and T. Kobori, in: Proceedings of the Sixth International Heat Transfer Conference, Toronto, Vol. 1 (1978), p. 369.
3. I. I. Morozov and V. A. Gerliga, Stability of Boiling Facilities [in Russian], Atomizdat, Moscow (1969).
4. V. I. Plyutinskii and P. A. Leppik, At. Energ., 47, No. 6, 363 (1978).
5. V. A. Kapustin et al., Preprint IAÉ-2347, Moscow (1974).
6. P. I. Leppik et al., Preprint IAÉ-3576/5, Moscow (1982).
7. P. A. Leppik et al., Preprint IAÉ-3667/5, Moscow (1982).

STATE-OF-THE-ART AND DEVELOPMENT PROSPECTS IN RADIATION TESTING

V. A. Kuprienko, N. V. Markina,   UDC 621.039.531:539.083
and V. A. Tsykanov

Developments in nuclear power have stimulated research on radiation testing of materials. Numerous methods and devices have been devised during the last decade [1], particularly for researching the radiation resistance of individual materials and components in nuclear engineering, which have provided a basis for some models for the behavior of materials under irradiation.

Particular efforts have been devoted to methods of improving the performance in tests within reactors or after irradiation, since these govern [2] not only the practical value of the results, but also the reliability. In part the problem can be handled by optimal metrological support to experiments.

Here we propose ways of evaluating the level of metrological support to radiation testing and make recommendations on improvements. The methods and devices for radiation testing have been devised as problems in material science have arisen, and in most cases the provision of universality and the optimization of developments have not been decisive. For this reason, there are many examples of different realizations of a single method in different reactors, and also of different methods used to examine some one property.

For example, the thermal conductivities of nonfissile materials are measured in several ways, particularly by means of unbounded planar layers [3-5], radial heat fluxes [6, 7], and Kohlrausch's method [8]. In studies on the thermophysical characteristics of fuel pins, the thermal power is estimated from the temperature rise and the flow of coolant [5], or else from

643
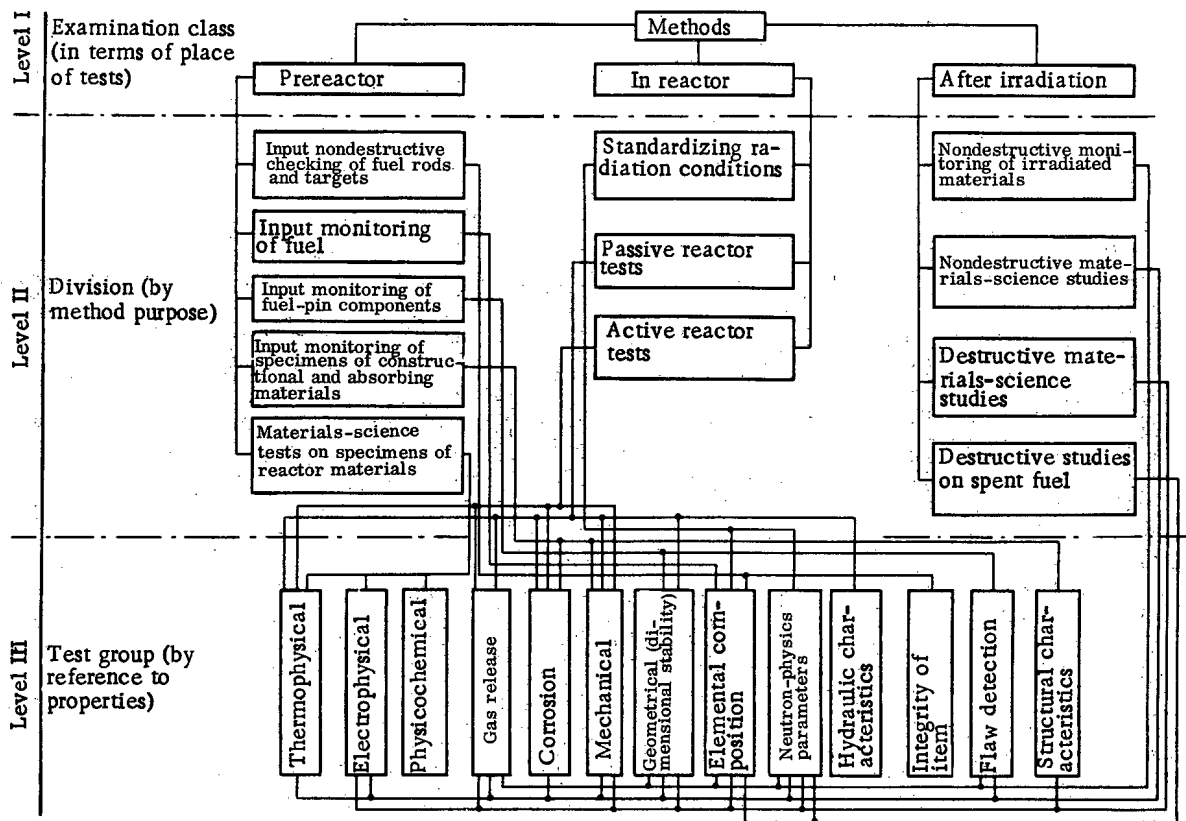
Fig. 1. Structure of the catalog of radiation-test methods.

the use of a heat meter [6, 9] or from neutron-physics measurements [10]. These examples indicate that there are many different approaches to test methods and that it is necessary to analyze the sufficiency and necessity of subsequent developments.

Apart from the need to expand radiation test facilities, there are some objective reasons for the differences in the methods used:

1) the specific features of testing in reactors of different types;

2) the extent to which reactors are equipped with monitoring and measuring equipment;

3) the absence of universal test methods;

4) the delays in distributing information on methods that have been developed;

5) the lack of criteria for comparing methods;

6) the lack of criteria for optimizing the number of developments.

In the period when it was necessary to accumulate data on the radiation resistance of materials and items used in nuclear engineering, it was justified to develop radiation-test methods by expanding the range of methods. At the present time, primary importance attaches to ensuring representativeness, comparability, and reliability in the results from different studies. This requires systematization of existing radiation-test methods (e.g., in the form of a catalog) to provide a general conception of the available range of methods and to evaluate the level of development in radiation-test methods, as well as to identify problems for which no appropriate methods exist and to determine ways of optimizing the number of methods and of upgrading the metrological support. The question of cataloging can be handled when all the necessary types of test have been clearly classified, i.e., when the catalog structure has been defined.

A three-level structure is proposed (Fig. 1). The headings list constitutes a scheme in which three classes of research are distinguished (prereactor ones, ones within reactors, and after irradiation), which is followed by division into sections corresponding to the purposes. Within each section one can realize various groups of tests in accordance with the property. The basis for the headings list will now be discussed.

644
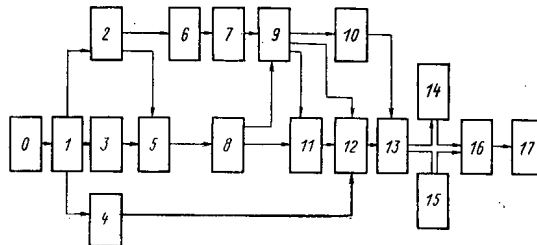
Fig. 2. Scheme for planning operations in the comparison of
radiation-test methods: 0) start, with target formation; 1)
choice of properties to be examined; 2) parameter list; 3)
method list; 4) demonstration of desirability of in-reactor
experiments; 5) classification of methods by purpose; 6) first
version of methods cards; 7) first form of catalog; 8) defi-
nition of criteria for comparing methods; 9) comparison of
methods; 10) classification of methods on accuracy parameters;
11) experimental comparison of methods; 12) determination of
application limits; 13) final decision on existing methods;
14) second version of methods cards; 15) method standardiza-
tion; 16) catalog editing; 17) end: catalog formation.

In radiation materials science, the research needs exhaustive information, i.e., a knowledge of the properties of the materials or items before, during, and after irradiation, which enables one to evaluate the radiation resistance and to define the mechanism of the behavior under irradiation. In this connection, there should be three classes of tests in the catalog: prereactor ones, ones within reactors, and those after irradiation (level I).

To determine the content of level II, we consider the logic of the tasks in each class of tests. The prereactor tests are intended to check the basic properties of materials and items, i.e., to establish, on the basis of the definitions of GOST 16504-74, that the re- quired parameters are within preset limits. Many of these studies are performed by nonde- structive methods. In many of these methods, precise measurement is applied only to one param- eter selected by the researcher, with the other parameters acting as controls.

Figure 1 shows the division within level II for prereactor tests, which arises from the essential differences in examining different objects (e.g., a finished fuel pin or raw fuel) in realizing the input checks (first four divisions). A small group of prereactor methods (materials-science tests on specimens of reactor materials) is intended for exact determina- tion of the characteristics or parameters under given conditions. From published data, we can see that these tests are either ones on reference specimens or parallel laboratory studies under identical conditions but without the action of ionizing radiation.

The group of in-reactor methods is intended to identify the irradiation conditions (flux- density measurement, spectrum, neutron fluence, etc.), in which the materials are irradiated at definite temperatures with appropriate neutron-physics conditions to the necessary neutron fluence, and there the required properties are examined after irradiation (reactor working-life tests), as well as to study the properties of materials and articles directly under the action of ionizing radiation and in the presence of other forms of loads, e.g., electrical, thermal, and mechanical ones. Then in accordance with the definition of GOST 16504-74, the tests per- formed by means of in-reactor methods belong to the test class (not monitoring), since they involve the experimental determination of **quantitative or qualitative characteristics.**

Tests after irradiation are intended to check properties and to examine the irradiated objects. Destructive tests are associated either with chemical methods of analysis or with disruption of the specimens in order to determine the limiting values of certain parameters or for other materials-science purposes.

Level III is common to all methods of measurement, testing, and monitoring, and it re- flects the detailed properties, parameters, or characteristics for any experiment. Level III makes operation with the catalog more flexible and provides for unambiguous method identifica- tion. The list of properties and characteristics given for this level in Fig. 1 is not to be considered as final and can be modified after the consideration of the methods to be included in the catalog.

Then, in our opinion, a three-level structure for the catalog enables one to formulate groups of methods correctly in terms of purposes and then to extend the analysis within the individual topics. When the information concentrated in the catalog is available, it will be possible to perform metrological evaluation of the existing set of methods in order to compare the accuracy characteristics and to optimize the number and quality of the parameters measured.

The scheme of Fig. 2 is used in comparing the methods and in generating the catalog. Comparative tests enable one to improve the metrological support, since they provice criteria for comparing methods (on accuracy, universality, reliability, etc.), and recommendations can be made on certification or standardization. Basic specifications for conducting the tests can also be drawn up for use in handling new tasks.

Therefore, metrological evaluation of existing methods enables one to guarantee unity in measurements involved in radiative tests on materials and items for nuclear engineering in reactors and in materials-science laboratories. To upgrade the metrological support to radiation tests, it is best to envisage comparative experiments in which the reliability of the results obtained by different methods is evaluated, along with the certification and standardization of methods that may be widely used in reactors of various types and the definition of methods for new purposes.

LITERATURE CITED

1. V. A. Tsykanov and B. V. Samsonov, Techniques for Irradiating Materials in High-Flux Reactors [in Russian], Atomizdat, Moscow (1973).
2. E. L. Broide, Izmer. Tekh., No. 3, 10 (1981).
3. A. G. Kharlamov, Measurement of the Thermal Conductivities of Solids [in Russian], Atomizdat, Moscow (1973).
4. V. A. Tsykanov, B. V. Samsonov, and V. M. Makhin, Preprint NIIAR-44 (452), Dimitrovgrad (1980).
5. V. A. Tsykanov et al., in: Proceedings of the All-Union School on In-Reactor Examination Methods [in Russian], Dmitrovgrad (1978), p. 213.
6. D. Clough and T. Sayers, AERE-R 4690, Harwell (1966).
7. N. V. Markina et al., Preprint NIIAR-48 (501), Dimitrovgrad (1981).
8. L. G. Gurvich and Sh. G. Makhkalov, Izv. Akad. Nauk Ukr. SSR, No. 5, 70 (1970).
9. B. Fitts, F. Miller, and P. Box, Nucl. Technol., 21, 26 (1974).
10. H. Ranm, C. Bronner, and W. Krebs, ibid., 29, 428 (1976).

SIZE CHANGES IN ZIRCONIUM ALLOY COMPONENTS IRRADIATED TO A HIGH FLUENCE

IN AN SM-2 REACTOR

V. A. Tsykanov, E. F. Davydov, V. A. Kuprienko,   UDC 621.039.534:546.831
V. K. Shamardin, A. S. Pokrovskii, G. P. Kobylyanskii,
V. M. Kosenkov, and Yu. D. Goncharenko

Components made of zirconium alloys may change in size and shape when used in reactor cores. One of the reasons is the radiation swelling in the alloy, which is essentially anisotropic and is dependent on the texture, and which occurs in the absence of external stresses (in contrast to radiation creep). The radiation swelling is affected by various factors: metallurgical features of the alloys, the deformation conditions during production, the neutron fluence, and the irradiation temperature [1, 2].

Here we present studies made on strips of $Zr + 1\%$ Nb alloy in the state after 20% cold deformation together with results on a central channel made of $Zr + 2.5\%$ Nb alloy in the annealed state, which were irradiated for a long time in the core of the SM-2 high-flux reactor at about 373°K.
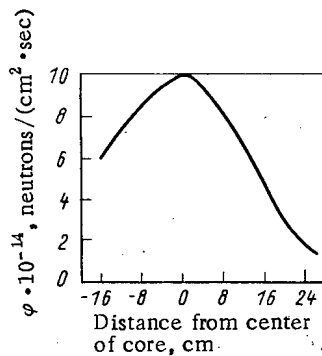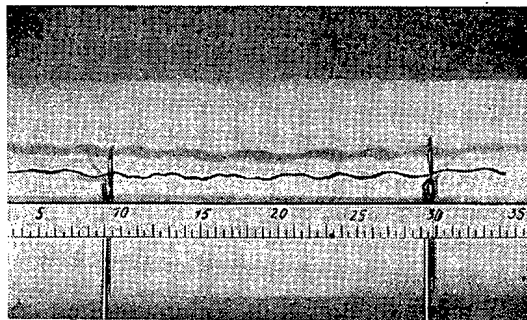
Fig. 1

Fig. 2

Fig. 1. Distribution of fast neutron flux density (E > 0.1 MeV) over the height of the central channel.

Fig. 2. Appearance of part of strip after irradiation to a fluence of $5.3 \cdot 10^{22}$ neutrons/cm^2 (E > 0.1 MeV).

The central channel in the SM-2 reactor is a tube of outside diameter 98.2 mm, wall thickness 6 mm, and length about 1000 mm, made of Zr + 2.5% Nb alloy anealed at 823°K for 5 h. The lower part of the channel of length 350 mm was in the reactor core. Figure 1 shows the neutron flux density distribution over the height of the channel. The neutron fluence in the plane of the core center was ∿9.1·10^{22} neutrons/cm^2 for the channel (E > 0.1 MeV). Four strips of length 500 mm each were used in the reflector block to prevent the possibility of contact with pieces of beryllium when the blocks crack, and they were irradiated to fluences of $5.0 \cdot 10^{21}$, $6.0 \cdot 10^{21}$, $1.6 \cdot 10^{22}$, and $5.3 \cdot 10^{22}$ neutrons/cm^2, correspondingly. During the tests the central channel and the strips were flushed by a heat carrier (water) under a pressure of 5 MPa and having a temperature of about 373°K.

During the studies the items were examined externally and the geometrical dimensions were measured with an error of ±0.5 mm. The microscopic densities were determined to ±0.04% by weighing with immersion. The lattice volume was calculated from the a and c parameters as determined by x-ray methods from the (220) and (006) maxima, correspondingly. Direct [001] polar figures were recorded with a DRON-2.0 diffractometer in reflection to determine the textures of the channel tube and strips.

The specimens were analyzed chemically for molybdenum, which is formed by nuclear reaction [3]; this was performed photometrically with potassium thiocyanate [4]. The relative error was ±10% of the absolute molybdenum content in the alloy.

The initially rectilinear strips became buckled as a result of the irradiation, and the length increased by 10-20 mm (Fig. 2). The relative extension of the strips increased with the fluence (Fig. 3) and attained about 3.9% for the strip irradiated to a fluence of $5.3 \cdot 10^{22}$ neutrons/cm^2. During the tests, the outside diameter of the part of the channel in the core fell substantially (Fig. 4). As the fluence increased, there was a linear reduction in the diameter from the initial value to the minimal one. There was also considerable hardening in the channel-tube material. The microhardness of the irradiated material was 260 MPa, as against 1700 MPa in parts of the channel that had not been irradiated.

The macroscopic density of the Zr + 2.5% Nb alloy and the volume of the unit cell gradually increased as the fluence rose, the increases being, respectively, 0.43 and 0.35% at the maximal fluence. Annealing for 1 h at 770°K led to complete recovery in the unit-cell volume (Fig. 5a). The radiation defects accumulated during irradiation are almost completely healed at this temperature [5], so one assumes that these defects produce the observed change in unit-cell volume.

However, this annealing did not produce an appreciable change in the macroscopic density (Fig. 5b). To explain this, we calculated the mean number n of atoms per unit cell for the alloy irradiated to the maximal fluence and annealed for 1 h at 770°K:

$$n = \rho V N_A / A_{av},$$ (1)

where ρ is the macroscopic density; V, unit-cell volume, N_A, Avogadro's number; and A_{av}, average atomic mass of the Zr + 2.5% Nb alloy. Here n = 2.02, which exceeds the average number of atoms in the unit cell of the unirradiated alloy by about 1%. Evidently, the surplus atoms may

647
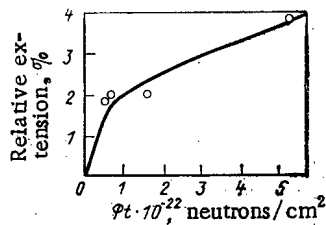
Fig. 3

Fig. 4

Fig. 3. Dependence of the relative extension of strips made of Zr + 1% Nb alloy (20% cold deforma-tion) on the fluence.
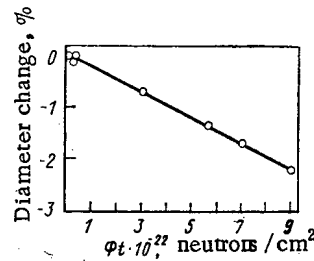
Fig. 4. Change in outside diameter of Zr + 2.5% Nb channel tube in accordance with fluence.

either be present at interstitial positions or form the nuclei of some compound denser than the matrix. Neutron irradiation produces appreciable alloying of the Zr + 2.5% Nb alloy with molybdenum formed by nuclear reaction (Fig. 5c). The molybdenum concentration increased up to about 0.7 mass % as the fluence increased. Since the maximal solubility of molybdenum in zirconium does not exceed 0.2% [6], some of the molybdenum will form the intermetallide $ZrMo_2$. The atomic volume of the intermetallide at 18.1 $\mathring{A}^3$ is approximately 20% less than that for zirconium (1 $\mathring{A}$ = 10^{-10} m). Therefore, the presence of the denser phase can explain the ob-served increase in channel material density.

However, the changes in unit-cell volume and macroscopic density cannot explain the channel-tube shape changes. For example, the reduction in tube diameter due to increase in the macroscopic density should not exceed 0.2%. Therefore, one assumes that the diameter re-duction is produced mainly by radiation growth. In a polycrystalline structure in which the grains are close to equiaxial, the deformation during radiation growth is defined [7] by

$$\varepsilon_d = SF_d (\Phi t)^n, \tag{2}$$

where ε_d is the growth deformation in direction d; S, structural growth coefficient; Φt, neu-tron fluence; n, exponent; and F_d, texture growth coefficient, which is determined from the texture parameter f_d via

$$F_d = 1 - 3f_d. \tag{3}$$

Figure 6 shows [001] polar figures for specimens cut from the strip and channel tube. The spreads in the texture of the strip and tube in the direction of the A axis are ±30 and 20°, correspondingly. The texture was evaluated from the texture parameter f_d in the direction d [7]. Table 1 gives the values of f_d and F_d.

The magnitude and sign of the radiation-growth deformation of the channel and strip in this direction are determined by the value of the texture coefficient, since the value of the structure coefficient is independent of the texture. On account of technical difficulties and the small values of the radiation growth, we did not make direct measurements in the axial and tangential directions (for the channel) and the transverse directions (for the strip). We therefore calculated these changes. If we know ε_i and F_i for one direction, one can deter-mine ε_x for those directions for which F_x is known from

$$\varepsilon_x/\varepsilon_i = F_x/F_i. \tag{4}$$

We calculated the size changes in the channel tube and strip after irradiation to fluences of about $9.1 \cdot 10^{22}$ and $5.3 \cdot 10^{22}$ neutrons/cm^2, correspondingly, for the principal directions.

In calculating the size changes for the channel tube, we incorporated the fact that when the diameter changes by Δd, the wall thickness changes by Δh and there is negative growth Δd_t in the tangential direction (Table 2):

$$\Delta d = \Delta h + \Delta d_t. \tag{5}$$

Then the relative diameter change is

$$\frac{\Delta d}{d} = \frac{\Delta h}{d} + \frac{\Delta d_t}{d} = \frac{h}{d} \varepsilon_R + \varepsilon_t. \tag{6}$$

648
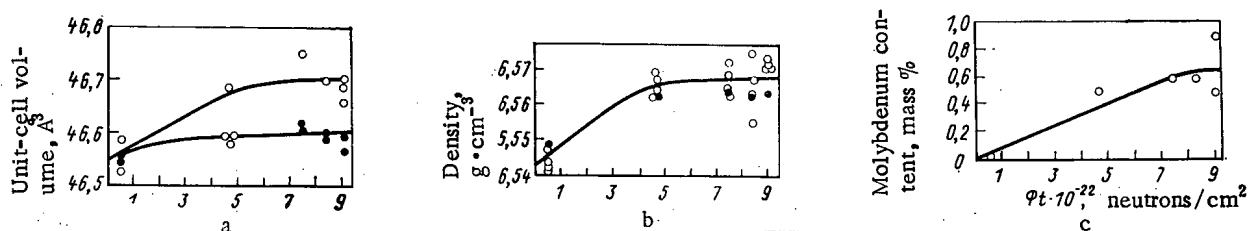
Fig. 5. Changes in unit-cell volume (a), macroscopic density (b), and molybdenum content (c) in Zr + 2.5% Nb alloy in relation to fluence after irradiation and subsequent annealing at 770°K for 1 h (black points) and after irradiation alone (white points).
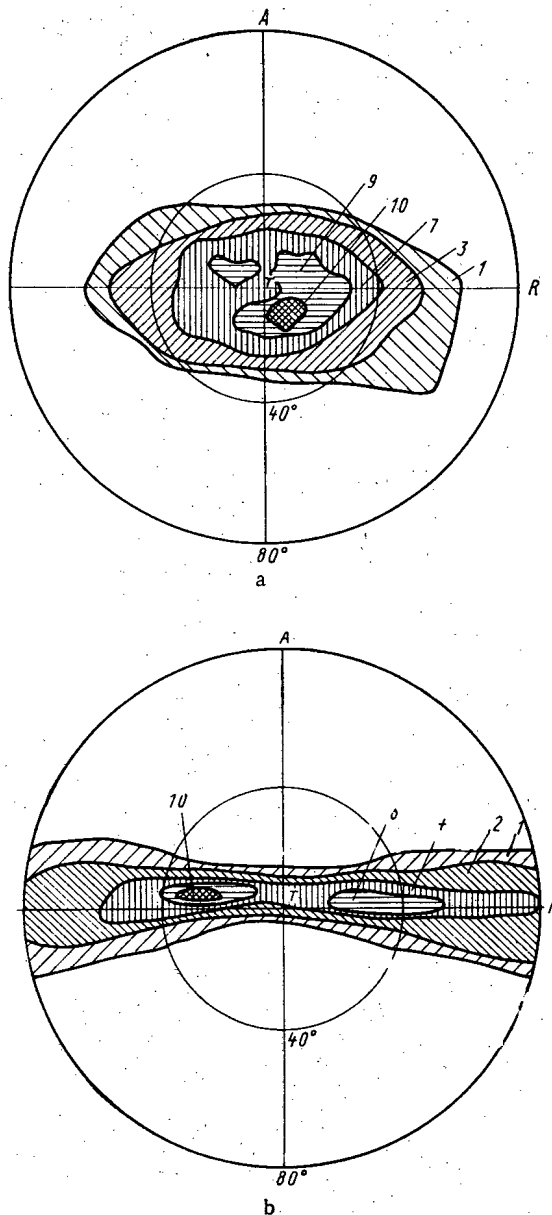
Fig. 6. [001] direct polar figures for strip (a) and channel tube (b). Direction of principal axes: A) longitudinal and axial; R) perpendicular to narrow side of strip and radial; T) perpendicular to wide side of strip and tangential. Different forms of hatching are the densities of the basal poles in relative terms.

From (2) with (4), (6) we get that ε_R and ε_t are $1.4 \cdot 10^{-2}$ and $2.2 \cdot 10^{-2}$, correspondingly. Therefore, the diameter change, in the main, is due to growth in the tangential direction. The relative length change in the central channel found from (4) is $3.6 \cdot 10^{-2}$. Table 2 gives the calculated and measured changes in strip and channel-tube sizes as a result of the growth.

These results enable one to determine the structural growth coefficients S_1 and S_2 for the Zr + 1% Nb alloy in the state after cold deformation and for the Zr + 2.5% Nb alloy. If

649

TABLE 1. Texture Parameters f_d and Texture Growth Coefficient F_d for Principal Directions in Strip and Channel Tube

Item	f_A	f_R	f_t	F_A	F_R	F_t
Channel tube	0,015	0,459	0,526	0,956	—0,377	—0,579
Strip	0,023	0,067	0,910	0,931	0,799	—1,730

TABLE 2. Change in Dimensions of Strip and Channel Tube as a Result of Radiation Growth

Item	Geometrical dimensions	Initial, mm	After irradiation, mm	Absolute changes mm	Relative changes, %
Channel tube	Length in core	350	362,6*	12,6*	3,6*
	Outside diameter	98,2	96	—2,2	—2,24
	Wall thickness	6	5,92*	—0,08*	—1,4*
Strip	Length	500	520	20	3,8
	Width	15	14,5*	0,5*	3,3*
	Thickness	0,5	0,46*	0,04*	—7,1*

*Calculated values.

the growth deformation occurs in accordance with Eq. (2) with n = 1, the structural coefficients are:

$$S_1 = \frac{\varepsilon_A}{F_A (\Phi t)} = 0.73 \cdot 10^{-24} \text{ cm}^2/\text{neutron};$$ (7)

$$S_2 = \frac{\varepsilon_t}{F_t (\Phi t)} = 0.42 \cdot 10^{-24} \text{ cm}^2/\text{neutron};$$ (8)

If one uses these coefficients and determines the texture for items made of zirconium alloys, one can **forecast the radiation** growth in any direction. For example, the dependence of the relative diameter deformation for a textured tube of Zr + 2.5% Nb alloy on the neutron fluence takes the form

$$\varepsilon = S_2 F_t (\Phi t) = 2.4 \cdot 10^{-25} (\Phi t).$$ (9)

This relationship agrees with published data [8].

LITERATURE CITED

1. R. Murgatroyd and A. Rogerson, J. Nucl. Mater., 90, 240 (1980).
2. V. Fidleris, A Review, Chalk River Nuclear Laboratories, AECL-7053 (1980).
3. B. S. Dzhelepov and L. K. Peker, Decay Schemes of Radioactive Nuclides [in Russian], Vol. 1, Nauka, Moscow—Leningrad (1966), p. 2.
4. A. I. Busev, in: Methods of Determining and Analyzing the Rarer Elements [in Russian], Izd. Akad. Nauk SSSR, Moscow (1961), p. 537.
5. V. S. Belokopytov, A. S. Pokrovskii, and G. P. Kobylyanskii, Aspects of Nuclear Science and Engineering, Radiation Materials Science Series, Irradiation Methods and Techniques [in Russian], Issue 6 (1975), p. 13.
6. O. S. Ivanov et al., Structures of Zirconium Alloys [in Russian], Nauka, Moscow (1973).
7. M. Holicky and J. Schreder, J. Nucl. Mater., 44, No. 1, 31 (1972).
8. A. Rogerson and R. Murgatroyd, ibid., 80, No. 2, 260 (1979).

HIGH-TEMPERATURE RADIATION-INDUCED EMBRITTLEMENT OF NICKEL

V. L. Arbuzov, S. N. Votinov, A. A. Grigor'yan,   UDC 621.039:539.373
B. V. Bychkov, S. E. Danilov, S. M. Klotsman,
I. V. Al'tovskii, N. K. Vinogradova,
E. A. Voitekhova, and V. N. Geminov

The reliability and operational lifetime of a number of units in fast-breeder and thermo-nuclear reactors must largely depend on the degree of the high-temperature radiation-induced embrittlement (HTRE) of materials under neutron irradiation. Many investigators [1-5] associate HTRE with the formation of helium in austenitic chrome-nickel and chrome-mangenese steels, in high-nickel alloys, in nickel, and in other metals and alloys due to the (n, α) reactions. The sharp drop in plasticity and the intergrain nature of the rupture of specimens in tensile tests in the temperature range $(0.5-0.6)T_{melt}$ were observed also after irradiation of specimens of the materials listed above by α particles with energies up to 40 MeV and with 225-MeV electrons, i.e., with the introduction of helium atoms.

It was noted at the same time [6-8] that HTRE is manifested most clearly in materials which even without irradiation tend to rupture along grain boundaries in tension tests at high temperature. It is well known that the tendency of a number of materials (copper, nickel, high-nickel alloys, austenitic stainless steels) to rupture in this manner is, to a large extent, due to the presence of impurities and their segregation [9, 10], and in our opinion it is only intensified by irradiation.

In accordance with these ideas, irradiation of materials susceptible to HTRE, by particles capable of creating radiation-induced defects, but which do not give rise to the formation of helium, must lead to the appearance of the same HTRE as with reactor irradiation. Such particles are, e.g., electrons with energies less than 8 MeV (for nickel), i.e., below the threshold energy for the formation of helium nuclei as a result of (γ, α) reactions [5].

In this work we investigated the effect of irradiation with 5.5-MeV electrons on the high-temperature mechanical properties of commercial-grade nickel without helium and with helium, introduced beforehand by the tritium trick method [11].

Materials and Experimental Procedure. Taking into account the special role of impurities in HTRE of metals and alloys, we selected, specially for the investigations, commercial-grade nickel with a purity of 99.7 mass %, containing the following (mass %): 0.15 Fe, 0.05 Al, 0.01 C, 0.015 Cu, 0.001 S, 0.001 P, and 0.005 each of Pb, Bi, Sn, Zn, and Co.

We annealed the specimens used for irradiation and mechanical testing (the dimensions of the working part were $10 \times 3.5 \times 0.22$ mm) at 800°C for 1 h in quartz ampuls, filled with argon; after annealing, the grain size in the specimens was 30-40 µm. We irradiated the specimens with 5.5-MeV electrons at temperatures of 350° and 500°C on a LUÉ-5 accelerator. The electron current density was $\sim 6 \cdot 10^{13}$ cm$^{-2} \cdot$sec^{-1}; the rate of radiation damage was $\sim 10^{-8}$ displacements/atom·sec. The fluence of electrons was $2 \cdot 10^{18}$ and 10^{19} cm^{-2}.

We saturated the nickel specimens at 700°C and under a pressure of 33 kPa over 15 h in a special apparatus filled with a mixture of hydrogen isotopes with 35 vol.% ^{3}H. The initial concentration of tritium, determined by the method of isotopic equilibration, constituted ~ 0.7 Ci/100 g Ni, or $1.5 \cdot 10^{-3}$ at.% (1 Ci = $3700 \cdot 10^{10}$ Bq). We held the tritium-saturated specimens at room temperature in glass weighing bottles with ground plugs for 1.5 yrs ($\sim 13,000$ h).

We indicate below the tritium and helium content of the nickel specimens [12]:

Initial tritium concentration C^3_H, at.% $1.5 \cdot 10^{-3}$
Computed helium concentration prior to mechanical testing C^3_{He}, at.% $1.2 \cdot 10^{-4}$

651
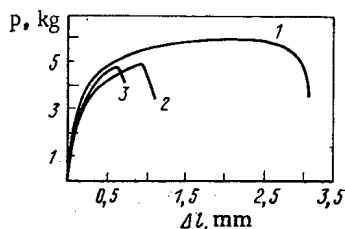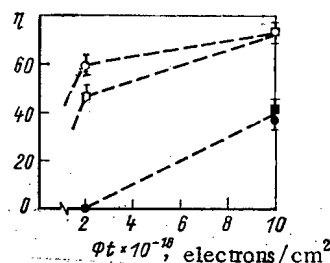
Fig. 1   Fig. 2

Fig. 1. Primary stress—strain curves for nickel at 700°C: 1) unirradiated specimen; 2, 3) irradiated at 500°C and electron fluence $2 \cdot 10^{18}$ and 10^{19} cm^{-2}, respectively.

Fig. 2. Dependence of the degree of embrittlement η of nickel on temperature and irradiation dose (T_{test} = 700°C) for nickel without helium (O, ●) and with 10^{-4} at.% helium (□, ■) at T_{irr} = 500 (O, □) at 350°C (●, ■).

Experimentally determined gas concentration $C^{*}_{^3H + ^3He}$, at.%:

    prior to mechanical testing $7 \cdot 10^{-4}$

    after mechanical testing at 700°C $2 \cdot 10^{-4}$

The quite good agreement between the computed and experimental estimates of the helium concentration in nickel specimens before and after heating up to 700°C with mechanical tests permits assuming that the helium concentration in the specimens was close to the computed value.

We performed the mechanical tests of the specimens on the "Instron" machine at a temperature of 600–800°C in air (and, selectively, in argon) with a strain rate of $1.5 \cdot 10^{-3}$ sec^{-1}. The specimens were heated up to the temperature of the tests within 10–15 min and they were held at that level prior to stretching for 15 min. Each experimental point characterizes the average for three tested specimens. Tests in argon and in air gave the same results. We calculated the degree of embrittlement of nickel η using the relation

$$\eta = \frac{\delta_{init} - \delta_{irr}}{\delta_{init}} \cdot 100\%.$$

We investigated the nature of the rupture of the specimens accompanying high-temperature stretching by methods of optical and scanning electron-microscopy.

Experimental Results. Figure 1 shows the primary stress—strain curves for the starting and irradiated nickel specimens not containing helium. Irradiation causes almost complete disappearance of the strain localization stage (formation of a nick) and considerably shortens the strain hardening stage, indicating embrittlement of the material. Irradiation with electrons had an analogous effect even for stretching of nickel with helium.

The results of mechanical tests (Tables 1 and 2, Fig. 2) show that irradiation of nickel with 5.5-MeV electrons leads to high-temperature embrittlement, the degree of which depends on the temperature of irradiation and the fluence of electrons, but does not depend on the presence of helium atoms in the nickel in the amount $\sim 10^{-4}$ at.%. Thus, irradiation of nickel at 350°C up to a fluence of $2 \cdot 10^{18}$ cm^{-2} led to appreciable ($\sim 40\%$) embrittlement at 700°C for nickel with and without helium. The embrittlement of nickel as a result of irradiation at 500°C reached 50–60% already with a fluence of $2 \cdot 10^{18}$ cm^{-2}, while at a fluence of 10^{19} cm^{-2} it increased approximately up to 75%.

A metallographic investigation established (Fig. 3) that irradiation with 5.5-MeV electrons changes the nature of the rupture of the specimens: the intragrain rupture of unirradiated specimens is replaced by intergrain rupture, independent of the presence of helium.

---

*Due to the absence of standards with ^{3}He, the total current of ions with mass numbers 3 was recorded, so that the total content of tritium and helium was determined in the experiments.

TABLE 1. Mechanical Properties of Nickel without Helium

Electron fluence, cm^{-2}	Testing temperature, °C	Ultimate strength σ_u, MPa	Yield stress $\sigma_{0.2}$, MPa	Elongation δ, %
		Without irradiation		
—	600	93	54	28,0
—	700	78	50	27,0
—	800	65	51	29,0
		Irradiation at 350°C		
$2 \cdot 10^{18}$	600	92	52	28,0
$2 \cdot 10^{18}$	700	79	51	30,0
10^{19}	700	74	42	17,0
		Irradiation at 500°C		
$2 \cdot 10^{18}$	600	90	45	13,0
$2 \cdot 10^{18}$	700	70	40	11,0
10^{19}	700	65	33	7,0

TABLE 2. Mechanical Properties of Nickel with Helium ($\sim 10^{-4}$ at.%)

Electron fluence, cm^{-2}	Testing temperature, °C	Ultimate strength σ_u, MPa	Yield stress $\sigma_{0.2}$, MPa	Elongation δ, %
		Without irradiation		
—	600	85	45	36,0
—	700	70	42	38,0
—	800	60	40	36,0
		Irradiation at 350°C		
10^{19}	700	78	48	22,0
		Irradiation at 500°C		
$2 \cdot 10^{18}$	700	72	52	20,0
10^{19}	700	68	44	10,0

Discussion of Results. The investigations show that irradiation of commercial-grade nickel with 5.5- MeV electrons leads to a considerable decrease in plasticity and a transition from intragrain rupture of unirradiated specimens to intergrain rupture of irradiated specimens under tension tests in the temperature range $(0.5–0.6)T_{melt}$. These effects are analogous to the characteristic indications of HTRE of nickel and austenitic stainless steels and alloys with reactor irradiation, which, as established in [1–4], appears in the materials indicated as a result of reactor irradiation up to a neutron fluence of $\sim 10^{18}-10^{19}$ cm^{-2}, while according to the data in [13], significant embrittlement at 800°C of an alloy such as nimonik (decrease in elongation from 30 to 5%) was observed with a neutron fluence of only 10^{16} cm^{-2}. With such a low neutron fluence, a negligible amount of helium ($\sim 10^{-7}-10^{10}$ at. %) accumulates in the class of materials being studied [14–16]. In an experiment on irradiation of nickel and austenitic steels with α particles [1, 2] it was established that helium begins to have an appreciable effect on the high-temperature plasticity of materials at concentrations of $\sim 10^{-5}$ at.% and above. At this level, radiation damage constitutes $\sim 10^{-4}$ displacements/atom [5], i.e., it is comparable to the damage that arises with neutron irradiation accompanied by appreciable decrease in the high-temperature plasticity of nickel and austenitic steels and alloys. The introduction of $\sim 10^{-4}$ at.% helium into nickel using the "defect-free" tritium trick method had no effect on the high-temperature plasticity.

The concentration of metallurgical impurities in structural materials greatly exceeds the concentration of helium forming with irradiation. Irradiation stimulates redistribution of impurity elements and the formation of their grain-boundary segregations [17, 18]. The embrittling action of sulfur in nickel was reported in [17]; the influence of phosphorus,
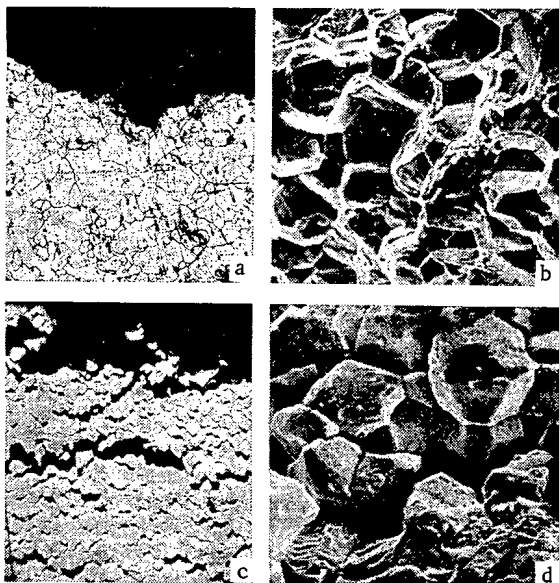
Fig. 3. Nature of the rupture of nickel specimens at 70°C: a, b) unirradiated specimens (×200 and 100); c, d) irradiation at 500°C and electron fluence $2 \cdot 10^{18}$ cm^{-2} (×200 and 1000); b, d) scanning electron microscopy of the rupture surface.

653

TABLE 3. Effect of HTRE in Nickel Accompanying Irradiation by Different Particles

Bombarding particle	Particle fluence, cm^{-2}	Degree of damage, displ./atom	Helium content, at.%	C_{He}, at.%/D, displ./atom	Presence of HTRE	Reference
Fission neutrons	10^{18}	$5 \cdot 10^{-1}$	$5 \cdot 10^{-8}$	10^{-4}	Same	[3, 4, 14-16]
225-MeV electrons	$2 \cdot 10^{18}$	$7 \cdot 10^{-1}$	$4 \cdot 10^{-7}$	$6 \cdot 10^{-4}$	Same	[5]
α particles up to 40 MeV	10^{15}	$6 \cdot 10^{-5}$	$6 \cdot 10^{-5}$	1	»	[1, 2, 5]
5.5-MeV electrons	$2 \cdot 10^{18}$ 10^{19}	$3,5 \cdot 10^{-1}$ $2 \cdot 10^{-3}$	0 0	0 0	» »	This paper
Tritium trick	0	0	10^{-4}	—	No	This paper

antimony, and tin on the hardening of grain boundaries in austenitic chrome-nickel steel was reported in [20]. The influence of the impurity concentration on HTRE of nickel and chrome-nickel steels accompanying irradiation with α particles and high-energy electrons was noted in [1, 2, 5].

These data, together with the experiments performed, confirm, in our opinion, the previously stated [6-8] hypothesis that the determining factor in HTRE of metals and alloys accompanying irradiation is the formation of point radiation defects, stimulating redistribution of impurities and the formation of their grain-boundary segregations.

It should be noted that this interpretation of the reasons for HTRE in metals and alloys does not agree with the absence of a drop in the high-temperature plasticity in experiments involving irradiation of nickel with 8-MeV electrons and protons and lithium ions, which produce radiation defects in materials without the formation of helium [5]. This result could be due, in our opinion, to the very high purity of the nickel studied (99.90 mass %). In addition, as our results have shown, the degree of high-temperature embrittlement of nickel greatly depends on the temperature and dosage of irradiation. In [5], these parameters were apparently not "optimal" for appreciable development of HTRE.

Analysis of experimental data on HTRE of metals and alloys (Table 3) shows that this phenomenon is always observed when point radiation defects are generated; the concentration of helium atoms, in this case, and its relation to the degree of radiation damage can vary over a wide range and even equal zero.

CONCLUSIONS

Thus, the results of this work and their comparison with published data permit formulating the following conclusions.

1. The occurrence of high-temperature embrittlement in commercial-grade nickel with a purity of 99.70 mass % accompanying irradiation with 5.5-MeV electrons, which generate point radiation defects in the material without the formation of helium atoms (the transmutant), has been established experimentally for the first time.

2. "Defect-free" injection of $\sim 10^{-4}$ mass % helium into nickel by the tritium trick method does not decrease the high-temperature plasticity of the material.

3. Nickel with helium, introduced by the tritium trick method, becomes brittle under irradiation with 5.5 MeV electrons to the same degree as nickel not containing helium.

4. High-temperature embrittlement is observed in nickel when the nickel is irradiated with neutrons, α-particles up to energies of 40 MeV, and 225- and 5.5-MeV electrons, resulting in the formation of radiation defects. This suggests that radiation-initiated redistribution of metallurgical impurities and the formation of their grain-boundary segregations play a determining role in HTRE of nickel and other structural materials.

5. The solution of the problem of specific mechanisms governing the influence of impurities on HTRE in metals and alloys requires further investigation. Meanwhile, it is already possible to formulate the general principle for increasing the resistance of materials to HTRE: suppression of redistribution of impurities and formation of grain-boundary segrega-

tions. This can be achieved, e.g., by increasing the purity of the materials with respect to the impurities or binding the impurities into thermodynamically stable complexes and compounds, i.e., by doping, heat treatment, as well as pulverization of the grains and cold **deformation.**

LITERATURE CITED

1. N. P. Agapova et al., At. Energ., 41, No. 5, 314 (1976).
2. N. P. Agapova et al., in: Reactor Materials Engineering. **Proceedings of a Conference on** Reactor Materiology, Vol. 2, **TsNIIatominform,** Moscow (1978), p. 215.
3. K. Garr et al., Met. Trans., 2, 269 (1971).
4. E. Bloom and F. Wiffen, J. Nucl. Mater., 58, 171 (1975).
5. V. F. Zelenskii et al., Problems in Atomic Science and Technology. Series on Physics of Radiation Damage and Radiation Materiology [in Russian], No. 1(2), p. 8 (1975).
6. S. N. Votinov et al., At. Energ., 27, No. 6, 506 (1969).
7. S. N. Votinov et al., Radiation Physics of Solids and Reactor Materiology [in Russian], Atomizdat, Moscow (1979), p. 103.
8. V. I. Prokhorov and S. N. Votinov, Problems in Atomic Science and Technology. Series on Fuel and Structural Materials, No. 2, 3 (1975).
9. E. Gudremon, Special Steels [in Russian], Vol. I, Metallurgiya, Moscow (1956), p. 595.
10. H. Franz, H. Pfeifer, and I. Pfeifer, Metallik, 58, 87 (1967).
11. J. Gost and R. Hichmann, J. Vac. Sci. Technol., 12, 516 (1974).
12. S. N. Votinov et al., Preprint I. V. Kurchatov Inst. At. Energy, No. 3760, Moscow (1983).
13. Nuclei and the Radiation Resistance of Structural Materials [in Russian], Naukova Dumka, Kiev (1978), p. 243.
14. G. Kulcinski, in: Proc. Int. Conf. on Radiation Damage: The **Second** Most Serious Obstacle to Commercialization of Fusion Power Radiation Effect and Tritium Technology to Fusion Reactors, Tennessee, Oct. 1-3, 1975, Vol. 1, p. 17.
15. A. G. Zaluzhnyi et al., Ref. 2, p. 148.
16. B. A. Shilyaev, V. A. Kuz'menko, and V. A. Yamnitskii, Problems in Atomic Science and Technology. Series in Physics of Radiation Damage and Radiation Materiology, No. 2(10), 43 (1979).
17. R. Johnson and N. Lam, Phys. Rev. B, 13, 4364 (1976).
18. V. L. Arbuzov et al., Dokl. Akad. Nauk SSSR, 244, No. 5, 1114 (1979).
19. R. Holt and W. Wallace, Int. **Metall.** Rev., 21, No. 1, 143 (1976).
20. I. Kameda and I. McMahon, Met. Trans., 12A, No. 1, 273 (1981).

STATISTICAL ANALYSIS OF EXPERIMENTAL DATA ON THE CROSS SECTIONS OF
^{233,235,238}U, ^{237}Np, ^{239,242}Pu FISSION BY NEUTRONS OF ENERGY 2.6,
8.5, AND 14.5 MeV

V. N. Dushin, A. V. Fomichev, S. S. Kovalenko,   UDC 539.173.4
K. A. Petrzhak, V. I. Shpakov, R. Arl't, M. Iosh,
G. Muziol', Kh.-G. Ortlepp, and V. Vagner

Absolute measurements of the fission cross sections of heavy nuclei by neutrons of fixed energy — 2.6, 8.5, and 14.7 MeV — have been performed in a collaboration between the V. G. Khlopin Radium Institute (USSR) and the Technical University (German Democratic Republic) for a number of years. The work was performed on neutron generators of the Radium Institute and the Technical University, and also on the tandem generator of the Central Institute of Nuclear Research (German Democratic Republic).

The measuring apparatus and experimental methods were repeatedly improved and modified. To increase the accuracy, the measurements for all the nuclides were repeated on different apparatus and, for the most important nuclides, many times. Thus, a large set of experimental data, published at various times [1-4], is now available.

The aim of the present work is the critical analysis of the results, measurement errors, and correlative estimates necessary to obtain final values of the cross sections from the experimental data.

The measurements were made by the method of time-correlated accompanying particles. The method itself was described in detail earlier; see, e.g., [2]. Therefore, brief recollection of its principles is all that is necessary here. The reaction ^{3}H(d, n)^{4}He or ^{2}H(d, n)^{3}He served as the neutron source. The ^{3}He or ^{4}He particles accompanying the neutrons are recorded by a detector in some solid angle determined by the input diaphragm of the detector. The neutron cone corresponding to these particles irradiates a target of fissile material. The accompanying particles and fission-accompanying-particle coincidences are recorded. Under the condition that the base of the neutron cone is completely covered within the limits of the target, the fission cross section is determined by the expression

$$\sigma_f = \frac{N_c}{n N_{a.p}}, \tag{1}$$

where N_c is the number of coincidences; $N_{a.p}$, number of accompanying particles; and n, number of nuclei of the given isotope per cm^2 of target.

The following corrections are introduced into the experimental data: for the background of random coincidences; for the background in the accompanying-particle channel; for the losses and variation in neutron-flux energy on account of scattering on the constructional materials, target substrates, windows, etc.; for the efficiency of recording fission fragments (by ionization chambers in pulsed current conditions), which is determined by two corrections — for absorption in the active layer of the target and for extrapolation of the amplitude spectrum of the fragments to zero discrimination; for the fission of impurity isotopes in the target.

The corrections for the background of random coincidences are determined by simultaneous separate recording of the complete number of coincidences and random coincidences in the same circuit, and also from an analysis of the accompanying-particle-fission time spectrum. The background in the accompanying-particle channel is measured without a target or neutron source, and also found from the analysis of the amplitude spectrum in the channel.

The corrections for distortion of the neutron flux are calculated by a method consisting in the solution of the inverse problem of radiation transfer [5]. The transfer equations are

---

solved by the Monte Carlo method with modeling of the real experimental geometry, while taking account of all the constructional materials.

Absorption of fragments in the layer is considered as a function of the layer thickness, neutron energy, fragment path length, and anisotropy of fission [6].

The target of fissile material was prepared at the Radium Institute by the method of high-frequency sputtering on a nonaxially rotating substrate, ensuring high uniformity of the layer. The target was calibrated by measuring the α activity in an apparatus with a small solid angle. The homogeneity of the layer was determined by scanning over the surface using an α detector with a diaphragm of diameter 1-2 mm; for a target with small activity (^{238}U, ^{235}U), an x-ray analyzer was used.

In determining the number of nuclei, the following corrections were made in the results of α-activity measurement subtraction of the impurity-isotope peaks (impurities of low-activity isotopes were determined by mass-spectrometric analysis); corrections for the α-detector background; for the extrapolation of the α spectrum to the zero level of discrimination; for the efficiency and geometry of the measuring apparatus.

All these corrections are sources of error. In addition, contributions to the error of the results are made by: the statistics of the number of coincidences; the statistics of α counting in target calibration; the statistics of the accompanying particles; the half-lives in calculating the number of nuclei from the α activity; the inhomogeneity of active-layer thickness in the target; inaccuracy in the position of the neutron cone relative to the target of fissile material; error in the energy of the bombarding neutrons.

Analysis of the experimental data and calculation of the mean values is performed on the basis of taking account of the correlations between the errors of the individual measurements. This changes and increases the reliability of the mean values, and also allows the inaccuracies to be correctly converted and the error of the results to be determined, allows missing measurements to be reliably determined, and allows the results of different — including integral — measurements to be mutually refined.

To take account of the correlations, covariant matrices of the results $cov(\sigma_f^i, \sigma_f^j)$ are constructed; they are calculated from the covariations of the partial errors of the cross sections:

$$cov\,(\sigma_j^i,\ \sigma_j^j) = S_i^T cov\,(x_l^i,\ x_k^j)\,S_j, \tag{2}$$

where σ_f^i, σ_f^j are the results of measuring the fission cross sections; $cov(x_l^i, x_k^j)$, covariational matrix of the partial measurement errors; S_i, S_j, sensitivity-coefficient vectors; x_l^i, x_k^j, quantities appearing in the formula for calculating the fission cross sections and corrections; i, j denote the number of the measurement; and k, l denote the number of the partial error of the measurement.

In calculating the covariation, the following values are assumed in Eq. (1) for the fission cross section:

$$N_c = (x_1 - x_2)\,(1 + x_3)\,(1 - x_4)\,(1 + x_5);\ N_{a.p} = (x_6 - x_7)\,(1 - x_8);$$
$$n = (x_9 - x_{10})\,(1 - x_{11})\,(1 + x_{12})\,x_{13}^{-1}x_{14}\,(\ln 2)^{-1}, \tag{3}$$

where x_1 is the statistics of coincidence counting; x_2, statistics of random-coincidence counting; x_3, absorption of fragments in the target layer; x_4, contribution from fission of impurity isotopes; x_5, correction for extrapolation of the spectrum of fragments to zero discrimination; x_6, statistics of the accompanying particles; x_7, background in the accompanying-particle channel; x_8, neutron-beam distortion; x_9, α-particle statistics in measuring the number of nuclei in the target; x_{10}, statistics of the background in the α-particle detector; x_{11}, contribution from impurity isotopes in measuring the number of nuclei in the target; x_{12}, correction for extrapolation of the α spectrum to zero discrimination; x_{13}, geometric factor in measuring the α activity of the target; x_{14}, half-life.

In addition, the following errors are also considered: x_{15}, due to inhomogeneity of the target layer; x_{16}, due to inaccuracy in the position of the neutron cone at the target; and x_{17}, due to inaccuracy in specifying the neutron energy. In the statistical analysis, all the x are variable.

The last three quantities (x_{15}, x_{16}, x_{17}) do not appear in the formula for determining the cross sections; therefore, no corrections for these quantities are introduced, and they are regarded as partial errors. The total deviation from homogeneity of the layer thickness

657

TABLE 1. Covariational Error Matrices for Measurements of Cross Sections for ^{235}U Fission by Neutrons of Energy 14-15 MeV

Measurements at*	σ_f, b	E_n, MeV	Covariational matrix, (%)²										
RI	2,0714	14,7	2,08	0,92	0,73	0,82	0,82	0,82	0,41	0,41	0,41	0,41	0,41
RI	2,1348	14,7		2,08	0,73	0,82	0,82	0,82	0,41	0,41	0,41	0,41	0,41
RI	2,0755	14,7			3,03	0,67	0,67	0,67	0,45	0,39	0,39	0,39	0,39
RI	2,0960	14,7				1,90	0,74	0,74	0,31	0,31	0,31	0,31	0,31
RI	2,1010	14,5					3,02	0,74	0,31	0,31	0,31	0,31	0,31
RI	2,0840	14,0						3,02	0,31	0,31	0,31	0,31	0,31
TU	2,083	14,7							1,76	1,05	1,06	1,05	1,06
TU	2,087	14,7								1,45	1,06	1,05	1,06
TU	2,075	14,7									2,76	1,05	1,07
TU	2,073	14,7										1,51	1,06
TU	2,075	14,7											1,81

*RI indicates Radium Institute; TU indicates Technical University.

in the target is taken as x_{15}, although this estimate of the error is too high, generally speaking.

To ensure localization of the neutron cone entirely within the limits of the target, its profile was carefully measured. The maximum estimate of the possible "tails" of the cone passing beyond the limits of the measurement statistics is taken as the partial error x_{16}. The partial error x_{17} is determined from the calculational and experimental dispersions of the neutron energy and from the slope of the energy dependence of the cross section.

The basic problem in constructing the covariational matrices is to determine the measurements. Since the measurement errors are divided into sufficiently elementary components, corresponding to the intellectual structure of the experiment, it seems correct, on the basis of expert evaluations, to assign one of three levels of correlation to the partial errors: zero ($k = 0$), complete ($k = 1$), and mean ($k \simeq 0.5$-0.7).

The sensitivity coefficients $s_i^k = \partial\sigma_f^i/\partial x_k^i$ are calculated on the basis of Eqs. (1)-(3) above, relating σ_f^i and x_k^i. This relation may be regarded as an expression of the solution of the inverse problem of radiation-transport theory in terms of corrections [5]. In the present case, Eqs. (1)-(3) are of the necessary accuracy, which means that without considering the system of equations of the inverse problem, attention may be confined to the solution in terms of corrections.

The measurement results published in [1-3] are also considered. The data for ^{239}Pu and ^{237}Np [1] are eliminated here, as they are known to be inconsistent. They were obtained at an earlier stage of the work, using targets with very thick (up to 3 mm) substrates and a high percentage of impurity nuclides. In [3], a preliminary value was given for the cross section of ^{235}U fission by neutrons of energy 8.5 MeV; this value is reexamined here, together with the cross section for ^{238}U fission given in [1]. The results of new (1981-1982) measurements of the cross section of ^{235}U fission by neutrons of energy 2.6 MeV and of ^{233}U, ^{237}Np, ^{239}Pu, and ^{242}Pu fission by neutrons of energy 14.7 MeV are also analyzed [4]. All these data with covariational error matrices are given in Tables 1 and 2. RI and TU denote where the measurements were performed: the Radium Institute or the Technical University.

The data are analyzed from the viewpoint of the concepts of the χ^2 method. The error of the ratio σ_f^i/σ_f^j is considered to determine the inconsistent measurements (for ^{239}Pu and ^{235}U). Taking convariation into account reduces the error of the ratio by a factor of 3.5, which allows two measurements to be eliminated [4] since their deviation from unity exceeds the error by a factor of ~ 4.

The final values of the cross sections are estimated from the generalized least-squares method, which has been described repeatedly in the literature; see, e.g., [7]. The data obtained, together with the errors, are shown in Tables 3 and 4. Analysis indicates the statistical inconsistency of the measurement results for ^{239}Pu. The large value of χ_3^2 (~ 6) implies an error that has not been taken into account.

Table 3 gives the results of separate analysis of the measurements of different nuclides. The set of all the measurements is also considered, taking account of mutual correlations. The covariational matrix of the complete set of measurements has elements similar in order of

TABLE 2. Covariational Error Matrices for Measurements of Fission Cross Sections

Measurement at	Nuclide	E_n, MeV	σ_f, b	Covariational matrix (%)²			
TU	235U	8,5	1,801	6,12			
TU	235U	2,6	1,214	3,41	2,44		
TU		2,6	1,215		5,17		
TU	239Pu	14,7	2,377	0,92	0,62	0,24	0,24
TU		14,7	2,394		1,02	0,24	0,24
RI		14,7	2,309			1,65	0,65
RI		14,7	2,349				3,64
TU	237Np	14,7	2,226	1,08	0,41	0,53	
RI		14,7	2,214		3,26	0,82	
TU		8,5	2,163			4,40	
RI	233U	14,7	2,254	4,00	2,02		
TU		14,7	2,244		3,48		
RI	242Pu	14,7	2,062	2,90	1,49		
TU		14,7	2,079		2,94		
RI	238U	14,7	1,171	3,98	0,38		
TU		14,7	1,166		2,96		

TABLE 3. Results of Calculating the Mean Cross Sections and Comparison with the Results of Estimates and Data of Other Works Obtained by the Method of Time-Correlated Accompanying Particles

Nuclide	E_n, MeV	σ_f, b	±δ, %	$\pm\delta\sqrt{\frac{x^2}{N-1}}$, %	Data of estimates, σ_f, b; ±δ, %	Experimental results from other work σ_f, b
233U	14,7	2,248	1,7	1,7	2,28±4, ENDL-76	2,085±0,039 [8]
235U	14,7	2,086	0,9	0,9	2,101±4, ENDF-B/V	2,080±0,030 [9]
235U	8,5	1,810	2,5	2,5	1,782±3,5, ENDF-B/V	—
235U	2,6	1,214	1,8	1,8	1,259±3, ENDF-B/V	—
238U	14,7	1,168	1,4	1,4	1,180±4,3, ENDF-B/V	1,149±0,025 [8]
237Np	14,7	2,224	1,0	1,0	2,179±5, INDC (FR)-42/L [10]	—
237Np	8,5	2,163	2,0	2,0	2,165±5, INDC (FR)-42/L [10]	—
239Pu	14,7	2,361	0,8	1,1	2,343±5, INDC (CCP)-166 [10]	2,310±0,021 [8]
242Pu	14,7	2,071	1,5	1,5	2,15±5,5, INDC (CCP)-150 [10]	—

Note. The third column gives the mean values of the cross sections; the fourth and fifth columns give the errors obtained as a result of the analysis.

TABLE 4. Covariational Error Matrices of the Mean Cross Sections for a Complete Set of Measurements over All the Nuclides

Nuclide	E_n, MeV	σ_f, b	Covariational matrix, (%)² × 10⁶										
235U	14,7	2,087	274*	161	159	92	77	83	89	127	67	71	78
235U	14,5	2,097		1040	160	61	53	53	64	75	50	52	75
235U	14,0	2,078			1020	60	53	52	64	74	50	52	74
235U	8,5	1,804				1210	260	40	34	74	170	43	32
235U	2,6	1,223					307	36	30	53	38	32	30
239Pu	14,7	2,360						304	90	140	87	76	72
237Np	14,7	2,221							417	110	197	75	74
233U	14,7	2,243								1190	115	87	120
237Np	8,5	2,165									1570	76	47
242Pu	14,7	2,071										910	46
238U	14,7	1,167											212

659

magnitude to the matrix of ^{235}U measurements (Table 1), and is not given here. The mean values obtained on the basis of this matrix are shown in Table 4, together with the covariational matrix. Note a certain shift in the mean error (in comparison with Table 3) and a pronounced (up to 30%) decrease in error of the individual cross sections, with satisfactory statistical agreement ($\chi^2_{10} = 12.9$).

For comparison with the experimental results of other workers, the correction for attenuation of the neutron flux on the basis of the details of the experiment given in [9] is considered. The results of the present calculations differ by 7%, which is associated with a reduction in the cross section by 0.2-0.4%. This shift (within the limits of the error of the result) definitely indicates the stability of the measurement method employed and at the same time does not remove the problem of mutual comparison of the programs for calculating the corrections.

Comparison of the present data with the results of subsequent measurements by the method of (n, p) scattering [11] and the black-counter method [12] also indicates good agreement.

Thus, it may be noted that except for data on ^{239}Pu, all the results of our measurements are in sufficiently good internal agreement. In addition, the results obtained by the same method in other laboratories are also in excellent agreement [8, 9]. All this means that the method of time-correlated accompanying particles may be regarded as the most reliable for the normalization of "form measurements."

LITERATURE CITED

1. V. Adamov et al., in: Proceedings of the International Conference on Nuclear Cross Sections for Technology, Knoxville, 1979, NBS Special Publication 594, Washington (1980), p. 995.
2. R. Arlt et al., in: Proceedings for the International Conference on Nuclear Cross Section for Technology, Knoxville, 1979, NBS Special Publication 594, Washington (1980), p. 990.
3. R. Arlt et al., in: Neutron Physics. Materials of the Fifth All-Union Conference on Neutron Physics, Kiev, 1980 [in Russian], Moscow (1980), Part X, p. 192.
4. I. D. Alkhazov et al., in: Abstracts of the Proceedings of the Third All-Union Conference on the Metrology of Neutron Radiation [in Russian], Moscow (1982), p. 155.
5. V. N. Dushin, Vopr. At. Nauki Tekh., Ser. Yad. Konst., No. 2(33), 3 (1979).
6. R. Arlt et al., Preprint 05-5-79, Technische Univ. Dresden, Dresden (1979).
7. W. Mannhart, A Small Guide to Generating Covariances of Experimental Data, PTB-FMRB-84, ISSN 0341-6666, Braunschweig (1981).
8. M. Cance and G. Gremier, Nucl. Sci. Eng., 68, 197 (1978).
9. O. Wasson, M. Meier, and K. Duvall, Nucl. Sci. Eng., 80, 882 (1982).
10. H. Lemel, INDL/A Nuclear Data Library for Evaluating Neutron Reaction Data of Actinides (May, 1982).
11. J. Gzirr and G. Sidhu, Nucl. Sci. Eng., 57, 18 (1975).
12. W. Poenitz, Nucl. Sci. Eng., 64, 894 (1977).

USE OF ELECTROSTATIC ACCELERATORS IN NUCLEAR–PHYSICS RESEARCH

B. D. Kuz'minov, V. A. Romanov,   UDC 621.384.653+004.1
and L. N. Usachev*

   Introduction. Electrostatic acclerators (ESA) are presently the most widely used in-
strument in nuclear physics research in the low- and medium-energy ranges. They are also
widely used for investigations in other fields, as well as for solving the most varied applied
problems. This is due to their high energy resolution $(10^{-4}-10^{-5})$, fast and precise tuning
of the energy of the accelerated particles over a wide dynamic range, possibility of accel-
erating ions with arbitrary mass from hydrogen to uranium, favorable conditions for arranging
different pulsed regimes and creating geometrically unique charged-particle beams, simplicity
of operation, and relatively low cost.

   The first steps toward the development of single-stage ESA were taken in the 1930s. Con-
struction of two-stage charge-exchange ESA (tandems) began in the 1950s. The maximum energy
of particles (protons) accelerated on single-stage ESA was in the range 1-6 MeV with a cur-
rent of about 10 μA. The study of nuclear reactions on such ESA was limited to the region
of light and medium nuclei due to the high Coulomb barrier for the heavier nuclei. However,
the possibilities of obtaining monoenergetic fast neutrons on ESA turned out to be excep-
tionally favorable for studying the interaction of neutrons with all accessible nuclei.

   The total energy of accelerated particles on modern tandems is sufficient for investi-
gating all natural nuclei, quantum states with high excitation energy of these nuclei, crea-
tion of new exotic nuclei in endothermic reactions, and emission processes characterized by
high angular momenta and Coulomb fields. As their output energy increased, tandems were no
longer inferior to cyclotrons and linear accelerators with respect to the possibility of ac-
celerating heavy ions, but retained their precision and convenience of use. Tandems are also
used to obtain high-energy neutrons.

   The diagram in Fig. 1 illustrates the dynamics of the evolution of tandems. In the last
10 years, the number of accelerators in this class increased considerably and the potential on
the conductor increased sharply as well.

   There are now hundreds of ESA being used in accelerators or in industry. Many of them
have been operated for several decades. Their widespread use, high reliability, and inten-
sive development are to a large extent due to the constant improvement of the important sub-
units. Recently, a module of a diffusion-welded accelerating tube made of aluminum oxide,
20 cm long and designed for a voltage of 330 kV, was developed. This creates a basis for de-
signing ESA with a potential of 60 MeV on the conductor [1]. New charging systems are being
introduced with a conducting charge carrier, providing voltage stability (±200 eV) and having
a long operational lifetime (up to 20,000 h). Transferring the functions of monitoring and
control of the accelerator operation to a computer opens up extensive possibilities for opti-
mizing the working regimes and increasing their stability [2, 3]. Due to the large stock of
ESA and their long lifetimes, researchers have obtained an enormous amount of scientific in-
formation from different areas of nuclear physics. For example, more than 200 scientific
papers concerning the interaction of neutrons with nuclei were published based on the data
obtained on the EG-1 accelerator at the Physicopower Institute over the 20 years that it was
in use.

   The extensive possibilities of ESA have been further demonstrated in more characteristic
research in the field of nuclear physics, work on measuring nuclear constants required by the
nuclear power industry, and applied work on nuclear microanalysis.

   Research in Nuclear Physics. Due to their unique qualities, ESA turned out to be ex-
tremely convenient for experimentally justified modern fundamental concepts in nuclear phys-

----

*Deceased.

661
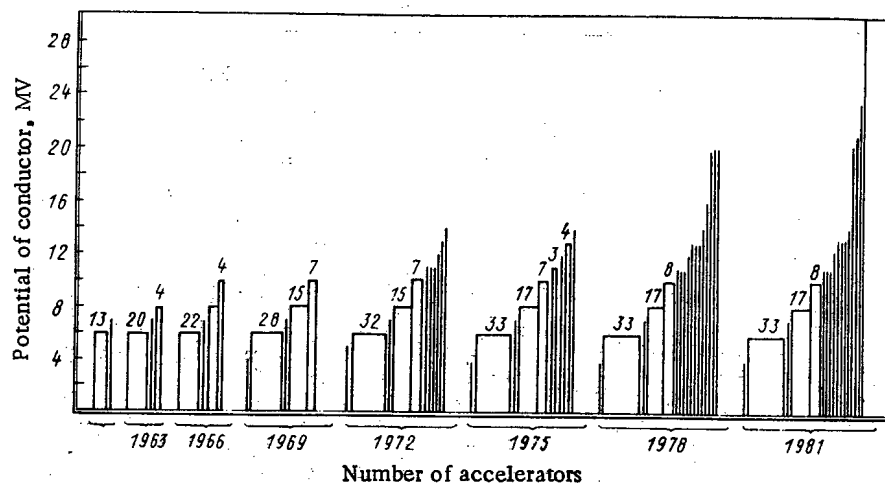
Fig. 1. Dynamics of development of electrostatic charge exchange accelerators (tandems).

ics in the medium- and low-energy ranges. The problems related with studying the structure of nuclei and the mechanisms of nuclear reactions, including such complex phenomena as fissioning of nuclei and interaction of heavy ions with nuclei, are widely studied on ESA.

The properties of time reversal symmetry of nuclear systems were checked in investigations of the forward and backward reactions of the type $^{24}Mg + \alpha \rightleftarrows {}^{27}Al + p$ [4, 5]. As a result, the validity of the mutual conditions imposed on such processes was verified to within fractions of a percent.

The isobaric invariance of nuclear interactions was convincingly demonstrated in investigations of isobar-analog states. Without the high energy resolution and the smooth regulation of the energy of the accelerated particles, achieved in ESA, the study of such states would have been unthinkable. Thus, a beam of protons with energy resolution of 200 eV was used to investigate the spectrum of the analog states in the ^{57}Co nucleus [6].

A large amount of work on ESA is devoted to justifying the applicability of the independent particle model to the nucleus. The main criterion for the applicability of the model was the average mean free path of nucleons in the nucleus, determined from the total cross sections of the interactions of neutrons with nuclei.

The shell model has occupied a strong position in the arsenal of physical models of nuclear structure. The decisive step in its development was the establishment of the comparatively strong spin—orbital interaction in the motion of nucleons in the mean field of the nucleus, which permitted describing quite well the sequence of energy levels. The spin—orbital interaction is manifested in polarization phenomena accompanying collisions of nucleons with nuclei [7, 8]. The potential, acting on a nucleon, depends on its spin orientation relative to the scattering plane. The study of this phenomenon in reactions realized on ESA greatly extended the understanding of spin—orbital interaction.

In studying the spectrum of nuclear states, quantum numbers such as the energy of the states and its spin and parity are of great interest. The first number is determined from the energy balance of the reaction used, while the measurement of the angular correlations of the radiation accompanying a nuclear reaction is a natural method for determining the remaining quantum numbers.

Experiments on proton scattering with high energy resolution should be put into a **separate class.** They are exceptionally valuable for investigating many statistical and nonstatistical nuclear phenomena. Analysis of such data yields rich spectroscopic information on isobar-analog states, the density of levels, force functions, statistical distributions of the reduced width, and distances between levels.

One method for determining the nuclear energy density function is to measure the neutron stripping spectra. Figure 2 shows the typical neutron spectrum, which is obtained by measuring the time of flight of neutrons forming in the reaction (p, n) [9].

The shell model of the nucleus rested for a long time primarily on the experimental data for light and medium nuclei. Combining the high energy of particles accelerated on tandems

662
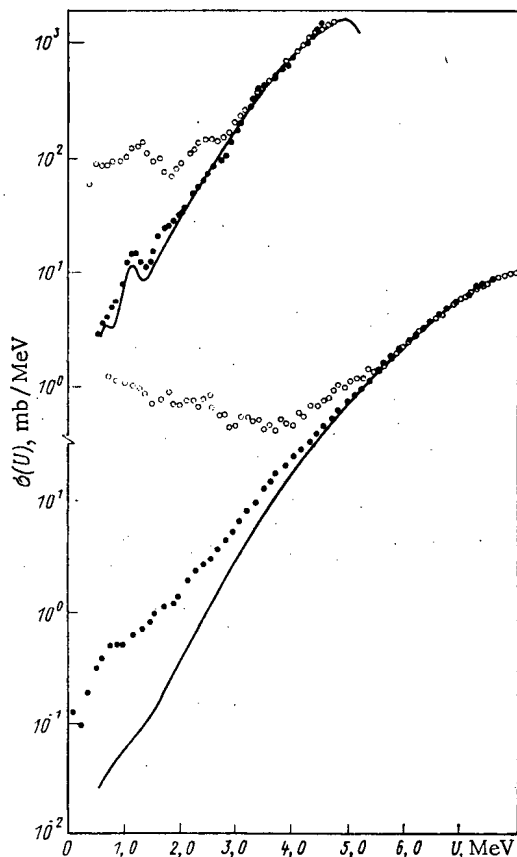
Fig. 2. Spectrum of excitations of the residual nucleus with neutron energy $E_n^0 = 5.34$ MeV and proton energy $E_p^0 = 6$ MeV (upper curves) and $E_n^0 = 8.53$ MeV, $E_p^0 = 9$ MeV (lower curves) in the reactions ^{113}In(n, n')^{113}In (○) and ^{113}Cd(p, n)^{113}In (●). The solid line shows the theoretical calculation using the Hauser—Feshbach model [9].

with the high energy resolution permitted establishing the validity of this model for nuclei close to lead as well. Investigations of individual final states of nuclei in reactions (d, p), (p, d), and (t, α) confirmed the agreement between the distribution of excited states of nuclei close to twice the magic nucleus ^{208}Pb and the theoretical predictions and proved their single-particle nature [10].

To study the single-particle motion, single-nucleon transfer and capture reactions are widely used. The spectra of nuclei, containing a single particle or a single hole above filled shells, give especially convincing proof of the independence of the motion of particles in a nucleus. In nuclei whose shells are close to being filled, the entire force of a (d, p) transition can be concentrated on a single level; this level can then be identified with the corresponding single-particle configuration. In nuclei with several nucleons above filled shells or with a higher energy of excitation, there can exist many levels with corresponding quantum numbers, and the force for a (d, p) transition will be distributed over many states. Figure 3 shows the results of typical investigations of the force function using the reaction (d, p) [11]. In capture reactions or knockout reactions (of the type (p, 2p)), analogous information is obtained on hole states situated below the Fermi level.

Data on the total and differential elastic scattering cross sections and the polarization give quite detailed information on the basic properties of the nuclear potential. Measurements of the total neutron scattering cross sections in the energy range 0.02–3 MeV [12] stimulated the development of the optical model of the nucleus in application to the low- and medium-energy ranges. The optical model, which has well justified itself in applications to the description of scattering of nucleons by nuclei with different degree of deformation and in a wide energy range, has been further developed in describing the scattering of complex particles: deuterons, helium-3 nuclei, and α particles. In recent years this model has been intensively tested for describing scattering of heavy nucleons. In this case the characteristic feature is the very small depth of the real part of the potential well, indicating that only surface nucleons participate in the interaction [13].

The average nuclear potential characterizes a macroscopic system, based on the interaction between nucleons. Experiments on n—p and p—p scattering are concerned with studying these interactions. The investigations establish that the internucleon interactions represent a strong short-range attraction.

663
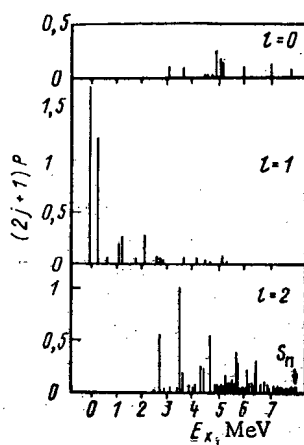
Fig. 3

Fig. 4

Fig. 3. Genealogical factors, determined from the stripping reaction
$^{60}Ni(d, p)^{61}Ni$ [11].
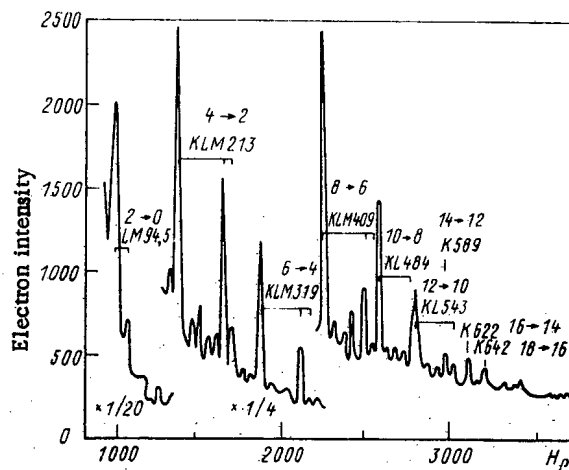
Fig. 4. Spectrum of conversion electrons emitted with the bombardment
of ^{165}Ho nuclei by 6 MeV ^{11}B ions [14].

Understanding of deformation of the nuclear density and the average potential, the problem of coexistence of single particle and collective degrees of freedom, and the analysis of diverse phenomena due to their interaction is given a large place in work of ESA. In studying rotational spectra, the method of Coulomb excitation by heavy ions has turned out to be successful. In this case, multiple Coulomb excitation and population of levels of the rotational band of the ground state of the traget nucleus with high angular momentum is becoming possible. The states of **rotational** bands with high angular momentum are populated no less effectively with the formation of compound nuclei in heavy-ion reactions. Figure 4 shows the results of a study of the rotational band of the ground state of ^{172}Hf in the reaction ^{165}Ho $(^{11}B, 4n)$ [14].

Another remarkable property of nuclear structure is the manifestation of pair correlations. The role of pairing phenomena and of a phase transition in the nuclear fission process was studied in [15]. The change in the internal structure of nuclei (phase transition) as the angular momentum increased in heavy-ion reactions was investigated in [14]. At I = 20, the moment of inertia of the ^{172}Hf nucleus almost doubles and approaches the rigid-body value. Discussion of these problems continues and they must be further studied experimentally.

The study of mechanisms of nuclear reactions has been widely reflected in work on ESA. Confirmation of the validity of the Hauser—Feshback formalism for describing heavy-ion reactions has been one of the enormous achievements of research on ESA. Recognition of equilibrium and nonequilibrium processes is the subject of [12], where the reactions $^{113}In(n, n')$-^{113}In and $^{113}Cd(p, n)^{113}In$, occurring through the same intermediate nucleus, were studied. The energy of the incident particles was chosen from the condition that the intermediate nuclei have the same excitation energy in both reactions. The results of measurements of the neutron spectra for two values of the excitation energy, presented in Fig. 2, indicate the appreciable contribution of direct processes in the case of inelastic neutron scattering. In the case of the reaction $^{113}Cd(p, n)^{113}In$, direct processes are suppressed, which is evidently related with the necessity of recharging the nucleons.

In reactions involving the transfer of a single nucleon, the nucleus itself as well as the final state turn out to be important, which can be observed, e.g., in the reactions $^{208}Pd(p, d)$, $^{186}W(p, d)^{185}W$, $^{172}Yb(p, d)^{171}Yb$ [14]. In the case of lead, the experimental results are described well by the DWBA model. For the other two cases, this model is not applicable at all. The correction to the model consists of including higher-order inelastic processes. In lead, which has a weak collectiveness, the coupling of inelastic channels has an insignificant effect, but in more strongly deformed more collective systems, this coupling can dominate. In the case of tungsten, the contributions of the direct and indirect processes depend strongly on the structure of the final state. The same is true for two-nucleon transfer reactions.
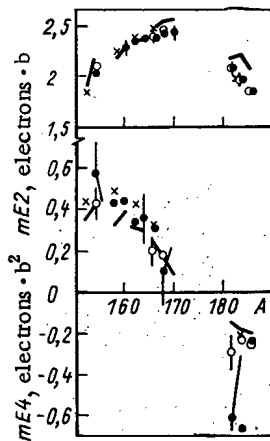
Fig. 5
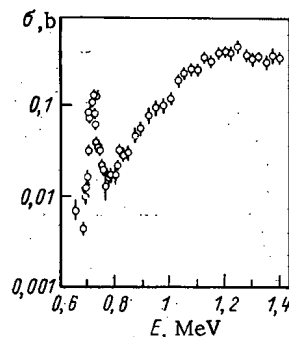
Fig. 6

Fig. 5. Matrix elements of E2 and E4 transitions, obtained from investigations of elastic and inelastic scattering of α particles as a function of the atomic number A: ———, ×) theoretical calculation [17]; ●, ○) experiment.

Fig. 6. Energy dependence of the neutron fission cross section of ^{230}Th nuclei [23].

In elastic transfer reactions of the type $^{12}C(^{13}C, {}^{12}C)^{13}C$, the elastic scattering and neutron transfer amplitudes add coherently. In the case of large collision parameters (scattering at an energy less than the Coulomb barrier), the amplitude of the neutron transfer reaction is very small. However, due to the interference term, the neutron transfer process will be manifested in the cross section of the reaction. This makes it possible to study the tail of the neutron wave function at distances where the amplitude is small and cannot be directly measured [16].

Investigations of the interaction of heavy ions with nuclei on ESA have in recent years been extensively developed. The most characteristic aspects of the heavy-ion reactions are related with the large angular momenta.

From the point of view of obtaining super-heavy nuclei, as well as studying the reverse fission reaction, it is of interest to investigate the coalescence of nuclei. Here entirely new problems and phenomena are being discovered, related with competing processes: fission, deep inelastic processes, the usual direct reactions, and, possible, some qualitatively new processes.

A large number of nucleons participate in the deep inelastic process and most of the starting kinetic energy goes over into other degrees of freedom. However, a strong memory of the input channels remains. Fragments, whose masses are close to the mass of the starting nuclei, are observed in the output channel and their kinetic energy is determined primarily by the Coulomb repulsion energy, while the angular distributions of the reaction products extend along the tangent angle. For other investigations, requiring detailed measurements, including the angular distributions and their extension to the entire Periodic Table, ESA are preferable.

Another interesting aspect of the coalescence reaction, which is being resolved on ESA, consists of the problem of resonance fragmentation. The problem here is that some of the energy of the input channel must correspond to resonant states in the Greiner potential [13] and a resonant division of mass between the fragments, differing from nonresonant division. To study this problem, detailed energy measurements with good resolution are required.

The possibility of obtaining a wide range of accelerated heavy ions on ESA led to considerable successes in establishing the process of Coulomb excitation, including the electric moments of higher order than quadrupole moments, which facilitated the use of this process in nuclear spectroscopy. Figure 5 shows the matrix elements of E2 and E4 transitions, obtained from the excitation functions of the elastic and inelastic scattering of α particles by ^{168}Er, ^{184}W, ^{186}W nuclei [17]. The theoretical calculations reproduce the experi-

665
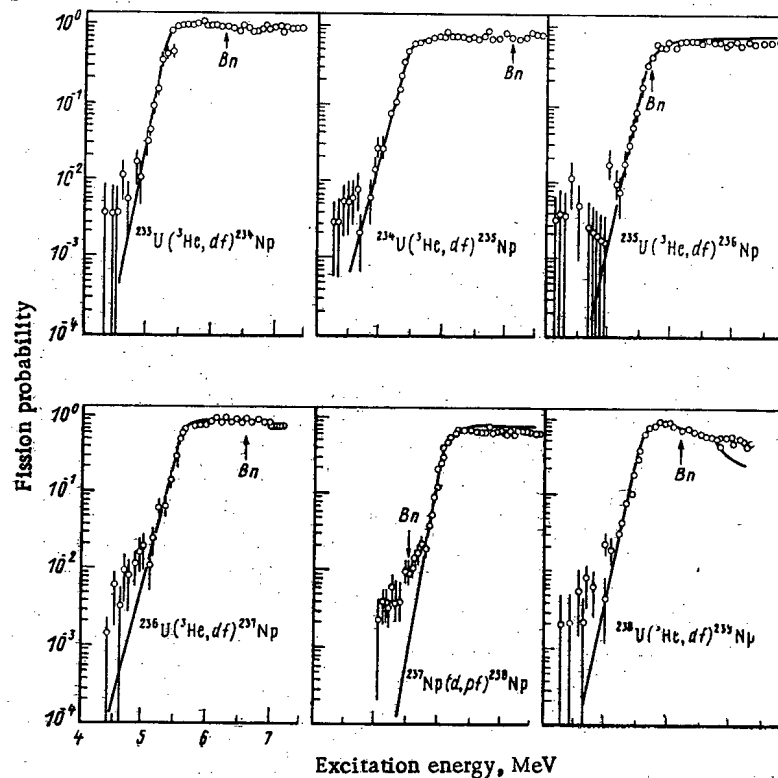
Fig. 7. Fissionability of isotopes of neptunium. Solid lines obtained by statistical calculations; points obtained by experiment [26].

mental results well [18, 19]. These data indicate the absence of differences in the deformations of the nuclear potential and of the charge.

The giant multipole resonance in nuclei remains a subject of investigations on ESA up to the present time [20, 21].

The intensive development of the physics of nuclear fission, related with the appearance of new scientific ideas, has touched upon many problems, among which the structure of the nuclear fission barrier, the dynamics of the nuclear-fission process, and the asymmetry of nuclear fission stand out. ESA appeared as the instrument which to a large extent facilitated successes in the experimental investigations of these problems.

The complicated structure of the potential barrier of fissioning nuclei, due to the influence of the shell effects, is strongly reflected on the fissionability of nuclei at an energy close to the fission barrier. The resonance structure of the cross section of neutron fission of a ^{230}Th nucleus, ascribed within the framework of modern understanding to the vibrational resonance in the second potential well of the deformed nucleus, was first obtained in [22]. In later works [23, 24] the neutron fission cross section of ^{230}Th nuclei was studied with high energy resolution. Figure 6 shows the results of [23], obtained on ESA. In [24], the vibrational resonance itself was studied with an energy resolution of 2.5 keV. An analogous resonance structure of the fissionability of nuclei was obtained in the (d, pf) reaction on ^{233}U, ^{235}U, ^{239}Pu, ^{241}Pu nuclei [25]. Later such investigations acquired extensive scales and in (p, p'f), (d, pf), (t, pf), (α, α'f), (^{3}He, df), (t, αf) reactions the fissionability of several tens of nuclei, many of which had short lifetimes [26, 27] was studied. Figure 7 shows the results of measurements of the fissionability of neptunium isotopes and the results of calculations using the statistical model [26]. Systematic investigations of the fissionability of nuclei and the parameters of the vibrational resonances have permitted constructing a representation of the form of the fission barrier and its transformation in a wide range of values of A and Z of the fissioning nuclei.

Information on the quantum characteristics of the vibrational resonance was obtained from the angular distributions of the fission fragments. This characteristic of the fission process is studied in many papers. Figure 8 presents the results of investigations of the energy dependence of the angular anisotropy of fragments accompanying neutron fission of

666
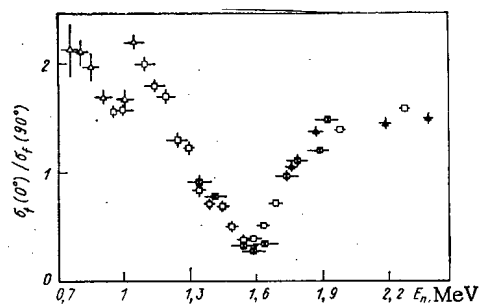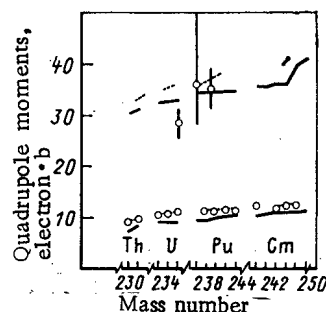
Fig. 8   Fig. 9

Fig. 8. Energy dependence of the angular anisotropy of frag-
ments accompanying neutron fission of ^{232}Th nuclei [28] (the
symbols indicate the data obtained by different authors).

Fig. 9. Quadrupole moments of the ground states of nuclei
(bottom) and fissioning isomers (top); solid lines obtained
by theoretical calculations; points obtained by experiment.

^{232}Th nuclei [28]. In recent years, in measuring the angular distributions of fission frag-
ments, the energy resolution has been considerably improved. Thus, results of measurements
of the angular distribution of fragments accompanying neutron fission of ^{230}Th nuclei obtained
on ESA with energy resolution of 2.5 keV are presented in [28]. The totality of the experi-
mental data on the integral and differential fission cross sections of thorium isotopes does
not fit into the double-hump model of the fission barrier. The potential energy surface ac-
companying deformation of these nuclei apparently acquires a more complicated relief.

Investigations of fissioning isomeric nuclei were no less intensive. Careful measurements
of the lifetime of shape isomers permitted judging not only the depth of the second potential
well, but also the presence of the process of nuclear fission from excited isomeric states.
A drop in the limit of the recorded lifetime down to 5 psec made possible the observation of
shape isomers with two different lifetimes [29, 30], differing by an excitation energy of 1.3
MeV for even-even nuclei and by 0.2-0.3 MeV for even-odd nuclei for several nuclei. The short-
lived isomers in these two cases are ascribed to excitation of two-quasiparticle and single-
particle configurations in the second well, respectively.

To estimate the deformation of the shape-isomer nucleus, complicated experiments investi-
gating the rotational excitations of the fissioning isomers were performed [31]. The results
indicate that the moment of inertia of the fissioning nucleus in the isomeric state greatly
exceeds the moment of inertia in the ground state.

As these investigations evolved, the quadrupole moments of the fissioning isomers were
measured. The technique for performing the measurements, based on some atomic phenomena, is
described in [32, 33]. The quadrupole moments of the ground states of nuclei and fissioning
isomers are compared in Fig. 9. The results of the investigations performed indicate that
the fissioning isomers correspond to deformations of the nucleus, with which the presence of
a second well of the potential barrier is expected.

One of the important problems in the physics of nuclear fission is the problem of the
nature of the mass asymmetry of the fission fragments. Diverse investigations were performed
in order to coarify the stage of the fission process at which formation of the massive fis-
sion fragments occurs. In several works [34-37], measurements of the dependence of the angu-
lar anisotropy of the fragments on their masses were undertaken in order to obtain proof of
the formation of fragments according to the mass at the saddle point. Reactions involving
neutron fissioning of heavy nuclei [34-36] and reactions of the type (d, pf) and (t, pf) in
lighter nuclei [37] were used, but a unified point of view of this problem has not been de-
veloped. Figure 10 shows the mass distribution of the fragments accompanying neutron fission
of ^{239}Pu nuclei in the energy range from thermal energies to 6 MeV [38]. The insignificant
changes in the forms of the mass distribution of the fragments most likely indicate that they
were formed at later stages than the saddle point.

The dynamics of the fission process on the path away from the saddle point up to the
point of separation is attracting increasingly more attention. In experiments performed on
ESA, efforts are being made to study the energy dependence of the fine structure of the
properties of the fission fragments and the energy exchange between the collective and in-

667
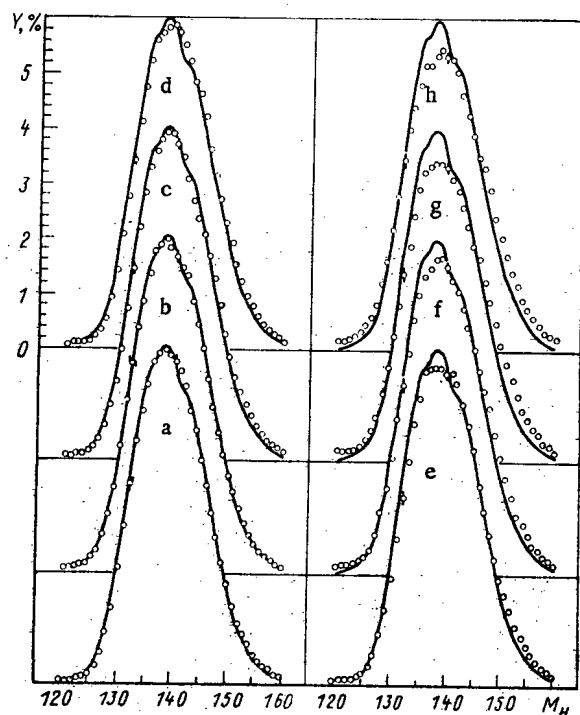
Fig. 10

Fig. 11

Fig. 10. Mass distribution of fragments accompanying fissioning of ^{239}Pu nuclei by neutrons with energies of 0.16 (a), 0.6 (b), 0.82 (c), 1.72 (d), 2.72 (e), 3.5 (f), 4.48 (g), and 5.3 MeV (h). Solid lines show the fissioning by thermal neutrons [38].
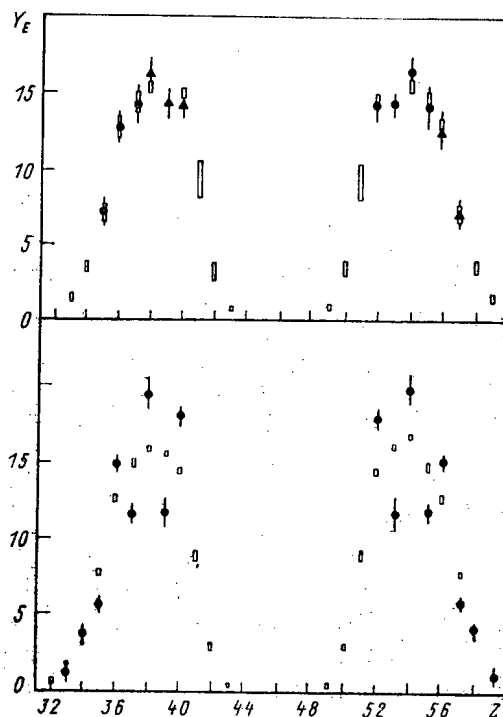
Fig. 11. Output of fragments as a function of the change in fissioning of ^{235}U nuclei by thermal neutrons (bottom) and 3-MeV neutrons (top): the rectangles show the calculation neglecting pairing effects; •, ▲) measurements in [39].

ternal degrees of freedom. The presence of effects that are explained by pair correlations during the descent away from the barrier indicates the small excitation energy of the fissioning nucleus in the motion toward the point of separation, and they can be interpreted as being the result of adiabatic motion. Such effects should disappear as the excitation energy of the fissioning nucleus increases. Figure 11 shows the results of [39], where the effect of the excitation energy of the fissioning nucleus on the intensity of the fine structure of the charge distribution of the fragments was investigated for neutron fissioning of ^{235}U.

The results of investigations of the redistribution of the total energy between the kinetic energy and the excitation energy of fragments, observed from the change in the excitation energy of the fissioning nucleus, are likewise used to judge the dynamics of the descent of the nucleus away from the barrier. Figure 12 shows the results of the measurements of the kinetic energy of fragments $\bar{E}_k$ and the average number of prompt fission neutrons $\bar{\nu}_p$, characterizing the excitation energy of the fragments, accompanying neutron fission of ^{232}Th nuclei. The redistribution of the total energy between the kinetic energy and the energy of excitation of the fragments occurs over the entire energy range investigated.

It should be noted that we have presented only selected nuclear-physical papers and they by no means pretend to give a comprehensive description of the fundamental investigations of the nucleus in the low- and medium-energy range. The material was selected so as to reveal the extensive possibilities of ESA for physical investigations.

Measurements of Nuclear Data, Characterizing Interaction of Neutrons with Nuclei. The requirements for nuclear data for use in different areas of science and technology are very extensive and have not yet been satisfied. The more nuclear physics enters power production and industry, the greater are the requirements on the reliability and the depth and breadth of knowledge concerning various types of nuclear transformations. The existing requirements for nuclear data can be judged from the "International List of Requirements" published by the International Atomic Energy Agency [40], in which all information from many countries is collected.

668
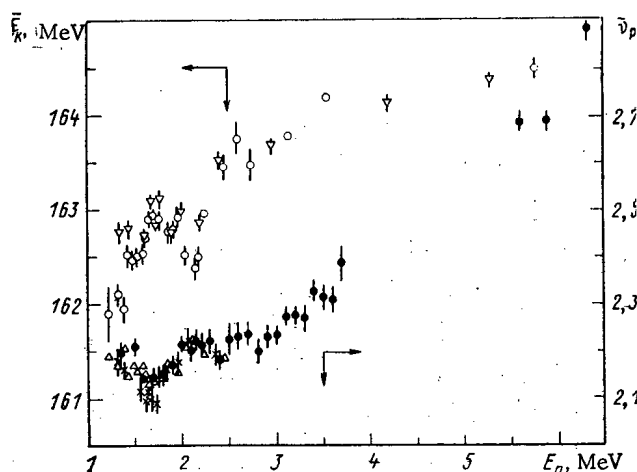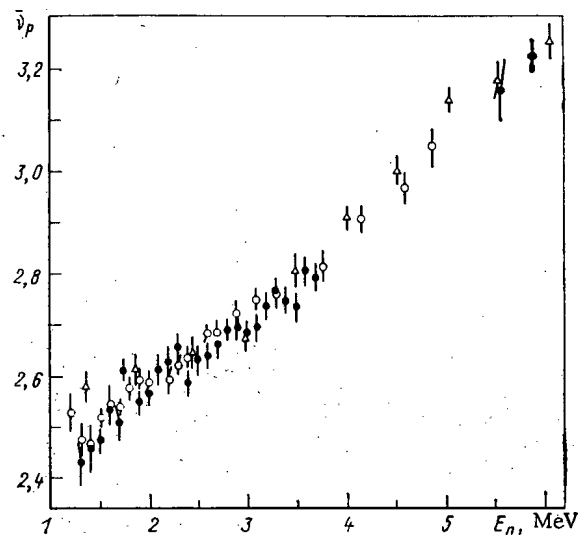
Fig. 12

Fig. 13

Fig. 12. Energy dependences of the average number of prompt neutrons $\bar{\nu}_p$ and the average kinetic energy of fragments $\bar{E}_k$ accompanying neutron fissioning of ^{232}Th nuclei (the symbols indicate data obtained by different authors).

Fig. 13. Energy dependence of the average number of prompt neutrons accompanying neutron fission of ^{238}U nuclei: O, ●, △) data of different authors.

It is difficult to imagine the successful development of physical concepts in nuclear power without the enormous work on investigations of interactions of neutrons with nuclei, performed on sources of monoenergetic neutrons or neutrons with a "restricted white" spectrum, the basis of which are ESA. Thus, the complex of accelerators at the **Physicopower Institute,** whose parameters are presented in Table 1, in studying the reactions ^{3}H(p, n), Li(p, n), ^{2}H(d, n), ^{3}H(d, n) permits obtaining monoenergetic neutrons with smoothly regulated energy in the range 0-20 MeV. The ESA as an instrument for neutron investigations is characterized by a favorable relation of the effect observed to background and extensive possibilities for forming pulsed neutron fluxes. We shall examine the possibility of using ESA to measure nuclear data primarily on examples of investigations of the interaction of neutrons with ^{238}U nuclei. Uranium 238 is an important component of power reactors and serves as a raw material for the production of ^{239}Pu nuclei. In this connection, all the partial-processes involved in the interaction of neutrons with ^{238}U nuclei have been carefully studied.

The fission cross section and the average number of prompt fission neutrons characterize the degree to which ^{238}U nuclei participate in the chain reaction and are reflected in the coefficient of breeding of nuclear fuel. Measurements of the fission cross section of ^{238}U on ESA were performed over a wide range of energies. In the measurements, both the constant and pulsed operating modes of the accelerators were used. The resolution of the neutron energy was 30-150 keV. The possibility of measuring the fission cross sections on ESA with a resolution of 2.5 keV was demonstrated in [28]. The admissible mass of the specimen used in the case of investigations of highly radioactive nuclei is severely restricted. This does not, however, exclude the possibility of measuring the fission cross sections of such nuclei of ESA. Thus, the fission cross section of ^{242}Cm was measured on a specimen with a mass of 8 ng in [41].

Figure 13 shows the results of investigations of the energy dependence of the average number of prompt neutrons in fissioning of ^{238}U nuclei. In these investigations, different operating modes of ESA were also used, depending on the method used to perform the measurements and the range of the energy of neutrons giving rise to fissioning.

For reactor physics it is important to know not only the average number of prompt neutrons, but also their spectra, since the value of the neutron in the reactor depends on its energy. Measurements of the spectra of prompt neutrons accompanying fissioning of ^{238}U nuclei by monoenergetic neutrons with energies in the range 2.5-9 MeV were performed in [42]. Kornilov et al. used the time-of-flight method both without recording the fission event (2.5 MeV) and using an ionization chamber to record the fission fragments.

TABLE 1. Characteristics of Accelerators
at Physicopower Institute

Working parameter	Type of accelerator				
	ÉG-2.5	ÉG-1	ÉGP-10M	KG-2.5	KG-0.3
Maximum energy of accelerated particles, MeV	2,6	5,0	10	2,2	0,25
Energy stability, %	0,01	0,05	0,1	0,1	0,5
Accelerated particles	H, D, Ar, He, O_2, N	H, D	H, D	H, D	D
Operating regime	Continuous pulsed	Continuous pulsed	Continuous pulsed	Continuous	Continuous pulsed
Proton current at target, μA constant/pulsed	50	50/800	12/500	to 500	700/800
Pulse repetition frequency	—	0,1—1,2 MHz 1—30 kHz	1; 5 MHz	—	1,25; 2,5; 5; 10; 20MHz
Duration of current pulses	—	2 nsec 1 μsec	1 nsec	—	3nsec
Beam size at target, mm	0,1—5	5	5	to 20	8

Inelastic scattering of neutrons plays a considerable role in the formation of the stationary spectrum of neutrons in the reactor. This phenomenon is also used to moderate fast neutrons in shielding structures. The measurement of double differential cross sections of inelastic scattering of neutrons by fissioning nuclei is a complicated procedure. In [43, 44], the method of measuring the time of flight of the scattered neutrons was used to investigate the excitation function of separate levels accompanying the inelastic scattering of neutrons by ^{238}U nuclei. In [45], the excitation function was investigated by the method of recording γ radiation from transitions out of the excited into the low-lying states. The spectra of neutrons scattered inelastically by ^{238}U nuclei at an energy when exictation is possible in the region of overlapping levels was investigated in [46]. Kornilov et al. note the superposition of two neutron-emission mechanisms: the direct and equilibrium mechanisms.

The process of radiative capture of neutrons by ^{238}U nuclei determines the production of ^{239}Pu nuclei. The extensive methodological possibilities, achieved with work on ESA, were used in measuring the cross section of this process. An activation method was used in [47] to perform the measurements. The pulsed operational regime of the accelerator was used in [48]. Neutrons with a continuous spectrum in the energy range 0.02-0.4 MeV were obtained in a thick lithium target. The energy of the neutrons was separated out by measuring the time of flight. For energies up to 3.5 MeV, the measurements were performed with monoenergetic neutrons. The acts of radiative capture of neutrons were recorded using the prompt γ emission. In measuring the capture cross section on small specimens of highly radioactive nuclei, the natural kinematic collimation of the beam of neutrons, forming in the reactions Li(p, n) and ^{3}H(p, n) were used.

During reactor operation, actinides, many of which as a result of their high radioactivity create difficulties in storage, transportation, and reprocessing of nuclear fuel, are accumulated. The investigation of the entire chain of nuclear transformations leading to the formation of such actinides is an important aspect of the work in the nuclear data area. In particular, the reaction (n, 2n) on ^{238}U nuclei is the first step in the formation of ^{236}Pu nuclei, after which a decay leads to the formation of ^{232}U. Figure 14 shows the results of measurements of the energy dependence of the cross section of the reaction ^{238}U(n, 2n), obtained by three methods radiochemically [49], by activation [50], and by measuring the multiplicity of neutrons using a total absorption detector [51]. The good agreement of the results obtained by different methods indicates the absence of significant systematic errors.
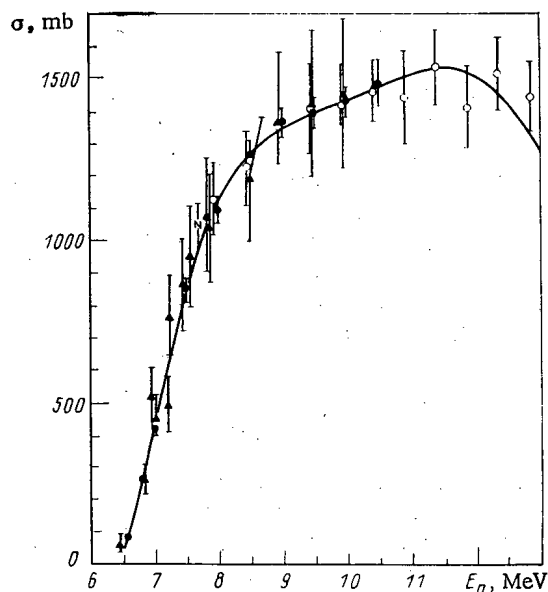
Fig. 14

Fig. 15

Fig. 14. Cross section of the reaction ^{238}U(n, 2n): △) data of [49]; ●) [50]; ▲) [51]; ———) estimate.
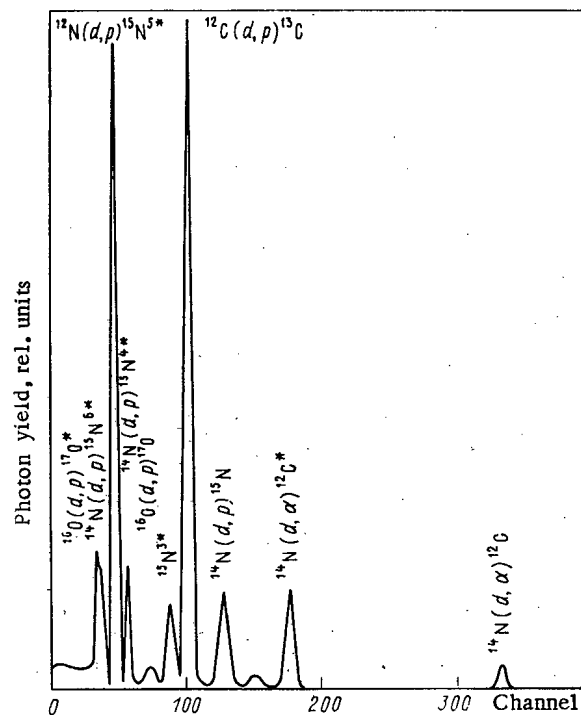
Fig. 15. Energy spectrum of protons and α particles, forming when tantalum nitride is bombarded with deuterons [55]: E_α = 1200 keV, 23.7 keV/channel.

The formation of such gaseous products as hydrogen, tritium, and helium accompanying the interaction of neutrons with nuclei can affect the technological characteristics of the structural materials, while tritium, in addition, is dangerous for the environment. In this connection, numerous reactions accompanying the formation of these products have been studied on ESA [52].

The examples presented indicate the extensive possibilities of ESA for measuring most nuclear constants required for nuclear power.

Use of Ion Beams to Analyze the Density and the Profile of the Distribution of Elements or Isotopes. Beams of ions, accelerated on ESA, are widely used to analyze the density and profile of the distribution of elements or separate isotopes, characterizing the phenomena of interest (analysis of impurities in materials, analysis of surfaces in investigations of corrosion, diffusion, electrolytic polishing, ion implantation, etc., analysis of the profile of the elemental distribution in different specimens ranging from lunar to biological). Both the activation method and the method of recording prompt emission accompanying nuclear reactions are used for the analysis.

The wide range of accelerated ions and the stable and well-reproducible beams with accurately set and easily varied ion energies are qualities of ESA that create favorable conditions for performing accurate and exact measurements by the method of activation analysis. To determine the hydrogen and deuterium content by the activation method, beams of heavy ions of lithium and boron are used. The limit of the sensitivity of the determination of the hydrogen and deuterium impurities that has been achieved is about 10^{-7} g/g. In analyzing the content of lithium, beryllium, boron, carbon, nitrogen, and oxygen, reactions of the type (p, α), (d, 2n), (t, n), (α, 2n) are used. The limit for recording impurities of these nuclei that has been achieved is (1-5)·10^{-10} g/g. The sensitivity of the activation method to determination of heavy ions is somewhat lower: up to 10^{-8} g/g. A detailed review of the possibilities of using charged particles for activation analysis is given in [53].

Recording prompt emission, accompanying nuclear reactions, greatly increased the efficiency of the analysis and extends the range of problems that can be solved with its help. In many cases the energy balance of nuclear reactions is high (∿10 MeV), and the energy of

671
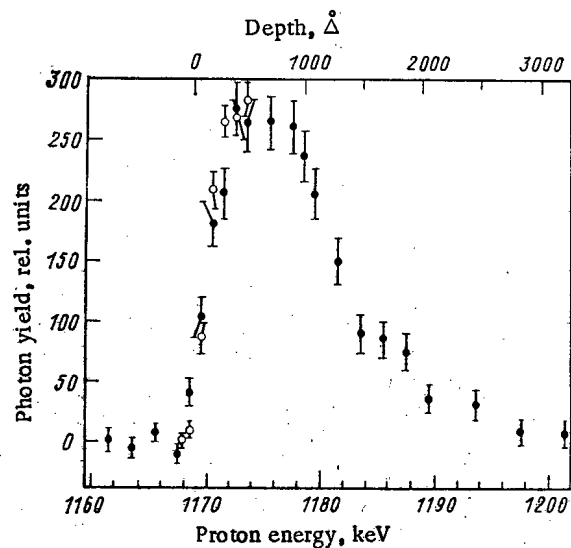
Fig. 16. Profile of neon implanted into tantalum, determined according to the resonance reaction $^{20}Ne(p, \gamma)^{21}Ne$ [56]: $\bigcirc$, $\bullet$) obtained by experiment.

reaction products is correspondingly high, which makes it easier to detect them. However, even reactions with negative energy balance have their advantages, since they occur only at energies above threshold. This circumstance opens up the possibility of reliable identification of nuclei and studying their distribution over the thickness of the specimen. The energy dependence of the cross sections of reactions initiated by charged particles can be smooth and can have a resonance character. The latter case is especially convenient for studying the distribution of nuclei over the thickness of a specimen using data on the loss of energy by charged particles in matter. The sensitivity of the analysis based on the method of recording prompt radiation can reach 10^{-10} g ($5 \cdot 10^{12}$ atoms). When probing a thickness of several micrometers, a resolution of 0.1 μm is achieved.

In recording scattered charged particles (backscattering method), the scattering nuclei are identified according to the energy loss and by the kinematic conditions of the experiment. The spectrum is formed as a result of energy losses by protons in the matter prior to scattering, energy losses accompanying scattering, and energy losses as the proton leaves the layer of matter [54]. The method of backscattering is also used to study the topology of the surface of a specimen. In this case the surface of the specimen is scanned by a well-formed beam of accelerated particles (beam diameter 2-3 μm). The combination of the technique of backscattering with channeling is widely used to analyze structural disorder in metals and semiconductors, arising as a result of various interactions, including ion implantation.

The diverse nuclear reactions accompanied by emission of charged particles [(p, d), (p, t), (p, α), (d, p), (^6Li, x), (^{11}B, α)] have found applications in the analysis of the content of nuclei up to phosphorus. For heavier nuclei these reactions are rarely used, since the Coulomb barrier decreases the yield of charged particles. Figure 15 [55] shows the spectrum of protons and α particles forming when a thin layer of tantalum nitride is bombarded with deuterons. These data permit judging the isotopic composition of nitrogen, as well as the presence of impurities of other elements.

Among reactions accompanied by the emission of neutrons, the ones that are most often used for analysis are (p, n), (d, n), (^3H, n), (α, n). This method is primarily used to analyze admixtures of nuclei lighter than neon. The (α, n) reactions are used to determine the isotopic concentration according to the neutron yield. The structure of the profiles is estimated from the neutron spectra using the (p, n) and (d, n) reactions, which are accompanied by the formation of specific energy groups of neutrons. The thickness of the layers is determined from the form of the energy dependence of the neutron yield near the threshold of endothermic reactions. The sensitivity of the method of analysis reaches the level of five parts of impurity per million. When using reactions accompanied by emission of γ radiation for the analysis, it is not necessary to introduce significant corrections for energy losses or attenuation of the intensity of the output radiation, which greatly increases the precision of the results obtained. Usually, the reactions (p, γ), (d, γ), (^3H, γ), (^3He, γ), (α, γ), (^7Li, γ), (^{15}N, γ), (^{19}F, γ), (^{16}O, γ), with whose help elements lighter than molybdenum are primarily analyzed, are used. Many of these reactions have very narrow resonances, less than the energy spread of the particles in the beam. This circumstance presents ideal possibili-

ties for studying the profile of the distribution of impurities as a function of depth. An example of the application of γ spectroscopy to elemental analysis is shown in Fig. 16 [56]. In this paper the resonance reaction $^{20}Ne(p, \gamma)^{21}Na$ was used to determine the profile of the distribution of neon implanted into tantalum. A big advantage of the method of recording emission is the possibility of revealing the presence of a large number of elements in the impurity simultaneously without destroying the specimen. For $Z > 15$ it is possible to obtain information on traces of impurities with concentrations of about 10^{-6}. The limit of the sensitivity of this method of analysis achieved so far constitutes $\sim 0.3 \cdot 10^{-12}$ g.

The method of exciting x-rays by ions (protons, α particles, heavy ions) accelerated on ESA has been widely used in elemental analysis, especially after the appearance of high-resolution silicon—lithium detectors. Its main advantage over the method of exciting x rays by electrons is the absence of a bremmstrahlung background. With the help of the silicon—lithium detectors, it is possible to implement spectrometry of K radiation, excited in elements from aluminum to zirconium, and of L radiation, excited in elements from bromine to uranium. As a result, the method of exciting the characteristic x-ray radiation by accelerated ions greatly extends the range of elements that can be analyzed. With this method it is possible to perform a quantitative analysis of traces of many elements simultaneously, with the impurity content ranging from 10 to 100 parts per million.

Conclusions. In a short review it is difficult to give a complete picture of the nuclear-physical investigations performed on ESA. The examples presented indicate the enormous range of subjects and the techniques used in these investigations. The contribution of ESA to the development of modern concepts of nuclear structure and nuclear reaction mechanisms is incomparably greater than any other instrument used in nuclear physics. These instruments also turned out to be exceptionally useful for solving applied problems and for investigations in different areas of science. The transfer of research techniques based on the use of ESA and concepts of nuclear physics to atomic and molecular problems has been reflected in optical spectroscopy, in investigations of the Lamb shift in strongly ionized heavy ions, in diverse experiments on atom—atom and atom—molecule scattering, and in investigations of collisions between charged particles and of charge transport processes.

Electrostatic accelerators have contributed to the success of such areas of science as astrophysics, atomic physics, solid-state physics, materials engineering, biophysics, and other areas.

LITERATURE CITED

1. R. Herb, Nucl. Instrum. Method, 122, 267 (1974).
2. P. Thieberger et al., ibid., 184, 121 (1981).
3. V. M. Mukhametshin et al., in: Proceedings of the 7th All-Union Conference on Charged Particle Accelerators, Vol. 2, Dubna (1981), p. 309.
4. D. Bodansky et al., Phys. Rev. Lett., 16, 589 (1966).
5. W. Witsch, ibid., 19, 524 (1967).
6. E. Arai, Nucl. Phys. A, 378, 259 (1982).
7. W. Trachslin and L. Brown, ibid., 101, 273 (1967).
8. C. Kelsey et al., ibid., 51, 395 (1964).
9. O. I. Sal'nikov et al., in: Proceedings of the 5th All-Union Conference on Neutron Physics, Part 2, TsNIIatominforma, Moscow, p. 144.
10. N. Stein, in: Proceedings of Conference on the Properties of Nuclear States, University of Montreal Press (1969).
11. R. Fulmer et al., Phys. Rev. B, 133, 955 (1964).
12. H. Barschall, ibid., 86, 431 (1952).
13. D. Bromley, Nucl. Instrum. Methods, 146, 1 (1977).
14. F. Stephens et al., Nucl. Phys., 63, 82 (1965).
15. D. L. Shpak et al., Yad. Fiz., 13, No. 5, 950 (1971).
16. A. Gobbi et al., Nucl. Phys. A, 112, 537 (1968).
17. I. Lea et al., Phys. Rev. C, 12, 1483 (1975).
18. U. Gotz et al., Nucl. Phys. A, 192, 1 (1972).
19. H. Flocard et al., Phys. Lett. B, 46, 304 (1973).
20. S. Hanna et al., Phys. Rev. Lett., 32, 114 (1974).
21. K. Ebisawa et al., Bull. Am. Phys. Soc., 20, 629 (1975).
22. B. M. Gokhberg et al., Dokl. Akad. Nauk SSSR, 128, 1157 (1959).
23. G. James et al., Nucl. Phys. A, 189, 225 (1972).

24. B. Bruneau, Sc. Thesis, Bordeaux (1980).
25. J. Pedersen and B. D. Kuzminov, Phys. Lett. B, 29, 176 (1969).
26. B. Back, O. Hansen, et al., in: Proc. Conf. on Physics and Chemistry of Fission, Vol. 1, Rochester (1973), p. 3.
27. H. Britt, in: Proc. Conf. on Physics and Chemistry of Fission, Vol. 1, Julich (1979), p. 3.
28. A. Michaudon, in: Proc. Conf. on Some Aspects of Nuclear Fission, Oxford, July 1-3, 1981, CEA-N-2232.
29. P. Limkilde and G. Sletten, Nucl. Phys. A, 199, 504 (1973).
30. V. Metag et al., Nucl. Instrum. Meth., 114, 445 (1974).
31. H. Backe et al., Phys. Rev. Lett., 42, 490 (1979).
32. G. Ulfert et al., Nucl. Instrum. Meth., 148, 369 (1978).
33. V. Metag and G. Sletten, Nucl. Phys. A, 282, 77 (1977).
34. J. Meadows, Phys. Rev., 117, 1817 (1969).
35. V. G. Vorob'eva et al., Yad. Fiz., 10, 491 (1969).
36. V. G. Vorob'eva et al., ibid., 26, 962 (1977).
37. E. Konecny et al., in: Proc. Conf. on Physics and Chemistry of Fission, Vol. 1, Rochester (1973), p. 13.
38. N. I. Akimov et al., Yad. Fiz., 13, 484 (1971).
39. G. Mariolopoulos et al., Nucl. Phys. A, 361, 213 (1981).
40. World Request List for Nuclear Data, WRENDA 81/82, IAEA, Vienna (1981).
41. A. N. Smirnov et al., Preprint IAE-3438, Moscow (1981).
42. N. V. Kornikov et al., in: 5th All-Union Conf. on Neutron Physics, Part 3, TsNIIatominforma, Moscow (1980), p. 104.
43. A. Smith, Nucl. Phys., 47, 633 (1963); P. Guenther and A. Smith, Nucl. Crocc. Sec. and Technol., Washington (1975), Vol. 2, p. 862.
44. P. E. Vorotnikov et al., in: Proc. 5th All-Union Conf. on Neutron Physics, Part 2, TsNIIatominforma, Moscow (1977), p. 119.
45. B. G. Kazyula et al., Problems in Atomic Science and Technology, No. 4, Ser. Yad. Konstanty (1980), p. 14.
46. N. V. Kornilov et al., in: Proc. 5th All-Union Conf. on Neutron Physics, Part 2, TsNIIatominforma, Moscow (1980), p. 44.
47. A. N. Davletshin et al., At. Energ., 48, No. 2, 87 (1980).
48. W. Poenitz, Nucl Sci. Eng., 57, No. 4, 300 (1975).
49. J. Knight, R. Smith, and B. Warren, Phys. Rev., 112, 259 (1958).
50. P. Raich et al., in: Proc. 5th All-Union Conf. on Neutron Physics, Part 1, TsNIIatominforma, Moscow (1980), p. 236.
51. J. Frehaut and G. Mosinski, in: Proc. Conf. Nucl. Cross Sect. Technol., Washington (1975), Vol. 11, p. 855.
52. V. M. Bychkov et al., Cross Sections of Neutron-Initiated Threshold Reactions [in Russian], Énergoizdat, Moscow (1982).
53. Ch. Engelmann, At. Rev., Suppl., 2, 107 (1981).
54. R. Edge and U. Bill, Nucl. Instrum. Meth., 168, 157 (1980).
55. G. Amsel et al., Rev. Phys. Appl., 3, 373 (1968).
56. Z. Switkowski et al., J. Nucl. Mater., 78, 64 (1978).

AN EFFECTIVE-DOSE DOSIMETER BASED ON THERMOLUMINESCENT
ALUMINOPHOSPHATE GLASSES

I. A. Bochvar, T. I. Gimadova,
I. B. Keirim-Markus, N. A. Sergeeva,
and V. V. Yakubik

UDC 539.1:535.377

It is generally accepted that allowance must be made for recovery processes in the body on repeated or prolonged exposure to ionizing radiation at a dose level that could produce acute radiation sickness [1, 2]. Therefore, damage to the body under prolonged irradiation cannot be evaluated from the total dose received during the irradiation time. The recovery processes mean that some of the radiation damage is compensated for before the start of the next irradiation. As a result, the organism can withstand irradiation to a larger total dose than in a single application. To evaluate the state of the human body under conditions of prolonged irradiation, one must be able to record the effective dose, which is the dose corresponding to the observed injury. The effective dose characterizes the possible unfavorable consequences from irradiation and enables one to take detailed medical measures.

In practice, the measurement of effective dose will be important in prolonged space flights, when the spaceman may be subject to repeated exposure to solar flares, and it is also extremely necessary in other cases where it is potentially possible for prolonged irradiation to high doses to occur. The Blair—Davidson hypothesis on post-irradiation recovery indicates [1] that

$$D_{ef} = D\left[f + (1-f)\cdot e^{-\beta t}\right],$$

where D is the dose received over a short period at time $t = 0$; f, irreversible part of the injury ($f = 0.1$ for a man subject to γ rays); β, recovery rate ($\beta = 0.001$ per hour for a man); and t, time after a single irradiation, h.

Akoev [2] has considered the effects of total dose, dose rate, and degree of protracted irradiation as regards recovery. Calculations may be performed on the effective dose from the formulas given by Davidson and Akoev, which show that under real irradiation conditions the difference between the two methods is only 10-20%. Therefore, the Blair—Davidson model has been used in devising a dosimeter for measuring effective dose.

The readings from the dosimeter at any instant after the start of irradiation should correspond to the effective dose no matter what the distribution of the radiation dose in time, so the reduction in the readings should correspond to the law followed by the effective dose in time. We therefore sought to develop an aluminophosphate thermoluminescent glass whose decay of readings fitted this.

If we know how the detector reading varies with time, and also the frequency factor P_0, one can determine the form of the elementary thermoluminescence curve (TLC) for a hypothetical detector and the position of this on the temperature axis. We used the value of P_0 given in [3] for aluminophosphate glasses and assumed that the probability of repeated trapping is small, from which we calculated the TLC for a heating rate of about 0.3 deg·sec^{-1} (Fig. 1). Having derived the TLC, we considered the scope for synthesizing glasses with these properties.

We considered glass compositions in the following systems: $MgO-Al_2O_3-P_2O_5$, $MgO-Na_2O-Al_2O_3-P_2O_5$, and $Na_2O-Al_2O_3-P_2O_5$. Manganese was the luminescence activator in all cases.

The element from the first group that was introduced into the glass was chosen as sodium. It is undesirable to use lithium because this increases the sensitivity to thermal neutrons. The use of lithium depleted in ^6Li complicates the preparation of material for synthesizing the glasses and makes the latter more expensive. It is undesirable to use potassium because

---

675
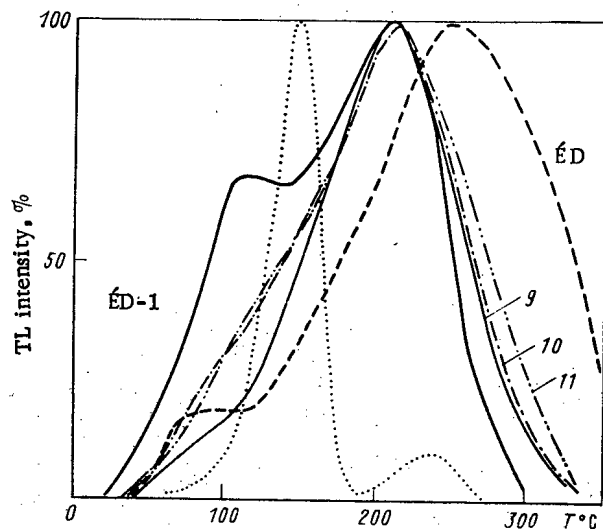
Fig. 1. Thermoluminescence curves for a hypothetical detector (dotted line) and for glasses of various compositions (see Table 1 for glass compositions); in Figs. 1, 2 the TL intensities are given as percent of the maximum intensity.

of its natural radioactivity, which leads to the accumulation of a dose in the glass on prolonged storage. It is undesirable to use cesium because of its high atomic number and the substantially worse chemical stability of glasses containing cesium.

The glasses were synthesized using metaphosphates as raw materials, since this simplified the technology and also produced glasses with parameters that were more stable from batch to batch and with better homogeneity within a single batch [4]. These features are important in the large-scale production of glass detectors.

The glasses were synthesized under laboratory conditions by means of a technology maximally approaching that used under factory conditions in producing phosphate glasses. We used the metaphosphates of aluminum (Technical Specification (TU) 6-09-4031-75) and magnesium (TU 10P-60-72), while the other components were used as oxides of pure or analytical grades. The glasses were synthesized in corundum crucibles in an electric oven with silite heaters. The mixtures were inserted when the oven space had reached the temperature required to synthesize the given glass composition (1200-1350°C). The glass mass was stirred with a silica stirrer and was poured as plates and annealed.

In the $MgO–Al_2O_3–P_2O_5$ system, the glass of composition $MgO \cdot P_2O_5$ (85 mass %), $Al_2O_3 \cdot 3P_2O_5$ (13 mass %), and MnO_2 (0.1 mass %) had the TLC at the lowest temperature. However, the half width of the TLC (150°C) and the position of the maximum (about 250°C) did not correspond to the required parameters of the TLC (Fig. 1). In the other two systems it was also impossible to make glasses with TLC substantially displaced to lower temperatures and with smaller half widths. The TLC maximum in these glasses could not be moved below 220°C. The TLC most displaced to the low-temperature range (half width 110°C, maximum at 220°C) occurred with a glass of composition $Na_2O \cdot P_2O_5$ (75 mass %), $Al_2O_3 \cdot 3P_2O_5$ (25 mass %), MnO_2 (0.1 mass %), which is composition 9 in Table 1, but this was of inadequate chemical stability, while the properties of the glass were unstable, so it cannot be recommended for use in dosimeters. The glasses of compositions 10 and 11 has approximtely the same TLC parameters (half width about 130-140°C, TLC maximum about 220°C) in conjunction with better chemical stability, and these glasses contained less P_2O_5 (Fig. 1, Table 1).

TABLE 1. Glass Compositions

Glass grade	Synthesis composition, mass %					Thermoluminescence intensity, rel. units
	$MgO \cdot P_2O_5$	$Na_2O \cdot P_2O_5$	$Al_2O_3 \cdot 3P_2O_5$	$Al_2O_3 \cdot P_2O_5$	MnO_2	
ÉD	87	—	13	—	0,1	1,0
9	—	75	25	—	0,1	0,6
10	—	75	12,5	12,5	0,1	1,1
11	—	77	—	23	0,1	1,0
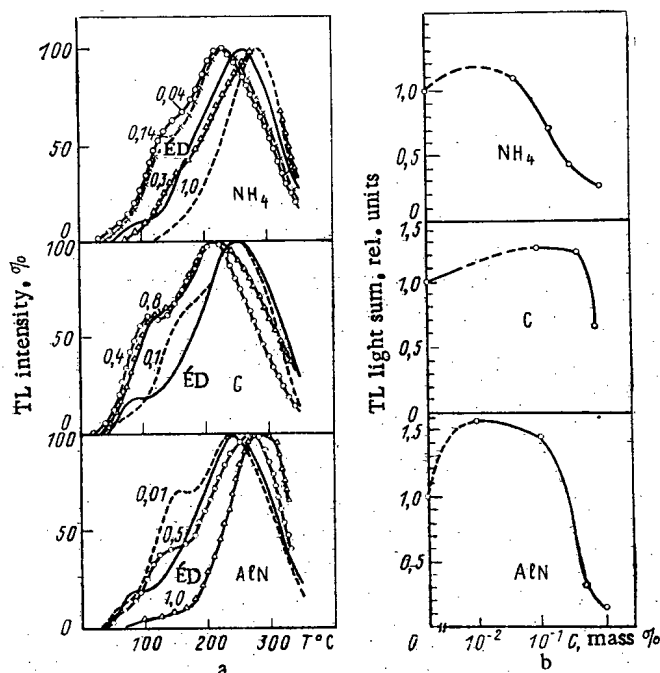
Fig. 2. Effects of NH_4, C, and AlN on the form of the TLC (a) and on the total TL light sum (b).

Figure 1 shows that the TLC for the best of these compositions are far from the required TLC. To bring the TLC close to the required one, we examined the effects of various dopes on the TLC shape. The dopes were the following elements and groups (in parentheses we give the concentration ranges in mass %): Ti, Cr, Co, Ni, Pb $(10^{-4}-10^{-2})$; Fe $(10^{-4}-1.8\cdot10^{-1})$; Cu $(10^{-4}-5\cdot10^{-2})$; Ce (10^{-2}); Cl $(6.6\cdot10^{-2}-1.65\cdot10^{-1})$; As $(7.6\cdot10^{-2}-1.9\cdot10^{-1})$; C $(10^{-1}-10)$; NH_4 $(4.3\cdot10^{-2}-1.0)$; SO_4 $(7\cdot10^{-2}-2.6)$; AlN $(10^{-2}-1.0)$. The thermoluminescence (TL) of the glasses was only quenched to various extents by Fe, Co, Ni, Cu, Pb, Ti, Cr, Cl, and As [4]. Throughout the concentration range, all the dopes apart from Cu had no effect on the shape of the TLC. Cu appreciably altered the shape of the TLC and weakened the emission in the high-temperature region. This reduced the half width of the peak by about $30°C$ at a concentration of $10^{-2}\%$. Any further increase in Cu content greatly reduced the TL intensity, which is undesirable.

The effects of NH_4, C, and AlN on the thermoluminescence deserve attention. Figure 2a compares the TLC shapes, while Fig. 2b shows how the stored light sum varies with the dope concentration. The quenching actions of NH_4, AlN, and C occur at much higher concentrations (>0.1%) than in the case of the coloring elements (Fe, Co, Ni, etc.), while at low levels of these dopes the stored light sum increases. The NH_4, AlN, and C alter the level of the redox potential in the molten glass toward reducing conditions, which leads to an increase in the stored light sum and a shift in the TLC toward lower temperatures. The stored light sum increases particularly when an aluminum nitride is used, while carbon produces the most effective shift to lower temperatures. The reducing agent tends to break the valency bonds (removes oxygen), which alters the structure of the glass; there is an increase in the number of structures responsible for trapping levels of intermediate depth (in the range 80–180°C). The largest shift in the TLC toward lower temperatures occurs at 0.4% carbon.

The effects of the dopes on the curve shape were examined for glasses in the $MgO-Al_2O_3-P_2O_5$ system; in the $Na_2O-Al_2O_3-P_2O_5$ system, carbon and copper have the same effect on the glass as in the $MgO-Al_2O_3-P_2O_5$ one, but with one exception: The introduction of carbon into a glass in the soda system reduces the intensity. We examined the concentration range from 10^{-1} to 2.5 mass %. The carbon substantially shifted the TLC toward lower temperatures relative to the initial glass of composition 11 (by 40°C at the peak and by 70–75°C at half height). As the carbon content increased, the intensity in the first peak at 90–100°C decreased, which may be considered as a positive factor, but at a carbon content of over 0.8% the glass becomes turbid, which prevents its practical use.

On the basis of the above, ÉD-1 glass may be recommended for a detector in the effective-dose device: $MgO\cdot P_2O_5$ (87 mass %), $Al_2O_3\cdot3P_2O_5$ (13 mass %), MnO_2 (0.1 mass %), C (0.4 mass %), CuO (0.0125 mass %) [5].

677
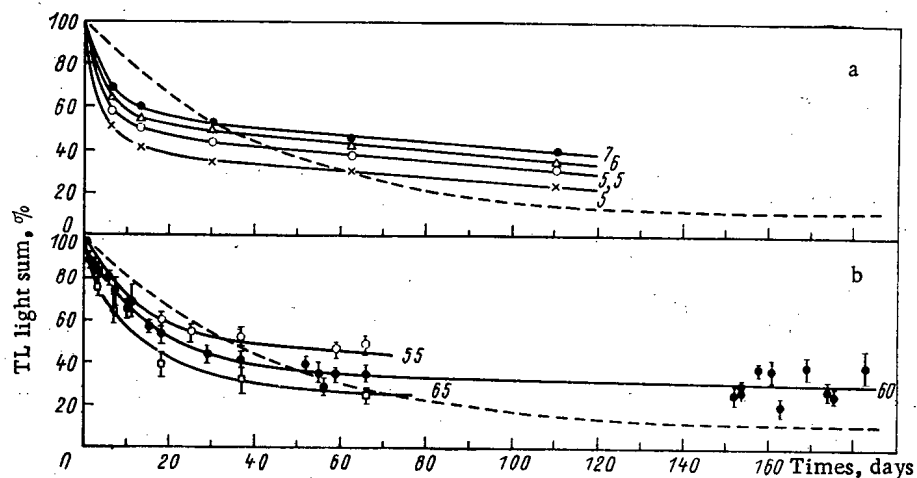
Fig. 3. Dependence of readings of ÉD-1 dosimeter on storage
time after irradiation on using a heating element with a con-
stant temperature of 360°C (a) and on heating from room tem-
perature at a rate of 5 deg·sec^{-1} (b); the numbers on the
curves are the times, sec, from the start of heating to the
middle of the measurement interval with $\Delta t = 1$ sec; dashed
lines indicate variation in effective dose given by the Blair—
Davidson theory.

This extensive study of aluminophosphate glass compositions has enabled us to bring the
basic characteristic (the TLC) close to the required one. It will probably be difficult to
produce any further improvement in this characteristic in the aluminophosphate glass system.
Phosphate glasses have deep carrier trapping levels. It is impossible to avoid these deeper
trapping levels by the method of modifying the TLC and displacing it toward lower temperatures,
and the role of them can only be diminished by selecting the basic composition of the glass,
quenching the high-temperature part of the TLC, and altering the structure of the phosphate
chains by influencing the redox potential. It would seem that other thermoluminescent sys-
tems are required to produce any further improvement in the dosimeter characteristics.

A basic characteristic of the detector is the dependence of the readings on storage time
after irradiation. Figure 1 shows that the detector should have a TLC in which the main peak
lies at 80-180°C. Consequently, the readings of such a detector will be substantially depen-
dent on the environmental temperature. To minimize the variability in the readings as af-
fected by temperature, it is desirable to place the dosimeter at the surface of the body un-
der clothing (e.g., around the neck on a cord), since the surface of the human body is a form
of thermostat. The temperature of the body surface at the chest under clothing under normal
conditions is 33-34°C with fluctuations of about 1-3°C when the environmental temperature
varies in the range from —10 to +45°C. On this basis, the time dependence of the readings was
determined by keeping the dosimeter after irradiation in a thermostat at 33-34°C.

The half width of the TLC fo ÉD-1 glass is several times larger than the calculated TLC
(Fig. 1), and the presence of much of the light sum in the temperature range up to about 100°C
results in an impermissibly large error in determining the effective dose during the initial
period of use (about 50%) on recording the total TL light sum. Consequently, one can improve
the dependence of the readings on storage time only by selecting the measurement conditions,
particularly by recording not all the light sum, but only part of it.

We used two modes of heating for the glass detector:

1) the detector was placed on a heating element with a constant temperature (about 360°C),
and the detector was then heated at a high but variable rate (about 40 deg·sec^{-1});

2) the detector was placed on the heating element at room temperature and then was heated
at an approximately constant rate of 5 deg· sec^{-1}.

To choose the optimum measurement conditions one needs a part of the TLC in which the
change of the light sum with time after irradiation reproduces the dependence of the effec-
tive dose on time given by the Blair—Davidson theory (broken line in Fig. 3).

678

TABLE 2. Calculated Results on Effective
Dose and Errors of Determination

Form	Periods of proposed dosimeter use	D_{ef}, rad	D, rad	D_{ED}, rad	δ_{ED}, rad	δ, %
I	20.08.57—19.11.57	42,1	127,3	46,0	+9,2	+202
II	01.07.58—30.07.59	143,8	297,8	135,6	—5,7	+107
III	01.05.59—30.07.59	989,5	1561	816,5	—17,5	+58
IV	01.09.60—30.11.60	452,9	608,5	347,9	—23,2	+34
V	17.10.69—16.01.70	81,0	262,0	94,4	+16,3	+224

*1 rad = 0.01 Gy.

A batch of ÉD-1 detectors was given a dose of 20 rad (1 rad = 0.01 Gy) of γ rays from a ^{60}Co source. These dosimeters were stored in a thermostat at 33 ± 1°C and their TLC were measured at various times up to 190 days. These TLC were used in determining the light sum per sec at various times after the start of heating. Figure 3 shows the results from the above two measurement conditions.

There is an additional error in determining the effective dose because of the difference between the decay curve for the ÉD-1 readings and the time dependence of the effective dose, which is defined by

$$\delta = \frac{I(t)/I(0) - D_{ef}(t)/D_{ef}(0)}{D_{ef}(t)/D_{ef}(0)} \cdot 100\%,$$

where $D_{ef}(t)$ is the effective dose at time t after brief irradiation, and I(t) is the reading of the dosimeter at time t.

The minimal errors with the maximum period of use are obtained under the following recording conditions: on heating at the uneven rate by recording the light sum at 5.5 sec after the start of heating, or on heating at 5 deg·sec^{-1} by recording the light sum at 60 sec after the start of heating. In both cases one records the light sum for 1 sec. Experience showed that recording only a small part of the light sum has virtually no effect on the spread in the readings.

The additional errors were calculated for two extreme cases; single irradiation at the start of the period of **dosimeter** wearing, which represents the maximum error, and uniform irradiation throughout the period of use (Fig. 4). Curves 1–3 were obtained with the following parameters in the Blair—Davidson formula: f = 0.1 and β = 0.024 day^{-1}, while curves 4, 5 were obtained with f = 0.15 and β = 0.022 day^{-1}. In [6], it is considered that the latter values of f and β are better, because they are averages over the range of possible values.

When rapid operational dose determination is required, it is desirable to use the first mode of measurement (5.5 sec from the start of heating). Figure 4 then shows that the ÉD-1 dosimeter enables one to measure the effective dose over any time interval in a period of two months of dosimeter use with an additional error not exceeding ±30%. If there is fractionated irradiation, the same error applies for a dosimeter-use period increased to 70–80 days. When on the other hand, the speed in obtaining the results is not decisive, e.g., under conditions of space flights, one can use the second mode of measurement (60 sec from the start of heating). Then the maximum additional error in determining the effective dose is reduced to ±23% for a working time up to 70 days, while with uniform irradiation the error does not exceed ±20% over 140 days.

As an illustration of how irradiation fractionation reduces the error, we consider the hypothetical case where the ÉD-1 dosimeter is used (D_{ED}) to record the effective radiation dose from solar flares actually observed in 1957–1969 (Table 2). The period of dosimeter use was taken as three months, and the effective dose was calculated by means of f = 0.15 and β = 0.022 day^{-1}. Figure 5 shows the distribution of the tissue **dose** due to solar flares during the period of dosimeter use.
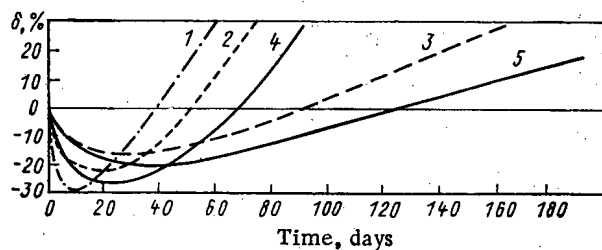
Fig. 4
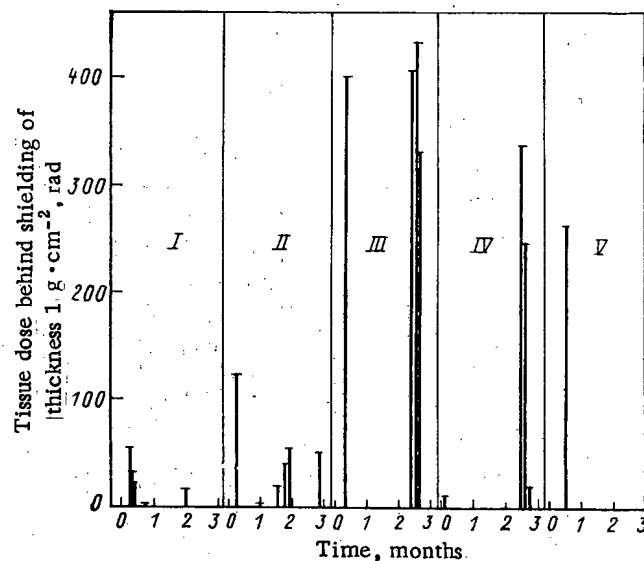
Fig. 5

Fig. 4. Additional error in determining the effective dose on single irradiation (1, 2, 4) and on uniform irradiation (3, 5) for various ways of heating the detector: 1) heating element at a constant temperature of 360°C; 2-5) heating from room temperature at a rate of 5 deg·sec⁻¹.

Fig. 5. Time distribution of the tissue dose due to solar flares (Table 2).

Table 2 shows, firstly, that the effective doses D_{ef} and D'_{ED} are less by factors of 2-3 than the overall dose D for the same time and, secondly, that the ED-1 dosimeter enables one to determine the effective dose with an error δ'_{ED} that is acceptable in practice. The error δ in determining the effective dose with a total-dose meter substantially exceeds δ'_{ED}. The total-dose meter does not allow one to consider the actual dose distribution in time, and therefore this traditional dosimeter is unsuitable for determining the hazard on prolonged irradiation to high doses.

As shown by experience, ED-1 glass is reasonably efficiently manufactured. The spread in sensitivity from a single batch of glass is not more than ±10%, while there is good reproducibility in the glass parameters from batch to batch.

The readings given by ED-1 glass dosimeters are linear from 1 to 5000 rad of γ rays from ^{60}Co. The Z_{ef} for the photoelectric effect is 11.8 for the glass of this composition, as for IKS dosimeters, and therefore the energy dependence of the sensitivity is the same as for the IKS [4]. Consequently, the energy dependence of the sensitivity of the effective-dose device in an IKS dosimeter cassette will not exceed ±20% over a photon energy range from 60 keV to 6 MeV.

This detector has all the necessary dosimetric characteristics for use in an individual effective-dose device, whose desirability is obvious, since the use of computational methods or direct-indicating instruments in determining effective dose does not enable one to incorporate the actual irradiation conditions: time spent in the irradiation field, screening by surrounding objects, movement relative to the radiation sources, etc.

LITERATURE CITED

1. H. O. Davidson, Biological Effects of Whole-Body Gamma Radiation on Human Beings [Russian translation], Atomizdat, Moscow (1960).
2. I. G. Akoev, Problems in Post-Irradiation Recovery [in Russian], Atomizdat, Moscow (1970).
3. Z. Spurny and Z. Novotny, in: Proc. Third Int. Conf. on Luminescence Dosimetry (1971).
4. I. A. Bochvar et al., The IKS Dosimetry Method [in Russian], Atomizdat, Moscow (1977).
5. I. A. Bochvar et al., "Radiothermoluminescent glass for an individual dosimeter detector," Inventor's Certificate No. 586634, February 25 (1977).
6. E. E. Kovalev, V. I. Popov, and V. A. Sakovich, Kosm. Biol. Meditsina, 3, No. 4, 29 (1969).

STRUCTURE OF THE ARTIFICIAL RADIONUCLIDE CONCENTRATION PATTERNS IN
THE BALTIC AND THE NORTH SEA IN THE SPRING OF 1981

D. B. Styro, G. I. Kadzhene,
I. V. Kleiza, and M. V. Lukinskene

The radiation background in the Baltic and North seas due to man-made radionuclides until recently has been due to global fallout [1-4], the only exception being represented by ^{137}Cs, which enters the North Sea with wastes from the nuclear industry [5, 6].

Recently, there has been a reduction in the ^{137}Cs concentration in the Baltic [2], with the retention of fairly high values in the North Sea [6]. However, the ^{90}Sr and ^{144}Ce levels in the Baltic somewhat exceed the absolute levels in the North Sea, which is evidently due to the relative closure of the Baltic, the considerable effect from land runoff, which brings in additional ^{90}Sr, and the smaller volume of the water.

Naturally, there are deviations from the average concentrations at individual points in the seas, because of storms and water-mass migration, as well as water exchange between these seas, the entry of fresh products from nuclear explosions, etc. However, the mean concentrations or the overall contents vary comparatively slowly and fluctuate much less widely than the values at individual points.

The ^{137}Cs, ^{90}Sr, and ^{144}Ce concentrations were measured in the surface waters of the Baltic and at a depth of 50 m, and also in the surface waters of the North Sea, during April-May, 1981 during a voyage of the Lev Titov ship (Table 1). The radionuclide concentrations were determined by radiochemical methods [7, 8]. The maximum possible errors in determining the ^{137}Cs and ^{144}Ce concentrations were 25%, as against 15% for ^{90}Sr.

Table 1 shows that the highest ^{137}Cs levels occur in the surface waters of the North Sea, where the entry of ^{137}Cs from industrial sources substantially exceeds the background due to global fallout. However, the ^{90}Sr and ^{144}Ce concentrations are lower here than in the surface waters of the Baltic. In particular, there is a comparatively high ^{144}Ce concentration around Gotland Island (Fig. 1, points 3, 4, 5, 7). If we eliminate these observations, the average ^{144}Ce concentration in the surface waters of the Baltic is 11 Bq/m^3.

The natural vertical distribution of the radionuclide concentrations is such that the levels decrease gradually as the depth increases, which applies, in particular, to ^{90}Sr and ^{144}Ce in the Baltic (Table 1). The average ^{137}Cs concentration in the Baltic has an anomalous vertical course, which occurs because the denser North Sea water containing ^{137}Cs enters the Baltic and displaces the less dense water from the bottom layers, thereby raising the ^{137}Cs concentration there. The radionuclide concentrations at the individual points often deviate considerably from the mean values (Table 2). The largest fluctuations in ^{137}Cs concentra-

TABLE 1. Average Concentrations of Man-Made Radionuclides, Bq/m^3

Depth, m	Baltic Sea			North Sea		
	^{137}Cs	^{90}Sr	^{144}Ce	^{137}Cs	^{90}Sr	^{144}Ce
0	15	29	16	106	23	11
50	18	24	11	—	—	—

TABLE 2. Maximal and Minimal Values of Radionuclide Concentrations Recorded in April–May, 1981 in the Baltic and North Seas, Bq/m^3

Depth, mm	Baltic Sea			North Sea		
	^{137}Cs	^{90}Sr	^{144}Ce	^{137}Cs	^{90}Sr	^{144}Ce
0	21 (8,12) *	46 (8)	47 (5)	185 (21)	28 (21, 26)	31 (25)
	8 (9)	10 (6)	4 (15)	24 (24)	16 (24)	4 (17, 23)
50	27 (9)	33 (7)	30 (4)	—	—	—
	10 (4)	20 (9)	7 (9)	—	—	—

*The numbers in parentheses are those of the sampling points (see Fig. 1).
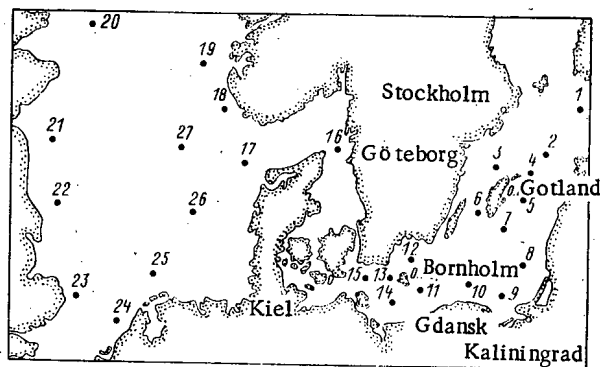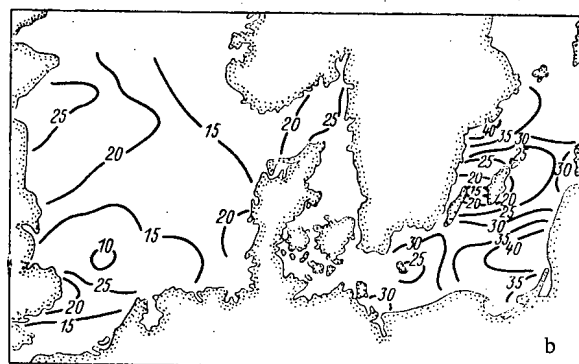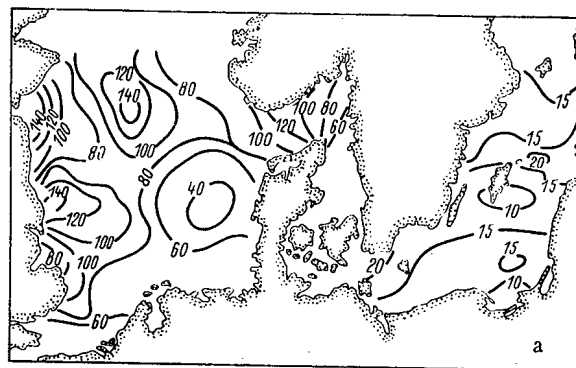
Fig. 1

Fig. 2

Fig. 1. Water sampling points in the Baltic and North seas.

Fig. 2. Concentration fields (Bq/m^3) for ^{137}Cs (a) and ^{90}Sr (b) in the surface waters of the Baltic and North Seas in April–May, 1981.

tion occur in the surface waters of the North Sea, while those in ^{90}Sr and ^{144}Ce occur in the surface waters of the Baltic. However, the data only allow one to estimate the contents of radionuclides in individual regions of the Baltic and North seas. A more detailed study was made of the structure of the concentration fields in these bodies of water by calculation (objective analysis [9–11]) from the experimental data. The calculations were based on stability in the hydrological processes during the measurements. The radionuclide concentrations were determined at the nodes of a regular net with a step of half a degree. The calculations were performed with a BÉSM–6 computer.

Figure 2 shows the calculations on the ^{137}Cs and ^{90}Sr concentrations for the surface waters of the Baltic and North seas. There are considerable differences in the absolute values of the ^{137}Cs concentrations in these areas (Fig. 2a). There is a gradual reduction in concentration from the coast of Britain in an easterly direction. The elevated ^{137}Cs concentrations at the east coast of Britain are due to discharges of the nuclear wastes into the Irish Sea, which are brought into the North Sea by the North Atlantic current [5, 6].

The lowest ^{137}Cs concentration occurs in the southeastern part of the North Sea. There is a certain rise in concentration on entry to the Skagerrak Straits, in which the values decrease to 20 Bq/m^3 in the southern part of the Baltic. This indicates that the North Sea influences the radioactive pollution of the Baltic. The structure of the ^{137}Cs concentration field in the Baltic is comparatively homogeneous. The lowest values occur in the southeastern and central parts (Fig. 2a).

The concentration patterns for ^{90}Sr in the Baltic and North seas are quite different in structure and absolute values (Fig. 2b). The most homogeneous structure for the ^{90}Sr concentration pattern occurs in the North Sea, where the absolute values are much lower than those in the Baltic. The lowest ^{90}Sr concentrations occur in the southwestern part of the North Sea, with the highest ones in the northwestern part (Fig. 2b). A rise in ^{90}Sr concentration is observed in the region of the Skagerrak. In the Baltic, the highest ^{90}Sr concentrations occur in the southeastern and northwestern parts, while the lowest levels occur in the regions of Götland and Bornholm islands (Fig. 2b). The comparatively scanty information does not enable us to calculate the structure of the ^{144}Ce field.

682

This structure in the radionuclide concentration fields in the Baltic and North seas is due, on the one hand, to the effects of precipitation and nuclear installations and, on the other, to the hydrological features of these bodies of water.

LITERATURE CITED

1. D. B. Styro, in: Pollutant Distribution in the Environment [in Russian], Mokslas, Vilnius (1980), p. 121.
2. D. B. Styro et al., At. Energ., 51, No. 2, 116 (1981).
3. D. B. Styro and I. V. Kleiza, Okeanologiya, 21, No. 3, 464 (1981).
4. D. B. Styro et al., in: Chemical and Radioactive Components of the Atmosphere and Hydrosphere [in Russian], Mokslas, Vilnius (1978), p. 138.
5. H. Kautsky, Deutsche Hydrographische Zeitschrift, No. 6, 241 (1973).
6. H. Kautsky, ibid., No. 7, 217 (1977).
7. L. M. Ivanova, Radiokhimiya, 9, No. 5, 622 (1967).
8. Yu. Ya. Mikhailov, Methods of Determining Strontium 90, Cesium 137, Cerium 144, and Lead 210 in Specimens of Plant Origin [in Russian], Ministry of Agriculture in the USSR, Principal Veterinary Board, Institute of Experimental Veterinary Practice, Moscow (1980).
9. I. V. Kleiza and D. B. Styro, in: Radioactive Tracers in Research on the Atmosphere and Hydrosphere [in Russian], Mokslas, Vilnius (1979), p. 167.
10. D. B. Styro and I. V. Kleiza, [1], p. 148.
11. D. B. Styro and I. V. Kleiza, in: Problems in Researching Atmospheric Pollutants [in Russian], Mokslas, Vilnius (1981), p. 119.

LETTERS TO THE EDITOR

AUTOMATED SYSTEM FOR CARRYING OUT OVERPOWER LOOP TESTS IN VVR-SM REACTORS

T. B. Ashrapov, L. I. Burmagin, A. K. Korennoi,
P. P. Oleinikov, O. P. Russkov, T. B. Satybaldiev,
Yu. A. Tokarev, and É. M. Chizhova

Reactor overpower tests are of considerable value to the designers of a new nuclear plant, providing them with experimental data on the behavior and serviceability of models under real conditions. A large number of operational calculations have to be carried out when the reactor is brought up to its rated load and to its margin above rated load, and also when the reactor is being shut down. These include physical calculations that enable the operator to control the course of the experiment. In order to carry out such calculations, we need both operational data on the state of the reactor and its coolant loop and also statistical data on the state of the reactor in the various periods of the test. This involves recording a large number of parameters and their subsequent processing. Demands such as these made it essential to use data-processing centers equipped with computers having sophisticated data I/O and storage facilities with a specially designed program set.

The present article examines an automated system ("Resurs" system) for research into overpower loop tests on the channels of the VVR-SM reactor, developed in the Institute of Nuclear Physics, Academy of Sciences of the Uzbek SSR. Apparatus is proposed, together with a schematic (see Fig. 1) for the test program. A channel in the center of the reactor core forms the subject of the investigation. This is furnished with a vacuum line, gas and power supplies, a standardizing converter and amplifiers for the measurement signals, a control desk with built-in mimic diagram and control instruments, a control computer type M-6000, and a measurement system.

The M-6000 computer incorporates a high-speed printer—plotter type Videoton-343, **three** Videoton-340 VDUs, and three Izot-1370 disk memories. A modified version of an RTE-2 real-time disk memory organizes the computer operations. This ensures that the disk is run in the best possible manner for multiterminal access. Up to 32 VDUs can be operated by the computer. A set of programs has been developed, enabling the computer and disk system to operate in a data-processing and advisory role. The program set consists of sixty 200 kbyte complexes, including ten programs for calculating the indirect parameters of the channel.

The tests monitor 128 parameters, including temperature (t), current (I), voltage (U), neutron-flux density (φ), and gas pressure (p), while carrying out the following functions: acquisition, primary processing, and storage of **data**, representing information in digital and analog form at the control panel; checking the reliability of measurements and the deviation from settings; mathematical processing **and recording the results by the printer; organizing the** storage and real-time processing of data files in the data bank; monitoring and recording of anomalous events at increased request speed; organizing the acquisition and representation of data under the control of the operator; documenting the results of the tests; and backing up the measurements of the principal parameters by means of a measurement system capable of feeding the data manually into the computer (to refresh the data base).

The model envisages three conditions of operation for monitoring the functioning of the reactor channel: normal, **prefault, and fault.** The monitoring mode is changed automatically when the reactor operates in an abnormal fashion. The cycle of request and primary processing of the data from the 128 measurement channels, comprising a tenfold request on each channel, averaging, and comparing the results with the settings, takes 15 sec for the normal conditions of operation of the reactor. Under anomalous conditions of operation, the request cycle is reduced to 5 sec, while the display units receive signals representing the characteristics of the fault values of the parameters.

The program set covers ten stages of functioning of the tests in accordance with the test program, including preparatory operations, a **step**-by-step approach to the required con-
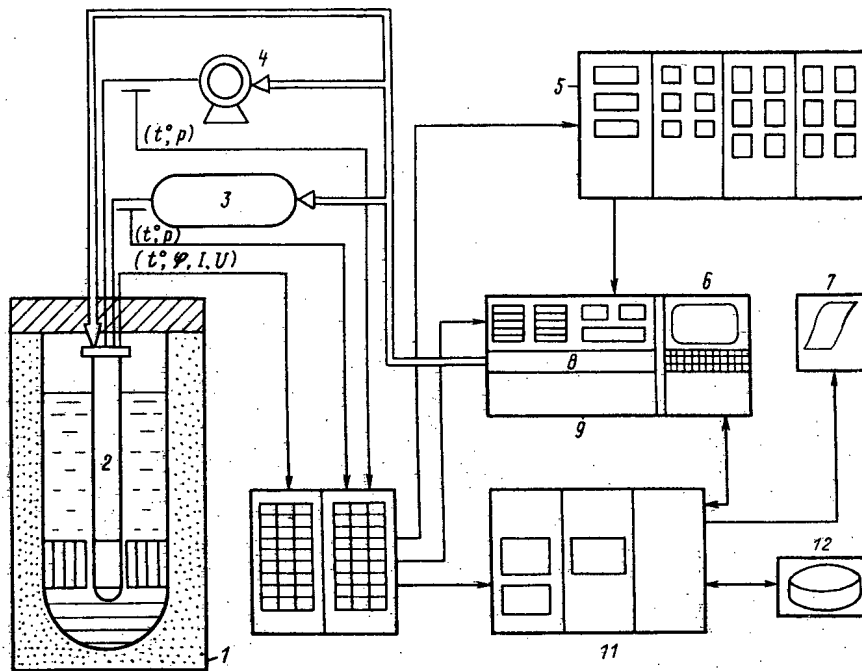
Fig. 1. Flow chart of "Resurs" experimental system: 1) reactor; 2) channel; 3) gas system; 4) vacuum system; 5) measurement system; 6) VDU; 7) printer-plotter; 8) mimic diagram; 9) control board; 10) measurement converter; 11) M-6000 computer; 12) data bank.

ditions of operation, and the conclusion of the test. The experimental system is adjusted automatically under all conditions at the command of the operator in not more than 10 sec.

The vector state of the reactor channel is formed at each stage of the investigation during primary processing. This state incorporates six variables, which are analyzed for reliability by comparing them with the initial vector and the vector representing the previous measurements. The results are then entered in the data bank. The data bank is run by a separate disk memory with limited access. The organization of the data bank enables data to be accumulated over the test cycles (more than 5000 h) with a facility for operator access on the basis of various criteria. The data are represented in the form of a table drawn up by the fast printer or the operator's VDU. The program set offers the operator a wide range of ways in which the data can be represented and in which the investigation system can operate. The dialog program is made up of 20 instructions enabling the operator to control the progress of the tests.

A wide variety of modes of access, storage, and representation of the test data under the control of the operator is a feature of this system. The system enables the quality of the information obtained during the tests to be **improved** and the ability of the operator to control the investigations of models of new nuclear systems to be increased [2]. The results of the present work are recommended as providing a basis for the planning of computerized systems of chemical, engineering, and physical investigation, and for the design of test rigs and test plants in various fields of the national economy, where real-time acquisition and processing of data files are required.

LITERATURE CITED

1. S. A. Barinov et al., Vopr. At. Nauki Tekh., Ser. Yad. Priborostr., No. 2-3 (43-44), 17-23 (1980).
2. I. S. Krasheninnikov and V. V. Matveev, At. Energ., 50, No. 2, 110 (1981).

DOSE BUILDUP FACTORS OF COLLIMATED GAMMA RADIATION BEHIND STEEL AND ALUMINUM PLATES

M. B. Vasil'ev and N. F. Chuvashev
UDC 539.1.09

Collimated γ radiation is frequently used in nondestructive testing and in radiotherapy. The buildup factors of collimated radiation behind shields of the most commonly used materials, steel and aluminum, have still not been adequately studied.

We have directed collimated radiation from isotropic ^{137}Cs and ^{60}Co sources into steel and aluminum plates. The angles of collimation were 0, 15, 30, 45, and 90°. Lead collimators 14.8 cm long and 9 cm in diameter were located inside the lead shield of the basic BDBSÉ-1eM detection block. The radiation was recorded by an SBM-10 miniature counter with filters to flatten its sensitivity to radiation of various energies [1, 2]. The steel and aluminum plates extended far enough in the direction perpendicular to the direction of propagation of the γ radiation to ensure an infinite medium [3]. The plates were up to six mean free paths (mfp) thick. A schematic diagram of the experiment is shown in Fig. 1.

Tables 1 and 2 list the experimental dose buildup factors of collimated γ radiation in shield geometry for steel and aluminum plates; the errors do not exceed 11%. These tables include for comparison, the energy buildup factors of collimated γ radiation calculated for similar points from separate data in [4, 5]. There are no similar data in the literature for dose buildup factors. Energy buildup factors are always somewhat smaller than dose buildup factors. Comparison shows that the measured dose buildup factors are close to the calculated energy buildup factors, and should be close to calculated dose buildup factors.

TABLE 1. Dose Buildup Factors of Collimated γ Radiation behind a Shield of Aluminum Plates

θ	Thickness of Al plate, mfp (μr)	$E_0 = 0{,}661$ MeV		$E_0 = 1{,}25$ MeV	
		results of our experiment	calculated from data in [4, 5]	results of our experiment	calculated from data in [4, 5]
0°	1	1,10	—	1,06	—
	2	1,21	—	1,15	—
	3	1,34	—	1,21	—
	4	1,45	—	1,36	—
	5	1,55	—	1,48	—
	6	1,60	—	1,56	—
15°	1	1,20	1,17	1,18	1,15
	2	1,45	1,39	1,37	1,31
	3	1,68	—	1,54	—
	4	1,80	1,74	1,72	1,76
	5	2,14	—	1,90	—
	6	2,45	—	2,04	—
30°	1	1,33	—	1,28	—
	2	1,96	1,83	1,82	1,68
	3	3,07	—	2,90	—
	4	4,0	—	3,85	—
	5	5,12	—	4,90	—
	6	6,17	—	5,95	—
45°	1	1,50	—	1,40	—
	2	2,20	—	2,13	—
	3	3,46	—	3,30	—
	4	4,38	4,29	4,22	—
	5	5,40	—	5,20	—
	6	7,0	—	6,75	—
90°	1	1,69	—	1,55	—
	2	2,48	—	2,35	—
	3	3,53	—	3,40	—
	4	4,77	4,30	4,62	—
	5	5,92	—	5,75	—
	6	7,30	—	6,80	—

TABLE 2. Dose Buildup Factors of Collimated γ Radiation behind a Shield of Steel Plates.

θ	Thickness of steel plates, mfp (μr)	$E_0 = 0{,}661$ MeV		$E_0 = 1{,}25$ MeV	
		results of our experiment	calculated from data in [4, 5]	results of our experiment	calculated from data in [4, 5]
0°	1	1,08	—	1,05	—
	2	1,12	—	1,07	—
	3	1,18	—	1,13	—
	4	1,24	—	1,22	—
	5	1,35	—	1,29	—
	6	1,40	—	1,36	—
15°	1	1,11	1,07	1,07	1,06
	2	1,26	1,18	1,22	1,16
	3	1,44	—	1,39	—
	4	1,53	1,45	1,46	1,35
	5	1,70	—	1,55	—
	6	1,93	—	1,80	—
30°	1	1,20	1,16	1,14	1,14
	2	1,75	—	1,52	—
	3	2,34	—	2,20	—
	4	3,0	—	2,78	—
	5	3,75	—	3,55	—
	6	4,65	—	4,20	—
45°	1	1,37	—	1,22	—
	2	1,86	—	1,68	—
	3	2,50	—	2,36	—
	4	3,25	—	3,08	—
	5	4,18	—	3,96	—
	6	5,0	—	4,52	—
90°	1	1,44	1,23	1,36	1,15
	2	2,20	—	1,95	—
	3	3,0	—	2,70	—
	4	3,93	—	3,75	—
	5	5,20	—	4,20	—
	6	5,60	—	4,73	—

Fig. 1. Schematic diagram of positions of: 1) source; 2) collimator; 3) metal plates; 4) detector. The graphs show buildup factors B as a function of θ behind a shield of metal plates; $\bullet$, $\circ$) ^{137}Cs and ^{60}Co for Al; $\blacktriangle$, $\triangle$) ^{137}Cs and ^{60}Co for Fe.

Figure 1 also shows the dependence of the buildup factors of $E_0 = 0.661$ MeV γ radiation behind shields of steel and aluminum plates 6 mfp thick as a function of the angle of collimation. The buildup factors are increased substantially when the angle of collimation is increased to 45°. From 45 to 90° the increase in the buildup factors is trivial for both $E_0 = 0.661$ and 1.25 MeV. For angles of collimation from 45 to 90° and a small number of mfp, more radiation is preferentially scattered forward and therefore does not reach the detector. In addition, at a certain distance from the source the angle of scattering to the detector increases, the cosine of this angle decreases, and the probability of photoabsorption increases, since the distance from the scattering center to the detector is increased. All this causes a very small increase in the buildup factors for angles of collimation $\theta = 45$-90°.

LITERATURE CITED

1. A. M. Panchenko, At. Energ., 14, No. 4, 408 (1963).
2. V. P. Mashkovich and V. A. Klimanov, At. Energ., 20, No. 2, 127 (1966).
3. V. I. Kukhtevich, B. P. Shemetenko, and B. I. Sinitsyn, At. Energ., 8, No. 1, 66 (1960).
4. R. L. Kimel' and V. P. Mashkovich, Shielding Against Ionizing Radiation [in Russian], Handbook, Atomizdat, Moscow (1972).
5. V. G. Zolotukhin et al., Radiation Field of a Point Monodirectional Gamma Source [in Russian], Atomizdat, Moscow (1974).

NEUTRON-ACTIVATION DETERMINATION OF GOLD IN ORES IN AN AUTOMATED VERSION

F. B. Bakhrieva, A. A. Kist, I. A. Miranskii,   UDC 543.53
A. G. Morozov, A. I. Muminov, and D. D. Pulatov

Since 1974 the Institute of Nuclear Physics, Academy of Sciences of the Uzbek SSR, has employed the neutron-activation method used in geological prospecting to determine gold in ores with automated irradiation in a nuclear reactor and measurement in a scintillation spectrometer [1, 2].

The transition to semiconductor spectrometry made it possible to build a completely automated analyzing system and to improve some parameters of the method. In measurements on a semiconductor spectrometer (Fig. 1) [Ge(Li) detector with a volume of 50 cm^3, resolution of 3.5 keV with respect to the ^{60}Co line, E_γ = 1332.5 keV] with a multichannel analyzer, the limit of gold determination attained (0.01–0.02 g/ton) was roughly an order of magnitude lower than in the scintillation variant with an rms error of ~30% (the threshold signal/background ratio for the 412-keV analytical line being 0.05). The influence of some noise (e.g., ^{179}Yb, E_γ = 395.6 keV), which is appreciable for ores from some deposits, has been eliminated.

The holding after irradiation has been reduced from 9–11 days to 7 days. This makes it possible to carry out mass analyses with a technological cycle (the time between the irradiation and the measurement of a batch of specimens) of one week and to do without sliding charts. With a five-day work week this in principle makes it possible, in comparison with the scintillation variant, to double the number of specimens irradiated per day, with allowance for the limited capacity of the specimen holder in the existing automated equipment [3, 4].

The method of mass analyses of ores for gold in the automated variant provides for the simultaneous irradiation and measurement of a specimen and a neutron monitor without separating them in the measuring position. Molybdenum proved to be the most appropriate monitor. We used the daughter radionuclide ^{99m}Tc (140.5 keV), which is formed in the transformation chain ^{98}Mo(n, γ)^{99}Mo → ^{99m}Tc. The radionuclides ^{99}Mo and ^{198}Au have similar half-lives (67 and 65 h, respectively) and their γ radiations do not display mutual influence. The monitor photopeak 140.5 keV (^{99m}Tc) can be measured with good accuracy. The contribution of the specimen to this photopeak turned out to be insignificant. The signal/background ratio for
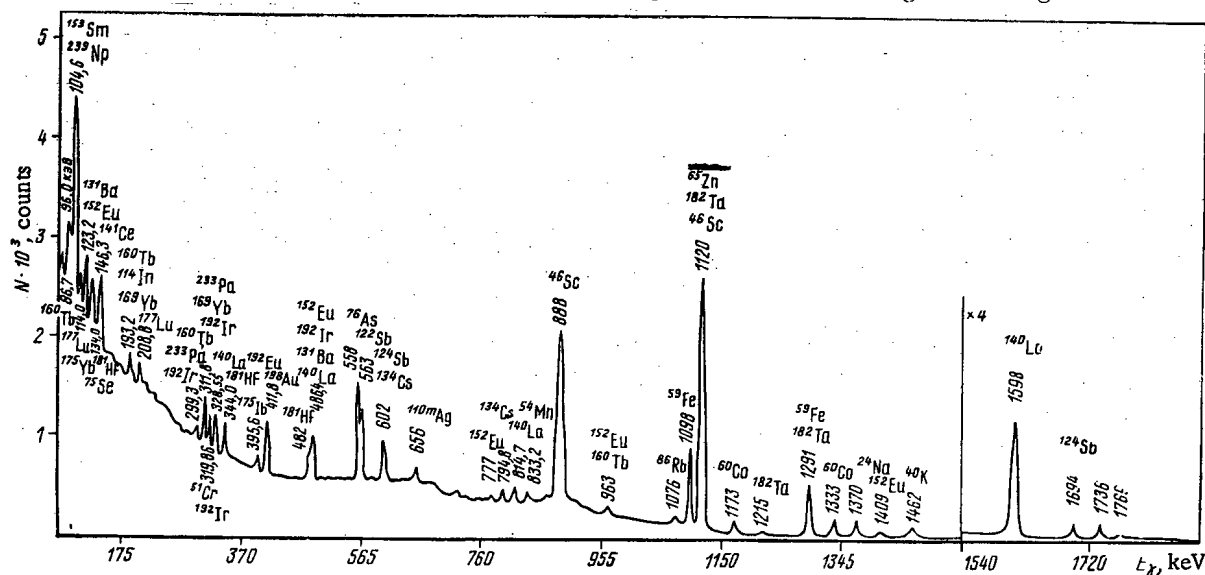
Fig. 1. Gamma-ray spectrum of irradiated specimen of gold-bearing ore after holding for 7 days.
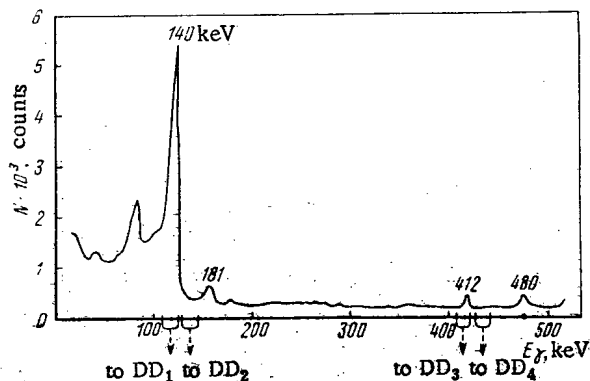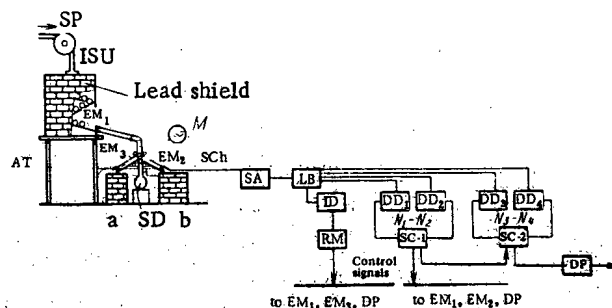
Fig. 2

Fig. 3

Fig. 2. Fragment of γ-ray spectrum of an activated specimen of gold ore with segments cut out by differential discriminators.

Fig. 3. Automated system for measurements during analysis of large ore samples for gold: ISU) intermediate storage unit; PA) preamplifier for the semiconductor detector; SA) spectrometric amplifier; LB) linear branching device; ID) integral discriminator; RM) ratemeter; DD) differential discriminator; SC) subtraction circuit; DP) digital printer; EM) electromagnet; M) electric motor; SCh) specimen changer; AT) assembly table; SP) specimen placer; SD) semiconductor detector.

the 140.5-keV line in the total spectrum of the radiation from the specimen + monitor varied roughly from 3 to 7.

At gold contents above ∼0.1 g/ton in ores, measurements were made in spectral "windows" [5], which made it possible to create systems with differential discriminators (DD) but without analyzers. The discriminators are set for the 140.5-keV and 412-keV photopeaks and additional background segments in the spectral regions ∼160-175 and ∼420-435 keV, correspondingly (Fig. 2). The width of the discriminator "windows" in the region of a photopeak is 5 keV. The width of the background segments was selected by the condition of equal pulse counts in them and in the corresponding "windows" for the matrix spectrum of the specimen.

The errors of this method of measurement were studied in an experiment on real specimens from different deposits and types of ore. For the 140.5-keV line we have juxtaposed the results of the joint and separate measurements of the specimen and the monitor. For the 412-keV line we have juxtaposed the results of measurements with DD and processing of the spectrum by well-known methods; in addition, we also measured the ratio of the count in the "windows" of the photopeak and the background for empty specimens and after the decay of ^{198}Au. In all cases the error of measurements with DD was within the limits of statistical error. The technological process of mass automated analysis takes place as follows. Ore samples weighing 170-300 g, a fractionation of 1-2 mm [6], packed in polyethylene containers (a cylinder 60 mm in diameter and ∼85 mm in height) with monitors attached to them, are irradiated with the aid of a pneumatic transport apparatus [3] in a horizontal channel of the VVR-CM nuclear reactor at a flux density of ∼10^{13} neutrons/cm^2·sec for 20 sec.

The monitor (a wafer of molybdenum with a mass of ∼1 g) was attached beneath the false lid of the container and during irradiation is at the end of the horizontal channel. The activated specimens are held in a special specimen holder which is designed to hold 3000 specimens and is located in a deep storage vault [3]. After storage for 7 days, the irradiated specimens are carried by a pneumatic transport system to an automatic measuring station (Fig. 3). This station has a shielded intermediate storage unit for 100 specimens, an electromagnetic specimen changer, a semiconductor detector, and an electronic measuring apparatus From the storage unit the specimens travel in succession to the measuring position in an electromagnetic changer in which they are rotated. From the measuring position the specimens are sorted by two channels: a) high-activity specimens into a chamber for individual examination; b) for burial (see Fig. 3). The specimens move by gravity feed along guide chutes and are fixed in the required position by a system of electromagnets. Control signals for the electromagnets are generated in the measuring unit.

The optimum measuring geometry was chosen experimentally: The specimen is positioned horizontally above the Ge(Li) detector, the axis of the specimen passes through the center

689

of the detector, and the monitor is 2 cm from its edge. The electronic measuring unit de-
signed and fabricated (see Fig. 3) has two pairs of precision DD and two subtraction circuits
(SC), at the output of which the number of photopeak pulses is 140.5 and 412 keV. During the
collection of the required number of photopeak pulses from the monitor, the measurements are
interrupted and control signals are sent to the electromagnet systems. The setup includes a
ratemeter, which emits signals for cessation of measurement and rejection of the specimen
when a given level of radiation intensity is exceeded. The number of pulses of the 412-keV
photopeak is transmitted to the digital printer (DP). The calibration is carried out so that
the number of ^{198}Au photopeak pulses corresponds to the gold content in mg/ton. (For ex-
ample, 100 recorded 412-keV photopeak pulses correspond to a gold content of 100 mg/ton.)
During the calibration a correction is also introduced for the self-screening of neutrons on
gold grains [7]. The mass of the specimen is taken into account in a special way in the elec-
tronic equipment. The measuring time is roughly 1-1.5 min. The automated complex with one
measuring apparatus can handle ∿250 analyses per working day. When radiation is recorded in
the spectral "windows" by means of this measuring apparatus, the error in the analysis of
gold ore was 20-30% at a content of 0.1-1 g/ton and ∿5-15% at a content of ∿1 g/ton or more.
At the present time, a measuring system and at a method of multiple-element analysis are be-
ing developed with a single molybdenum comparator so that a complex of elements, the radia-
tion of whose radionuclides is distinguishable on the γ-ray spectrum (Fig. 1), can be deter-
mined incidentally at the same time as the gold.

The authors thank P. K. Khabibullaev for constant attention to the work and for his
support.

LITERATURE CITED

1. I. A. Miranskii et al., Gold, NSAM Instruction No. 153-YaF [in Russian], VIMS NSAM,
   Moscow (1978).
2. E. M. Lobanov et al., in: Nuclear Geophysics [in Russian], No. 3, Tr. VINNIYaGG, Nedra,
   Moscow (1968), p. 226.
3. E. M. Lobanov et al., in: Activation Analysis in the National Economy [in Russian], Fan,
   Tashkent (1974), p. 48.
4. E. M. Lobanov et al., in: Abstracts of the Third All-Union Conference on Activation
   Analysis [in Russian], Fan, Tashkent (1972), p. 45.
5. I. A. Miranskii, F. B. Bakhrieva, and A. V. Yankovskii, in: Abstracts of Fourth Republic
   Conference of Young Physicists [in Russian], Fan, Tashkent (1978), p. 98.
6. A. V. Yankovskii et al., in: Abstracts of the Third All-Union Conference on Activation
   Analysis [in Russian], Fan, Tashkent (1972), p. 71.
7. E. M. Lobanov et al., in: Activation Analysis of Rocks and Other Objects [in Russian],
   Fan, Tashkent (1967), p. 47.

ANALYSIS OF THE RESULTS OF MEASURING THE NEUTRON FIELDS OF A REACTOR
BY THE METHOD OF MATCHED ACTIVATIONAL DETECTORS

Yu. V. Dubasov and N. N. Khramov

In comparing the irradiation conditions in experiments for the neutron-field characteristics of a reactor, it is sufficient to estimate solely the thermal and epithermal components of the neutron field. The cadmium-difference method is found to be inapplicable in conditions of uncontrollable neutron-field perturbations. Often the two-detector method is used in such conditions [1]. To estimate two components, it is sufficient, in principle, to use two detectors, but, since the rate of the activation reaction is estimated with an error (there may be gross oversights) and the error in determining the activation rate may be increased with unfavorable choice of detectors, it is desirable to use a larger number of detectors or detector components [2-4]. In the present work a statistical analysis of this approach is undertaken for the example of the results of Biryukov et al. [2].

The rate of activation reaction of a thin detector with a $1/v$ cross section in the thermal region, under irradiation by thermal and epithermal neutrons with a $1/E$ distribution, is determined by the relation [5]

$$R_i = \varphi_1 \sigma_{0i} + \varphi_2 I_i, \tag{1}$$

where σ_{0i} is the cross section of activation by thermal neutrons of the i-th nuclide, cm^2; I_i, resonance integral of the i-th nuclide, cm^2; and φ_1, φ_2, flux densities of thermal and epithermal neutrons, $cm^{-2} \cdot sec^{-1}$. If N detectors are irradiated, the least-squares method may be used to estimate the flux densities of thermal and epithermal neutrons. Then φ_1 and φ_2 are determined as follows [6, 7]:

$$\Phi = (\Sigma^T V \Sigma)^{-1} \Sigma^T V R, \tag{2}$$

where

$$\Phi^T = (\varphi_1, \varphi_2); \quad \Sigma^T = \begin{pmatrix} \sigma_{0i} \cdots \sigma_{0N} \\ I_1 \cdots I_N \end{pmatrix};$$

V is the dispersional matrix of observational errors. If it is assumed that the neutron spectrum may be described by a $1/E^n$ distribution, then the activation-reaction rate may be written in the form [3]

$$R_i = \varphi_1 \sigma_{0i} + \varphi_2 f(n). \tag{3}$$

Since Eq. (3) is nonlinear in n, an iterative procedure is used to solve a system of equations of the type in Eq. (3) [7]. No statistically significant deviation from a $1/E$ distribution is observed in the results of [2], and therefore further analysis is taken for a Fermi spectrum of epithermal neutrons. The constants given in Table 1 [8] are used in the analysis.

Estimation by the least-squares method for the neutron field components in accordance with Eq. (1) gives

TABLE 1. Parameters Used in Estimating the Neutron-Field Components

Detector	Cross section, cm^2	Resonance integral, cm^2	Half-life	Rate of activation reaction, sec^{-1}
Na	0,528	0,31	15 h	$2,29 \cdot 10^{-12}$
Cu	4,4	5,0	12,8 h	$1,41 \cdot 10^{-11}$
Au	98,8	1550	2,7 days	$5,15 \cdot 10^{-10}$
Co	37,7	75,0	5,26 yrs	$1,50 \cdot 10^{-10}$

$$\Phi = \begin{pmatrix} 3.81 \cdot 10^{12} \\ 8.88 \cdot 10^{10} \end{pmatrix}. \tag{4}$$

The diagonal elements of the covariational matrix $C = \Delta R^T V \Delta R / 2 (\Sigma^T V \Sigma)^{-1}$, where ΔR is the residue vector, are estimates of the dispersion, of dimensions $R(N \times 1)$. After substitution of the numerical values, the quadratic errors are obtained:

$$S_{\varphi_1} = 0.39 \cdot 10^{12}; \quad S_{\varphi_2} = 3.14 \cdot 10^{10}.$$

As the determinant of the dispersion matrix $(\Sigma^T V \Sigma)^{-1}$ becomes smaller — or, equivalently, the determinant of the information matrix $(\Sigma^T V \Sigma)$ becomes larger — the error in the estimate Φ is reduced. If the model in Eq. (1) gives an unsatisfactory prediction of any experimental value of the activation rate, the corresponding equation may be discarded and the estimate of the flux density obtained again. The error in predicting the rate of the activation reaction of the i-th nuclide is determined by the relation

$$S^2 = (\sigma_{0i}, I_i) C^{-1} (\sigma_{0i}, I_i). \tag{5}$$

In the present case the greatest deviation of the predicted value from the experimental result is observed for copper, but it does not exceed even twice the error of the prediction and therefore cannot be regarded as a gross mistake. The confidence ellipsoid for the selection of the F criterion at a 10% significance level is determined by the equation [9]

$$6,66 \cdot 10^{-24} y_1 + 3,06 \cdot 10^{-21} y_2 = 18,$$

where y_1, y_2 are the axes of the ellipse; the numerical coefficients are eigenvalues of the matrix C^{-1}. The confidence region is sufficiently large, since the residual dispersion is estimated with only two degrees of freedom.

There may arise a situation in which the information is limited, e.g., to the rates of activation reaction of sodium and copper. In this case the value of the determinant of the information matrix is small. Estimates in the form of Eq. (2) are meaningless, since the value of the epithermal flux is negative. Therefore, the estimates of the flux densities are taken in the form of the solution of equation of the type in Eq. (1) of the form

$$\Phi = (\Sigma^T V \Sigma + \alpha E)^{-1} \Sigma^T V R \tag{6}$$

with an appropriately chosen value of the parameter α. What is the dependence of φ_1 and φ_2 on α? When $\alpha = 0.25$, the sharp change in φ_1 stops in the same region; φ_2 changes sign. The values of the neutron flux densities with this choice of α are $\Phi^T = (3.82 \cdot 10^{12}, 8.17 \cdot 10^{10})$. The agreement of the values may be regarded as good. Note that estimation of the correct problem is preferable, since the dispersion of the estimates in Eq. (6) is always larger.

For measurements of the neutron-field characteristics, the nuclides must be chosen so as to ensure the maximum value of the determinant of the information matrix, with a specified number of nuclides, i.e., to ensure a combination of cross sections and resonance integrals such that Φ may be estimated with minimal error.

LITERATURE CITED

1. S. S. Lomakin, V. I. Petrov, and P. S. Samoilov, Radiometry of Neutrons by an Activational Method [in Russian], Atomizdat, Moscow (1975).
2. V. I. Biryukov, N. N. Khramov, and N. S. Shimanskaya, At. Energ., 28, No. 4, 357 (1970).
3. P. Lund and J. Sandberg, "Direct computation of neutron spectra from multicomponent activation detector measurements," Report TKK-F-A409, Helsinki (1980).
4. V. P. Yaryna, in: Third All-Union Conference on the Metrology of Neutron Radiation in Reactors and Accelerators. Abstracts of Proceedings [in Russian], VNIIFTRI, Moscow (1982), p. 74.
5. Neutron Fluence Measurements. Technical Report Series No. 107, IAEA, Vienna (1970).
6. V. I. Andreev et al., Elements of the Analysis and Planning of Radiochemical Experiments [in Russian], Energoizdat, Moscow (1981).
7. V. I. Mudrov and V. L. Kushko, Methods of Analyzing Measurements [in Russian], Sovet-skoe Radio, Moscow (1976).
8. Handbook on Nuclear Activation Cross Section, IAEA, Vienna (1974).
9. I. Bard, Nonlinear Estimation of Parameters [in Russian], Statistika, Moscow (1976).

COMBINED USE OF DELAYED NEUTRONS AND GAMMA QUANTA OF PHOTOFISSION
FOR THE IDENTIFICATION OF FISSILE NUCLIDES

P. P. Ganich, A. S. Krivokhatskii, A. I. Lendel,   UDC 539.173.3
V. I. Lomonosov, A. I. Parlag, D. I. Sikora,
and S. I. Sychev

In [1], a method was proposed for the identification of fissile nuclides on the basis of the difference in relative yields of groups of delayed neutrons (DN) emitted by the given samples after irradiation by neutrons. In [2, 3], it was shown that the identification of fissile nuclides by this method [1] may also be performed on electron accelerators in the irradiation of the samples by delayed γ quanta; the kinetic function (KF) of the DN time distribution may be determined from the formulas

$$R^{+}(f) = \frac{n(f)}{n(1)}; \quad R^{-}(f) = \frac{n(1)-n(f)}{n(1)};$$

$$S^{+\Delta}(f) = \frac{\sum\limits_{k=f}^{f_{max}} N(k)}{n(1)}; \quad S^{-\Delta}(f) = \frac{\sum\limits_{k=1}^{f} N(k)}{n(1)}; \tag{1}$$

where $n/f = N(f)/h$; $N(f)$ is the number of DN recorded in the f-th channel of width h in irradiation to saturation.

However, in the case of photofission, the use of the method of [1] to identify fissile nuclides is limited, as is evident from Fig. 1, on account of the difference in form of the dependence of the maximum KF values, e.g., $S^{\Delta}(f)_{max}$, on the composite-nucleus parameter $(3Z_{c} - A_{c})$ on irradiation by neutrons and γ quanta of bremsstrahlung.

Thus, in fission by neutrons, $S^{\Delta}(f)_{max}$ for various fissile nuclides satisfies the equation of a straight line

$$\ln S^{\Delta}(f)_{max} = -4.143 \cdot 10^{-1} + 1.956 \cdot 10^{-3} \omega_{1}, \tag{2}$$

where $\omega_{1} = (3Z_{c} - A_{c}) - 60(Z_{c} - 90) + 5(Z_{c} - 90)^{2}$; $90 \leqslant Z_{c} \leqslant 98$; Z_{c} and A_{c} are the charge and mass number of the composite nucleus, whereas the values of $\ln S^{\Delta}(f)_{max}$ with fission by bremsstrahlung γ quanta tend to saturation, which leads to nonuniqueness of identification of ^{235}U, ^{237}Np, and ^{239}Pu. In addition, in the method of [1], indeterminacy arises because of the coincidence of the KF values of fissile nuclides and their individual mixtures.

It is not always possible to use additional information on the fissile nuclides obtained by high-reoslution spectroscopy with a high level of γ activity samples [4]. To eliminate these indeterminacies, the following kinetic functions are determined in the present work:

$$R^{+}(f, Y) = \frac{n(f)}{Y}; \quad R^{-}(f, Y) = \frac{n(1)-n(f)}{Y};$$

$$S^{+}(f, Y) = \frac{\sum\limits_{k=f}^{f_{max}} N(k)}{Y}; \quad S^{-}(f, Y) = \frac{\sum\limits_{k=1}^{f} N(k)}{Y}, \tag{3}$$

the number of DN in which is normalized to the number of fissions or the number of γ quanta of the fission fragments Y.

The curves in Fig. 2 show the KF $R^{-}(f, Y)$ and $S^{+}(f, Y)$, which are determined from the time distribution of the DN and the yield of fragments ^{133}I measured in the photofission of the nuclides ^{232}Th, ^{235}U, ^{238}U, ^{237}Np, ^{239}Pu on an M-30 microtron at an accelerating-electron energy of 15 MeV.
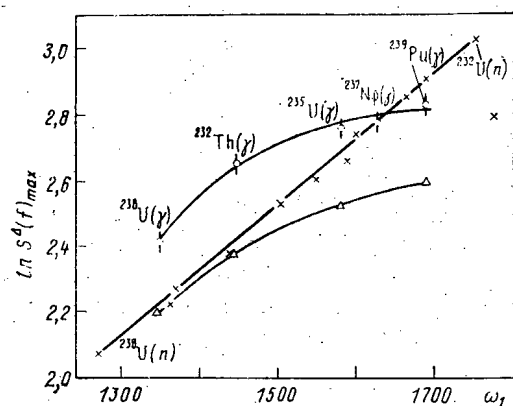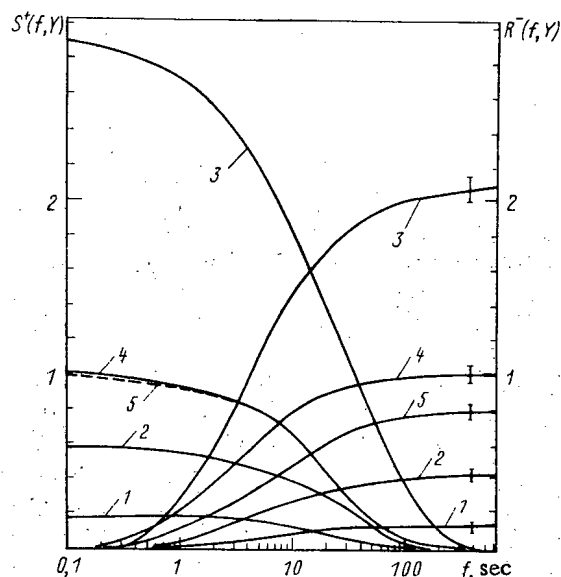
Fig. 1

Fig. 2

Fig. 1. Dependence of $\ln S^{\Delta}(f)_{max}$ on ω_1 in fission by neutrons (crosses, data of [8]) and in fission by bremsstrahlung γ quanta with a maximum energy of 15 MeV without delay in DN recording (triangles, data of [5]) and with a 0.5-sec delay in DN recording (circles).

Fig. 2. Kinetic functions $S^+(f, Y)$ and $R^-(f, Y)$ of the photofission (rel. units) of ^{239}Pu (1), ^{235}U (2), ^{232}Th (3), ^{238}U (4), ^{237}Np (5).
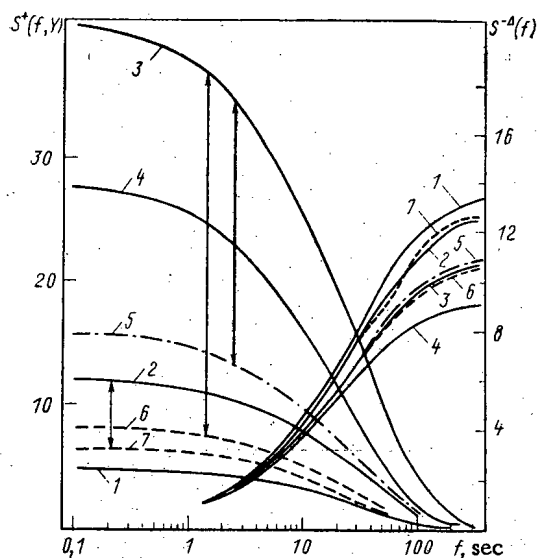
Fig. 3

Fig. 4

Fig. 3. Kinetic functions $S^+(f, Y)$ and $S^{-\Delta}(f)$ calculated on the basis of the data of [3, 5-7]: 1) ^{239}Pu; 2) ^{235}U; 3) ^{232}Th; 4) ^{238}U; 5) $^{235}U + ^{238}U$ (0.67:0.33); 6) $^{239}Pu + ^{239}U$ (0.61:0.39); 7) $^{239}Pu + ^{232}Th$ (0.71:0.29).
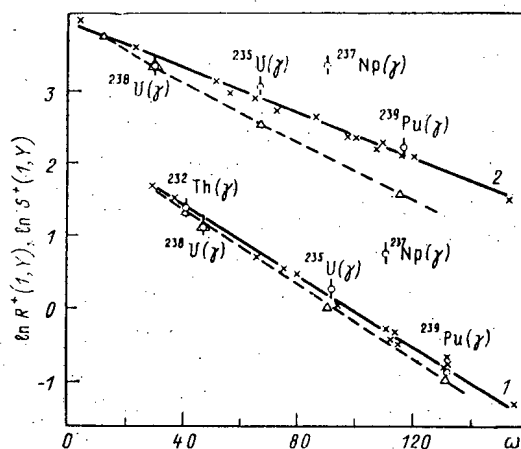
Fig. 4. Dependence of $\ln R^+(1, Y)$ and $\ln S^+(1, Y)$, respectively, on ω_2 and ω_3: O) present experiment; ×) data of [8]; Δ) data of [5]; 1) $\omega = \omega_2$; 2) $\omega = 1.724\omega_3$.

The time distribution of the DN was measured using the apparatus described in [3], after 5-min irradiation of the sample. The γ-quantum yield of ^{133}I was measured by a Ge(Li) detector after cooling the same sample for 17 h.

Retaining the same conditions in the subsequent measurement of DN and γ quanta of ^{133}I from samples of ^{232}Th, ^{235}U, ^{238}U, ^{237}Np, and ^{239}Pu on irradiation to saturation of the ac-

694

tivity of all DN groups eliminated the need to monitor the microtron electron beam and offered the possibility of directly determining the relative KF values from Eq. (3).

The values of the kinetic functions $R^-(f, Y)$ and $S^+(f, Y)$ are normalized, respectively, to the maximum values of $R^+(1, Y)$, $S^+(1, Y)$ of ^{238}U (see Fig. 2). As is evident from Fig. 2, the kinetic function $R^-(f, Y)$ and $S^+(f, Y)$ determined here are characterized by large discrimination ratios and change in their sequential order, which is due predominantly to the difference in DN yields with respect to the γ-quantum yields from ^{133}I fragments.

Change in sequential order of the KF in Eq. (3) with respect to the KF given in [2, 3] is a useful property, especially in identifying an individual fissile nuclide against a background of mixtures of fissile nuclides. This property is demonstrated in Fig. 3, where the kinetic functions $S^+(f, Y)$ and $S^{-\Delta}(f)$ are calculated on the basis of the data of [3, 5-7], under the condition that Y denotes the number of fissions.

For maximum clarity, mixtures of fissile nuclides for which the mixture value of $S^{-\Delta}(f)$ coincides, within limits of 2-5%, with the values of $S^{-\Delta}(f)$ for the individual nuclides are chosen. If the kinetic functions $S^+(f, Y)$ of the given mixtures and their individual nuclides are compared, their values are significantly different (denoted by arrows in Fig. 3), and thereby the nonuniqueness in the identification of individual fissile nuclides is eliminated. For example, the KF $S^+(f, Y)$ of ^{232}Th differs from the KF $S^+(f, Y)$ of the mixtures $^{235}U + {}^{238}U$; $^{238}U + {}^{239}Pu$. Before comparing the data, the maximum values of $R^+(1, Y)$ and $S^+(1, Y)$ measured on an M-30 microtron are normalized per 100 fissions, and on the basis of the data of [8] the following linear dependences are determined:

$$\ln R^+(1, Y) = 2.45 - 2.5 \cdot 10^{-2} \omega_2; \tag{4}$$
$$\omega_2 = (2.65 Z_c - A_c)^2 + 7.5 (Z_c - 90);$$
$$\ln S^+(1, Y) = 3.96 - 2.741 \cdot 10^{-3} \omega_3;$$
$$\omega_3 = (2.61 Z_c - A_c)^2 + 7 (Z_c - 90). \tag{5}$$

The constants in Eqs. (2), (4), and (5) are calculated from the condition that the straight lines pass through the points of maximum KF of the uranium isotopes.

It is evident from Fig. 4 that the maximum values of $R^+(1, Y)$ and $S^+(1, Y)$ for ^{232}Th, ^{235}U, ^{238}U, and ^{239}Pu agree with the data of [8], within the limits of measurement error. The deviation of $\ln R^+(1, Y)$ and $\ln S^+(1, Y)$ from a linear dependence requires further investigation and is probably associated with the presence in the sample of fissile-nuclide impurities which are difficult to determine.

It remains to thank our co-workers at the M-30 microtron of the Institute of Nuclear Research, Academy of Sciences of the Ukrainian SSR, for assistance in the work.

LITERATURE CITED

1. G. Keepin, in: Proceedings of a Symposium on Safeguards Research and Development, WASH-1076, USAEC (1967), p. 150.
2. M. M. Forosh et al., At. Energ., 35, No. 1, 59 (1973).
3. B. M. Aleksandrov et al., At. Energ., 44, No. 6, 526 (1978).
4. V. I. Lomonosov and D. I. Sikora, Preprint No. 78-7, Institute of Nuclear Research, Academy of Sciences of the Ukrainian SSR [in Russian], Kiev (1978).
5. O. P. Nikotin and K. A. Petrzhak, At. Energ., 20, No. 3, 268 (1966).
6. J. Caldwell and E. Dowdy, Nucl. Sci. Eng., 56, 179 (1975).
7. V. M. Gorbachev, Yu. S. Zamyatin, and A. A. Lbov, Interaction of Radiation with the Nuclei of Heavy Elements and Nuclear Fission. Handbook [in Russian], Atomizdat, Moscow (1976).
8. R. Waldo, R. Caram, and R. Mayer, Phys. Rev. C, 23, 1113 (1981).

POWER CAPACITIVE COUPLING OF ACCELERATING RESONATORS WITH HF OSCILLATOR

V. S. Panasyuk, Yu. K. Samoshenkov, and M. F. Simanovskii

UDC 621.384.6(088.8)

INTRODUCTION

At the present time, loop coupling is, as a rule, used in accelerators to supply hf power to the accelerating structure. This concerns both accelerators with direct coupling of the accelerating resonators with the oscillator tubes [1, 2] and accelerators in which the accelerating resonators are connected to the hf oscillator by a feeder of arbitrary length [3, 4]. However, in early papers on accelerators, e.g., cyclotrons, the possibility of using capacitive coupling of the anode loops of the oscillator tubes with the accelerating resonators in mentioned [1]. In contrast to the terminology adopted for describing self-excited oscillators, when capacitive and loop coupling refer to coupling of the grid circuits of the radio tubes with the oscillatory circuits, here we are talking about anode loops, so that in what follows we shall call this type of coupling power coupling. For unknown reasons, power capacitive coupling has not found widespread application. Meanwhile, in many cases, it has advantages, which are clearly evident in small accelerators with sealed oscillator tubes and in large accelerators with demountable tubes.

In what follows, we describe the characteristics of power capacitive coupling and the specific construction of ion and electron accelerators based on it. The accelerators described, due to their structural characteristics, acquired as a result of the use of power capacitive coupling, are highly portable and form a base for the production of sealed or evacuated accelerators, intended for use in the national economy. Thus, e.g., an electron accelerator, constructed in a sealed form, is a unique x-ray apparatus with vacuum step-up transformer based on a resonator (without the solid insulation), assimilated a long time ago in accelerator technology, but practically not used in x-ray apparatus. We also present some considerations concerning the use of power capacitive coupling in accelerating resonators with relatively large average reactive power, e.g., in resonance systems of cyclotrons, combined with demountable oscillator tubes.

It should be noted that all cases of power capacitive coupling described below are examined in application to self-excited oscillators with the tube coupled directly to the resonator. Excitation of accelerating structures from powerful oscillators through a feeder by means of capacitive coupling is useful in many cases, but falls outside the scope of the structures discussed here.

CHARACTERISTICS OF POWER CAPACITIVE COUPLING

We shall first examine some characteristics of capacitive coupling of an accelerating resonator with an hf oscillator. Figure 1 shows the equivalent circuits of two variants of capacitive (a, b) and, for comparison, a loop (c) coupling. In all three cases shown, the
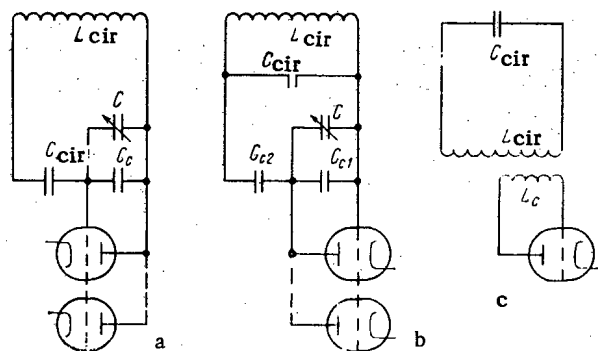

Fig. 1. Equivalent circuits of capacitive (a, b) and loop (c) coupling of anode loops of oscillator tubes with an accelerating resonator.
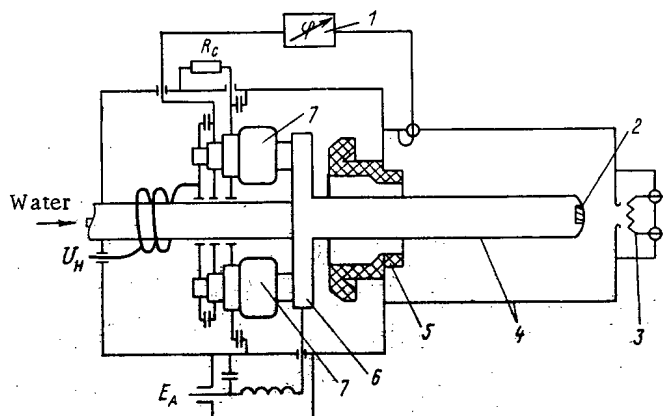
Fig. 2   Fig. 3

Fig. 2. Structural diagram of electron accelerators with power capacitive coupling: 1) phase shifter in the feedback circuit; 2) tungsten target; 3) thermocathode; 4) vacuum coaxial resonator; 5) metalloceramic insulator—capacitor; 6) collector of the tubes (anodic tank); 7) oscillator tubes.
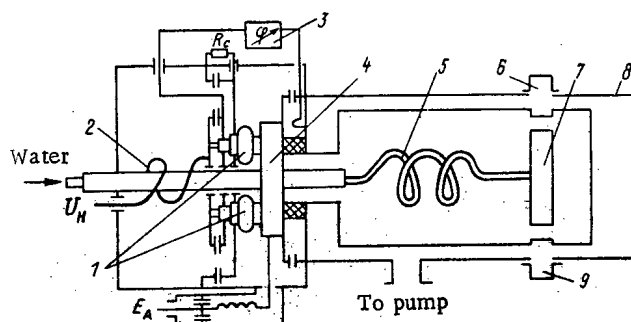
Fig. 3. Structural diagram of proton accelerator with power capacitive coupling: 1) oscillator tubes; 2) cathodic spiral resonator; 3) phase shifter in feedback circuit; 4) collector of tubes (anodic tank); 5) spiral electrode of resonator; 6) proton source; 7) drift tube; 8) vacuum chamber; 9) foil proton energy meter.

tube is not completely included in the resonance circuit, since in practice the accelerating voltage is always much greater than the hf potential on the anode of the tube.

In variant 1a, the capacitive coupling divider consists of the total capacitance of the circuit C_{cir} and the artificially introduced capacitance C_c connected in series with C_{cir}. In variant 1b, the capacitive coupling divider is constructed separately. A common advantage of the capacitive coupling, for the two variants, over loop coupling is the fact that the interelectrode capacitances of the tubes automatically enter into the lower branch of the capacitive divider. The choice of variant is determined by the specific conditions. In the real structure, corresponding to the scheme shown in Fig. 1a, the high-voltage electrode in the voltage unit for connecting the capacitive coupling must be insulated. In this case the anode voltage of the oscillator tubes can be used to suppress the resonance hf discharge (multiplicator) [5]. If this solution is structurally difficult to implement, which, as a rule, occurs only in large resonators, variant 1b automatically remains. Since the coupling capacitance (C_c or C_{c_1}) can be made from an evacuated volume, it is possible to implement a simpl. setup for operational change of the coupling coefficient with the help of a "variable" capacitor (C) with any construction. Such regulation in the case of loop coupling (see Fig. 1c) is much more complicated.

It should be noted that in the variant of coupling with the additional divider (see Fig. 1b), the capacitances of this divider cannot be selected arbitrarily. We can say roughly that the modulus of the reactive resistance of the lower branch of the divider must be approximately an order of magnitude smaller than the rescaled equivalent shunt resistance of the resonator (including the beam load) connected in parallel to it. In practice, this choice of capacitances with the usual values of the shunting resistance encountered should not give rise to any difficulties.

For comparison, Fig. 1c shows the equivalent circuit of the loop coupling with the accelerating resonator. It is evident that the unavoidable appearance of a two-circuit system in principle makes it difficult to tune the self-excited oscillator to operate at the frequency of the accelerating resonator and to obtain the required coupling coefficient, especially when the tubes are connected in parallel. Of course, in practice, capacitive coupling unavoidably involves a parasitic inductance. However, the characteristic frequency of the parasitic circuit (circuit of the tubes) can easily be displaced from the characteristic frequencies even in the decimeter wavelength range. This circumstance removes the limitation on parallel connection of oscillator tubes and thereby facilitates the construction of quite powerful hf oscillators.
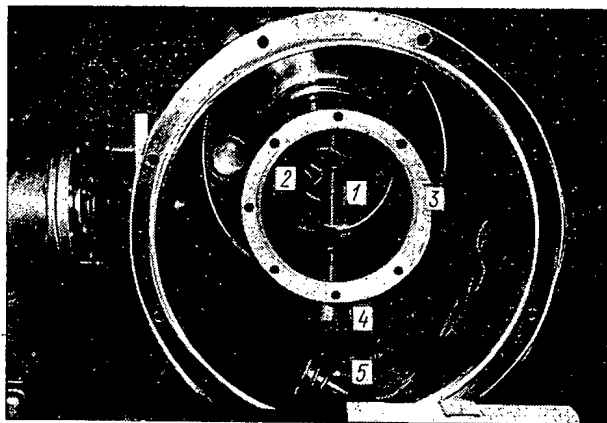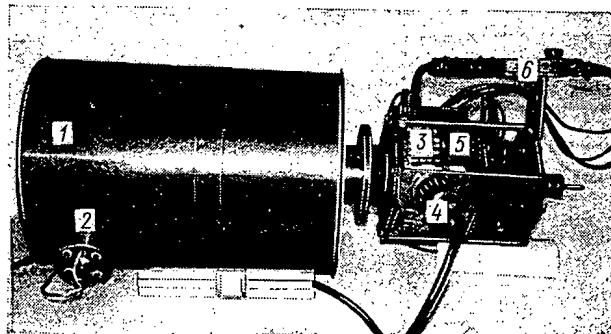
697

Fig. 4

Fig. 5

Fig. 4. Proton accelerator with the cover of the vacuum chamber removed: 1) drift tube; 2) spiral electrode; 3) outer electrode of the resonator; 4) foil proton energy meter; 5) capacitive accelerating voltage sensor.

Fig. 5. Proton accelerator in assembled form without the vacuum chamber: 1) outer electrode of the resonator; 2) foil proton energy meter; 3) coupling capacitors; 4) anode voltage input; 5) oscillator tubes; 6) phase shifter and feedback circuit.

It should be noted especially that with capacitive coupling of the resonance circuit with the tube, filtering of the higher harmonics of the components of the anode current of the tube is greatly improved compared with the case of loop coupling. Certain difficulties at this level are encountered in circuits for exciting oscillators with a grounded grid, but these difficulties are also easily overcome by the methods described in [6].

SMALL ELECTRONIC AND IONIC ACCELERATORS BASED ON A SELF-EXCITED OSCILLATOR

WITH POWER CAPACITIVE COUPLING WITH AN ACCELERATING RESONATOR

In these accelerators, the hf oscillator is placed directly in the accelerating resonator and is constructed based on four metalloceramic GI-39B tubes, connected in parallel. The peak pulse power of the oscillator is ∿400 kW and the average power is ∿1.2 kW. To increase the operational stability of the self-excited oscillator at the fundamental frequency, an external feedback through a coaxial feeder is used in accelerators.

Both accelerators are fed from a modulator, constructed according to a novel three-phase scheme without a power transformer [7, 8]. The pulse duration at the output of the modulator is 30 μsec and the amplitude is 20 kV, the pulse power is ∿1 MW, and the repetition frequency is 50 and 150 Hz and down to 1 Hz (single-pulse mode).

The electron accelerator is constructed according to the fundamental scheme described in [9], using power capacitive coupling as in Fig. 1a. Figure 2 shows the structural scheme of the accelerator. The inner electrode of the coaxial accelerating resonator is insulated from the housing and is affixed directly to the collector of the tubes, which permits simultaneously cooling the collector and the inner electrode with running water and using the anode voltage of the tubes to suppress the resonance hf discharge in the resonator.

The characteristic resonance frequency of the resonator is 210 MHz, the Q factor of the resonator is 3500, and the shunt resistance is 320 kΩ. A maximum accelerating voltage of 420 kV was achieved in the accelerator. The construction and parameters of the accelerator are described in greater detail in [10]. An x-ray apparatus, intended for diagnostics of the quality of seams in oil and gas pipelines, is currently being developed based on the accelerator described above.

The ion (proton) accelerator is based on a four-wave coaxial spiral resonator with a drift tube, attached to the high voltage end of the spiral electrode. Power capacitive coupling, according to Fig. 1a, is likewise used in the accelerator. The structural diagram of the accelerator is shown in Fig. 3. The low-voltage end of the spiral inner electrode of the resonator is attached directly to the collector of the tubes, and the coupling capacitor is inserted between the collector and the housing. As also in the electron accelerator, the
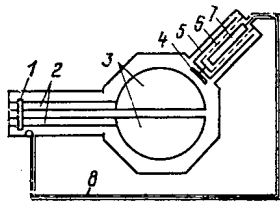
Fig. 6. Possible structural scheme of a cyclotron with power capacitive coupling and demountable oscillator tube: 1) short circuit; 2) resonance lines; 3) dee; 4) electrode of additional capacitive coupling divider; 5, 6, 7) anode, grid, and cathode of demountable oscillator tube, respectively; 8) feedback feeder.

collector of the tubes, the spiral electrode, and the drift tube are cooled by running water, while the anode voltage of the tubes is used to suppress the resonance hf discharge in the resonator.

The Q factor of the spiral resonator in the given design is 2800, the shunt resistance is 900 kΩ, and the resonance frequency is 37 MHz. The maximum accelerating voltage on the drift tube relative to the housing is 600 kV.

In the accelerator, a controllable capillary proton source, guaranteeing a quasirectangular proton current pulse with amplitudes up to 40 mA with duration 30 μsec (at the source output), is used. The maximum repetition frequency of the ionic current pulses for the given source is 1 Hz, which restricts the frequency of the working pulses of the accelerator. The source is the timing (tuning) unit of the accelerator and will be replaced by a different design.

The following parameters were achieved in setting up the accelerator: maximum proton energy at the output $\geqslant 1\,\mathrm{MeV}$; maximum beam current in the pulse about 5 mA.

A photograph of the external view of the accelerator (view from the side of the resonator with the covers removed) is shown in Fig. 4. Figure 5 gives a general view of the construction of the accelerator, in which the accelerator is shown outside the evacuated volume.

APPLICATION OF POWER CAPACITIVE COUPLING IN ACCELERATING
RESONATORS WITH HIGH AVERAGE REACTIVE POWER

As an example of a resonant system with high average reactive power, we shall examine the dee cyclotron circuit.

In practically all cyclotrons, loop coupling of the hf oscillator with the resonant system is currently used. Meanwhile, power capacitive coupling, which has, in addition to the characteristics noted above, other properties characteristic precisely of this case, can also be used in this case. We note that it is structurally difficult to use capacitive coupling in a cyclotron with insulated resonance lines and with the capacitive coupling inserted in the voltage unit (see Fig. 1a), due to the high average reactive power and the concomitant large size of the system, so that we shall examine a variant with an additional divider (see Fig. 1b). In this variant the coupling element must be placed at the peak of the electric field (the approximate structural scheme of such a cyclotron is shown in Fig. 6). In this case it turns out to be far removed from the frequency-tuning mechanism, which greatly simplifies the operational adjustment of the frequency with a change in the final energy of the particles in the cyclotron; in addition, in the entire working frequency range the coupling coefficient (or coefficient of transformation of the hf voltage from the anode of the tube to the dee) is determined practically only by the ratio of the capacitances of the coupling divider. The effect of the large average power of the system imposes corresponding requirements on the construction of the coupling divider; apparently, the coupling capacitances in the form of water-cooled vacuum capacitors will permit satisfying these requirements in most cases. Moreover, it is possible to combine the electrodes of the coupling capacitor with the electrodes of the oscillator tube and thereby realize the well-known idea of unifying the vacuums of the oscillator tube (which is demountable) and of the accelerating resonator (Fig. 6 shows precisely this variant). In other words, the idea of a demountable oscillator tube in a demountable evacuated accelerating resonator is becoming very promising in connection with the application of power capacitive coupling.

LITERATURE CITED

1. M. Livingston, T. Rose, and M. Namias, The Cyclotron. Collection of Papers [Russian translation], Gostekhteorizdat, Moscow (1948), p. 267.
2. V. G. Abdul'manov et al., Preprint IYaF 78-25, Novosibirsk (1978).
3. D. Armstrong et al., Part. Accel., 6, 175 (1975).
4. A. V. Shal'nov et al., in: Theory, Calculation, and Experimental Work on Charged Particle Accelerators [in Russian], Énergoizdat, Moscow (1982), p. 75.
5. I. N. Slivkov, Electrical Insulation and Vacuum Discharge [in Russian], Atomizdat, Moscow (1972), p. 161.
6. Yu. A. Grits et al., Prib. Tekh. Eksp., No. 6, 39 (1966).
7. V. S. Panasyuk et al., Inventor's Certificate No. 815895, Byull. Izobret., No. 11, 233 (1981).
8. V. S. Pansyuk, Yu. K. **Samoshenkov**, and M. F. Simanovskii, Prib. Tekh. Eksp., No. 4, 124 (1982).
9. Yu. A. Akimov et al., Inventor's Certificate No. 776529, Byull. Izobret., No. 1, 278 (1982).
10. V. S. Panasyuk, Yu. K. Samoshenkov, and M. F. Simanovskii, Prib. Tekh. Eksp., No. 4, 31 (1983).

EFFECTS OF OVERLAPPING OF X-RAY LINES IN GAMMA ACTIVATION OF NUCLEI

M. G. Davydov and V. G. Magera

UDC 543.0

In recording characteristic x rays in γ activation analysis, the relation of the spectra to the type of radionuclide transformation leads to the appearance of special effects of the overlapping of lines in the spectra of activated samples. The emission of x rays is associated mainly with such types of radionuclide decay as an isomeric transition accompanied by internal conversion, and electron capture. By considering the types of photonuclear reactions and the types of radionuclide transformations it is possible to classify the effects of overlapping of lines, and then to systematize the cases of such overlapping which are important for γ activation analysis.

The first type of overlapping of lines is related to photonuclear reactions on isotopes of the element being determined, whose decay products give x-rays of the same atoms. In this case there is an amplification of the analysis signal, which is formed of several components having different decay constants. The number of counts N in the photopeak of an analytic line of energy E used to determine the content of the element can in this case be recorded on the basis of an expression for the signal in γ activation analysis [1], modified for a variation of the recording of x rays [2]. If, for simplicity, we ignore factors which are not essential for treating the effect of overlapping of lines, the expression for the analytic signal can be written in the form

$$N = k \frac{m\theta}{A}\, y(E_0)\, n\, \frac{1}{\lambda}\, (1 - e^{-\lambda t_0})\, e^{-\lambda t_n}\, (1 - e^{-\lambda t_c}),$$

where m is the mass of the element being determined; θ, A, isotopic content and atomic mass of the initial nuclei; $y(E_0)$, reduced yield of photonuclear reactions at the upper limit of the bremsstrahlung E_0; n, absolute yield of photons of energy E of the radionuclide-product activation; λ, decay constant of this radionucldie; and t_0, t_n, t_c, irradiation, waiting, and counting times, respectively. The factor k characterizes the parameters of the bremsstrahlung beam irradiating the sample.

It is clear that different values of λ and $y(E_0)$ for the components of the analytic signal give a further possibility for controlling them by varying the time conditions and the energy E_0, and this in general cannot be ignored in choosing optimum conditions of analysis.

We present examples of the first type of overlapping of lines in γ activation analysis. In the γ activation of nickel there was observed the 6.93-keV K_α line of Co, which contained

___

three components formed in the reactions: $^{58}Ni(\gamma, n)^{57}Ni$, $T_{1/2} = 36.16$ h, $n = 16.53\%$; $^{58}Ni(\gamma, 2n)^{56}Ni$, $T_{1/2} = 6.1$ days, $n = 27.83\%$; $^{61}Ni(\gamma, p^m)^{60m}Co$, $T_{1/2} = 10.47$ min, $n = 28.01\%$. In the activation of gallium there was observed the 8.63-keV K_α line of Zn, which also contains three components formed in the reactions: $^{69}Ga(\gamma, n)^{68}Ga$, $T_{1/2} = 68$ min, $n = 3.75\%$; $^{69}Ga(\gamma, 2n)^{67}Ga$, $T_{1/2} = 78.26$ h, $n = 46.43\%$; $^{71}Ga(\gamma, pn^m)^{69m}Zn$, $T_{1/2} = 14$ h, $n = 1.5\%$. The presence of several components in the analytic or interfering signal can substantially change the optimal conditions of γ activation analysis in the recording of x rays as compared with optimal conditions of the classical version of γ activation analysis.

The second type of overlapping of lines is determined by the first-order primary interference reactions, well known in γ activation analysis. The systematic error due to interference of this type can be obtained from the relations or graphs in [3]. We present an example of this type of overlapping of x-ray lines in γ activation analysis for the pair of elements Sr—Y in the recording of the 14.14-keV K_α line of Sr, formed as a result of the following photonuclear reactions: $^{88}Sr(\gamma, n^m)^{87m}Sr$, $T_{1/2} = 2.805$ h, $n = 8.24\%$ and $^{89}Y(\gamma, 2n)^{87}Y \cdot$

$$\xrightarrow[T_{1/2}=80.3\,h]{\beta^+} {}^{87m}Sr, \quad T_{1/2} = 2.805 \text{ h}, \quad n = 60.52\%.$$ In addition to these reactions, contribution

to the K_α line of Sr are also made by other reactions on strontium and yttrium isotopes, i.e., overlapping of lines of the first type will occur: $^{89}Y(\gamma, n)^{88}Y$, $T_{1/2} = 106.6$ days, $n = 52.77\%$; $^{86}Sr(\gamma, n^m)^{85m}Sr$; $T_{1/2} = 67.7$ min, $n = 1.29\%$; $^{87}Sr(\gamma, 2n^m)^{85m}Sr$, $T_{1/2} = 67.7$ min, $n = 1.29\%$; $^{87}Sr(\gamma, \gamma')^{87m}Sr$, $T_{1/2} = 2.805$ h, $n = 8.24\%$.

The yield of the K_α line of Sr is negligible for the second and third reactions, since a radionuclide with a long half-life is formed in the first reaction, and therefore the contribution of the reactions listed to the analytic signal will be **relatively small.** The fourth reaction clearly cannot be ignored.

The effects of the overlapping of lines because of photonuclear reactions on nuclei of the matrix with atomic numbers Z_i, which may be appreciably different from the atomic number Z_0 of nuclei of the element being determined, are characteristic for γ activation analysis

with the recording of x rays. Here $|Z_0 - Z_i| \leqslant 3$: $_{Z_0}A(\gamma, n)_{Z_0}A^* \xrightarrow{\beta^-} X_K\, _{Z_0+1}B$, but $_{Z_0+3}D(\gamma, p)_{Z_0+2}C^* \xrightarrow{\text{el. cap}, \beta^+}$

$X_K\, _{Z_0+1}B$. This specific interference appreciably exceeds the number of cases of overlapping of lines. Here Z_0 is the atomic number of the element being determined, the Z_i are the atomic numbers of the interfering elements of the matrix of the sample, X_K is the x-ray K radiation of the radioisotope, and $Z_{0+1}B$ is the element corresponding to the **emission of X_K x-ray** radiation by a product of a photonuclear reaction.

For the first and third types of overlapping, if the analytic signal from the element A being determined and the interfering signals are each formed in their own photonuclear reaction, and if the final activation products do not have decay chains, the interference coefficient will have the form

$$L(E_0, t_0, t_n, t_c) = \frac{A_A \lambda_A}{m_A 0_A n_A y_A f_{tA}} \sum_i \frac{m_i \theta_i n_i y_i f_{ti}}{A_i \lambda_i},$$

where i is the number of interfering reactions which contribute to the analytic **photopeak;** $f_{ti} = (1 - e^{-\lambda_i t_0})e^{-\lambda_i t_n}(1 - e^{-\lambda_i t_c})$ is the time factor for the reference reaction (i = A) or for the interfering reactions.

TABLE 1. Experimental L_e and Calculated L_c Interference Coefficients

Element being determined	Interfering element	L_e	L_c
Co	Ni	0,056±0,002	0,032
Cd	In	0,83±0,01	0,98
In	Sn	0,11±0,01	0,15
Sr	Y	0,037±0,002	0,02
La	Ba	0,11±0,01	0,16

701

Taking account of the characteristics of the formation of x rays in radioactive decay, the absolute quantum yield will be $n = \omega_K \nu_{K \text{ el.cap}}$ for electron capture, and $\omega_K \sum_l \alpha_{Kl} n_l$ for internal conversion. Here ω_K is the fluorescence yield from the K shell; $\nu_{K\text{el.cap}}$, fraction of the decays with electron capture in the K shell; α_{Kl}, internal conversion coefficient for photons of the l-th energy; and n_l, absolute yield of photons of the l-th energy per decay.

It is important that the interference coefficient in these cases depends strongly on the time conditions, since the decay constants for the signal and the interfering reactions are generally different. By choosing an optimal measurement procedure, the effect of interfering elements on the result of the analysis can be reduced to a minimum.

For several pairs of elements for which the necessary data on the photonuclear reaction parameters are known, we determined the interference coefficients experimentally and compared them with the results calculated by the relation given (Table 1).

Samples in the form of tablets made by pressing a mixture of a simple compound of the element (oxide or salt) and boric acid were irradiated with bremmstrahlung from a linear electron accelerator with a 7-μA electron beam current under the following conditions: $E_0 = 25$ MeV, $t_0 = 10$ min, $t_n = t_c = 30$ min. The spectra were recorded by a BDRK-1-25 Si-Li detector (energy resolution 300 eV for a 6.4-keV radiation from ^{57}Co) and an AI-1024-4 analyzer. In view of the uncertainty in the input nuclear data, the agreement between the calculated and experimental results is satisfactory. It should be noted that because of the lack of sufficiently reliable data on the photonuclear reaction parameters, an assessment of the effect of interference on the results of the analysis cannot often be calculated.

By taking account of the three types of overlapping of lines in x-ray spectra of samples activated by bremsstrahlung from electron accelerators, both the estimates of the expected systematic errors and the calculations of optimal conditions of γ activation analysis can be substantially improved. The relations given for taking account of the effects of overlapping together with a systematization of the cases of overlapping of x-ray lines in γ activation analysis make it possible to avoid systematic errors in the development of specific methods, and to refine the optimal conditions of analysis.

LITERATURE CITED

1. M. G. Davydov and V. A. Shcherbachenko, At. Energ., **39**, No. 3, 210 (1975).
2. M. G. Davydov et al., Izv. Severo-Kavkazkovo Nauch. Tsentra Vysshei Shkoly. Estestv. Nauki No. 3, 5 (1981).
3. M. G. Davydov et al., Radiochem. Radioanal. Lett., No. 35, 67 (1978).

MEASUREMENTS OF THE SPECTRA OF FAST NEUTRONS IN THE CHANNELS OF
THE SUBCRITICAL SO-2M ASSEMBLY

V. A. Kamnev, V. P. Skopin,
and V. S. Troshin

We consider in the present article the main results of measurements of the spectra of fast neutrons in the channels of the SO-2M neutron breeder reactor, which forms part of the equipment for enriching ore with the neutron activation technique [1, 2].

The SO-2M neutron breeder reactor is a subcritical nuclear assembly in which fission reactions of uranium nuclei are supported by the introduction of an external neutron source into the core (Fig. 1). The main part of the assembly is a homogeneous core which is built from cylindrical fuel elements. UO_2 with 36% ^{235}U enrichment, dispersed in polyethylene, is used as the material undergoing fission. The core with a graphite reflector is surrounded by a heavy-concrete radiation shield with a specific weight of $4.4 \cdot 10^4$ N/m^3. The maximum thermal power is 10 W and the total neutron flux of the source is $5 \cdot 10^9$ sec^{-1}.

Knowledge of the actual energy spectrum of the neutrons is of great importance for selecting the conditions and the method for developing the ore irradiation. A set of eight threshold detectors (Table 1) which have the shape of disks with a diameter of 19 mm was used to determine the spectra. The detectors were irradiated in ore irradiation channels (OCh) with a diameter of 92 mm on the level of the core's center (point of OCh-2) and at points situated 80 mm above (OCh-1) and 120 mm below (OCh-3) that level; the detectors were also irradiated in the vertical experimental channels VECh-1 and VECh-2 with a diameter of 30 or 65 mm on the level of the core's center (Fig. 2). This set of detectors rather completely covers the energy range 112-1360 fJ (0.7-8.5 MeV). A commercial "Protoka" 4π-β counter

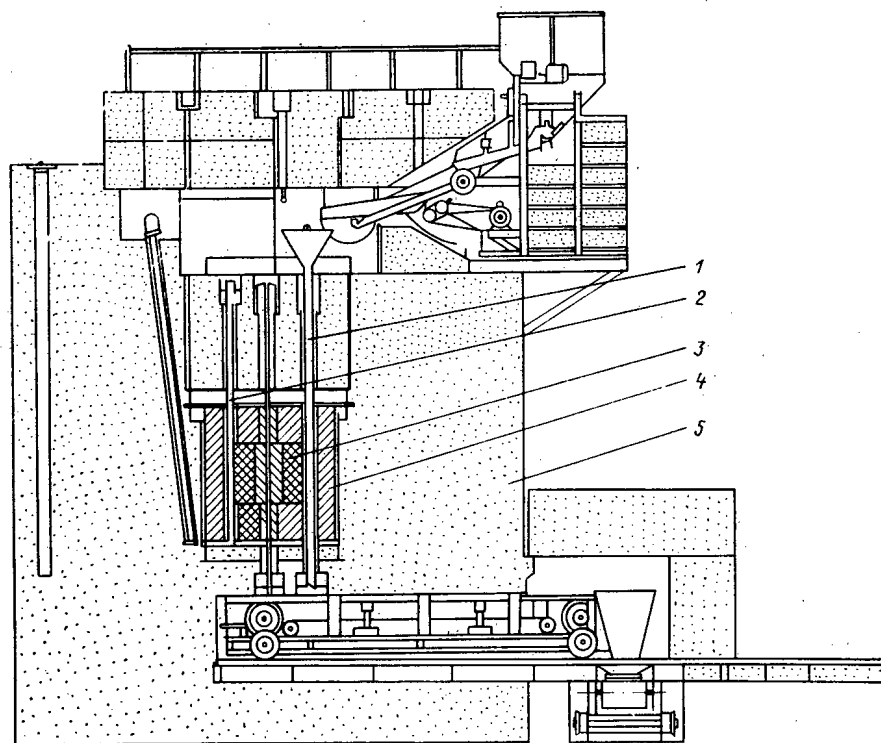Fig. 1. SO-2M neutron **breeder** reactor: 1) OCh channel; 2) VECh-2 channel; 3) core; 4) graphite reflector; 5) radiation shield.

TABLE 1. Activation Integrals Q_i

Reaction	σ_{eff}, mb	E_{eff}, MeV	Q_i, sec^{-1}				
			OCh$_1$	OCh$_2$	OCh$_3$	VECh-1	VECh-2
^{103}Rh (n, n')	920	0,70	$2{,}67 \cdot 10^{-17}$	$3{,}18 \cdot 10^{-17}$	$1{,}66 \cdot 10^{-17}$	$1{,}31 \cdot 10^{-17}$	$1{,}15 \cdot 10^{-17}$
^{31}P (n, p)	101	2,30	$9{,}44 \cdot 10^{-19}$	$1{,}13 \cdot 10^{-18}$	$5{,}40 \cdot 10^{-19}$	$3{,}84 \cdot 10^{-19}$	$3{,}23 \cdot 10^{-19}$
^{32}S (n, p)	306	3,00	$1{,}75 \cdot 10^{-18}$	$2{,}14 \cdot 10^{-18}$	$1{,}00 \cdot 10^{-18}$	$7{,}13 \cdot 10^{-19}$	$5{,}81 \cdot 10^{-19}$
^{35}Cl (n, α)	190	3,70	$6{,}56 \cdot 10^{-19}$	$8{,}11 \cdot 10^{-19}$	$3{,}75 \cdot 10^{-19}$	$2{,}72 \cdot 10^{-19}$	$2{,}20 \cdot 10^{-19}$
^{27}Al (n, p)	51	4,40	$1{,}08 \cdot 10^{-19}$	$1{,}35 \cdot 10^{-19}$	$6{,}27 \cdot 10^{-20}$	$4{,}59 \cdot 10^{-20}$	$3{,}67 \cdot 10^{-20}$
^{56}Fe (n, p)	56,6	6,40	$3{,}03 \cdot 10^{-20}$	$3{,}74 \cdot 10^{-20}$	$1{,}79 \cdot 10^{-20}$	$1{,}26 \cdot 10^{-20}$	$1{,}01 \cdot 10^{-20}$
^{24}Mg (n, p)	122,3	7,00	$4{,}28 \cdot 10^{-20}$	$5{,}26 \cdot 10^{-20}$	$2{,}57 \cdot 10^{-20}$	$1{,}80 \cdot 10^{-20}$	$1{,}44 \cdot 10^{-20}$
^{27}Al (n, α)	65,7	7,20	$1{,}97 \cdot 10^{-20}$	$2{,}56 \cdot 10^{-20}$	$1{,}22 \cdot 10^{-20}$	$8{,}28 \cdot 10^{-21}$	$6{,}77 \cdot 10^{-21}$

TABLE 2. Differential Energy Density of the Flux of Fast Neutrons in the OCh, VECh-1, and VECh-2 Channels of the SO-2M Neutron Breeder Reactor

E, MeV	$\varphi(E)$, cm$^{-2} \cdot$sec$^{-1} \cdot$MeV^{-1}										
	OCh$_1$			OCh$_2$		OCh$_3$		VECh-1		VECh-2	
	EM	IDM	MPM	EM	IDM	EM	IDM	EM	IDM	EM	IDM
0,7	$2{,}17 \cdot 10^7$	$1{,}94 \cdot 10^7$	$2{,}35 \cdot 10^7$	$2{,}36 \cdot 10^7$	$2{,}08 \cdot 10^7$	$1{,}40 \cdot 10^7$	$1{,}25 \cdot 10^7$	$1{,}66 \cdot 10^7$	$1{,}83 \cdot 10^7$	$1{,}35 \cdot 10^7$	$1{,}30 \cdot 10^7$
1,2	$1{,}44 \cdot 10^7$	$1{,}42 \cdot 10^7$	$1{,}61 \cdot 10^7$	$1{,}67 \cdot 10^7$	$1{,}62 \cdot 10^7$	$9{,}74 \cdot 10^6$	$9{,}31 \cdot 10^6$	$5{,}75 \cdot 10^6$	$6{,}45 \cdot 10^6$	$6{,}28 \cdot 10^6$	$6{,}56 \cdot 10^6$
1,7	$9{,}92 \cdot 10^6$	$1{,}00 \cdot 10^7$	$1{,}15 \cdot 10^7$	$1{,}18 \cdot 10^7$	$1{,}18 \cdot 10^7$	$6{,}29 \cdot 10^6$	$6{,}31 \cdot 10^6$	$3{,}72 \cdot 10^6$	$3{,}90 \cdot 10^6$	$3{,}79 \cdot 10^6$	$3{,}92 \cdot 10^6$
2,2	$6{,}93 \cdot 10^6$	$7{,}02 \cdot 10^6$	$7{,}28 \cdot 10^6$	$8{,}36 \cdot 10^6$	$8{,}44 \cdot 10^6$	$4{,}18 \cdot 10^6$	$4{,}25 \cdot 10^6$	$2{,}65 \cdot 10^6$	$2{,}68 \cdot 10^6$	$2{,}48 \cdot 10^6$	$2{,}53 \cdot 10^6$
2,7	$4{,}87 \cdot 10^6$	$4{,}92 \cdot 10^6$	$5{,}05 \cdot 10^6$	$5{,}92 \cdot 10^6$	$5{,}98 \cdot 10^6$	$2{,}85 \cdot 10^6$	$2{,}90 \cdot 10^6$	$1{,}91 \cdot 10^6$	$1{,}91 \cdot 10^6$	$1{,}68 \cdot 10^6$	$1{,}70 \cdot 10^6$
3,2	$3{,}43 \cdot 10^6$	$3{,}45 \cdot 10^6$	$3{,}50 \cdot 10^6$	$4{,}19 \cdot 10^6$	$4{,}22 \cdot 10^6$	$1{,}97 \cdot 10^6$	$1{,}99 \cdot 10^6$	$1{,}38 \cdot 10^6$	$1{,}37 \cdot 10^6$	$1{,}16 \cdot 10^6$	$1{,}17 \cdot 10^6$
3,7	$2{,}42 \cdot 10^6$	$2{,}43 \cdot 10^6$	$2{,}45 \cdot 10^6$	$2{,}96 \cdot 10^6$	$2{,}98 \cdot 10^6$	$1{,}38 \cdot 10^6$	$1{,}39 \cdot 10^6$	$9{,}86 \cdot 10^5$	$9{,}82 \cdot 10^5$	$8{,}10 \cdot 10^5$	$8{,}11 \cdot 10^5$
4,2	$1{,}70 \cdot 10^6$	$1{,}71 \cdot 10^6$	$1{,}71 \cdot 10^6$	$2{,}10 \cdot 10^6$	$2{,}10 \cdot 10^6$	$9{,}67 \cdot 10^5$	$9{,}71 \cdot 10^5$	$7{,}05 \cdot 10^5$	$7{,}03 \cdot 10^5$	$5{,}68 \cdot 10^5$	$5{,}69 \cdot 10^5$
4,7	$1{,}20 \cdot 10^6$	$1{,}20 \cdot 10^6$	$1{,}20 \cdot 10^6$	$1{,}48 \cdot 10^6$	$1{,}49 \cdot 10^6$	$6{,}82 \cdot 10^5$	$6{,}84 \cdot 10^5$	$5{,}03 \cdot 10^5$	$5{,}02 \cdot 10^5$	$4{,}00 \cdot 10^5$	$4{,}00 \cdot 10^5$
5,2	$8{,}49 \cdot 10^5$	$8{,}49 \cdot 10^5$	$8{,}50 \cdot 10^5$	$1{,}05 \cdot 10^6$	$1{,}05 \cdot 10^6$	$4{,}83 \cdot 10^5$	$4{,}84 \cdot 10^5$	$3{,}58 \cdot 10^5$	$3{,}58 \cdot 10^5$	$2{,}83 \cdot 10^5$	$2{,}83 \cdot 10^5$
5,7	$6{,}00 \cdot 10^5$	$5{,}99 \cdot 10^5$	$5{,}99 \cdot 10^5$	$7{,}43 \cdot 10^5$	$7{,}41 \cdot 10^5$	$3{,}43 \cdot 10^5$	$3{,}43 \cdot 10^5$	$2{,}54 \cdot 10^5$	$2{,}54 \cdot 10^5$	$2{,}00 \cdot 10^5$	$2{,}00 \cdot 10^5$
6,2	$4{,}24 \cdot 10^5$	$4{,}23 \cdot 10^5$	$4{,}25 \cdot 10^5$	$5{,}25 \cdot 10^5$	$5{,}24 \cdot 10^5$	$2{,}44 \cdot 10^5$	$2{,}44 \cdot 10^5$	$1{,}80 \cdot 10^5$	$1{,}80 \cdot 10^5$	$1{,}42 \cdot 10^5$	$1{,}42 \cdot 10^5$
6,7	$2{,}99 \cdot 10^5$	$2{,}99 \cdot 10^5$	$3{,}01 \cdot 10^5$	$3{,}72 \cdot 10^5$	$3{,}70 \cdot 10^5$	$1{,}74 \cdot 10^5$	$1{,}73 \cdot 10^5$	$1{,}28 \cdot 10^5$	$1{,}28 \cdot 10^5$	$1{,}01 \cdot 10^5$	$1{,}01 \cdot 10^5$
7,2	$2{,}12 \cdot 10^5$	$2{,}11 \cdot 10^5$	$2{,}12 \cdot 10^5$	$2{,}63 \cdot 10^5$	$2{,}62 \cdot 10^5$	$1{,}24 \cdot 10^5$	$1{,}23 \cdot 10^5$	$9{,}04 \cdot 10^4$	$9{,}03 \cdot 10^4$	$7{,}13 \cdot 10^4$	$7{,}12 \cdot 10^4$
7,7	$1{,}50 \cdot 10^5$	$1{,}49 \cdot 10^5$	$1{,}49 \cdot 10^5$	$1{,}86 \cdot 10^5$	$1{,}85 \cdot 10^5$	$8{,}85 \cdot 10^4$	$8{,}78 \cdot 10^4$	$6{,}39 \cdot 10^4$	$6{,}37 \cdot 10^4$	$5{,}07 \cdot 10^4$	$5{,}04 \cdot 10^4$
8,2	$1{,}06 \cdot 10^5$	$1{,}05 \cdot 10^5$	$1{,}05 \cdot 10^5$	$1{,}32 \cdot 10^5$	$1{,}31 \cdot 10^5$	$6{,}32 \cdot 10^4$	$6{,}26 \cdot 10^4$	$4{,}51 \cdot 10^4$	$4{,}49 \cdot 10^4$	$3{,}60 \cdot 10^4$	$3{,}57 \cdot 10^4$

was used to determine the detector counting rate. Table 1 lists the experimental information on the activation integrals. The differential spectra of the fast neutrons were compiled from the integral data of the experiment with the aid of the "express" algorithms method (EM) and with the maximum probability method (MPM) (or with the method of directed disrepancies) [3, 4]; the iterational differentiation method (IDM) of [5] was also employed in the form of a computer program. The results of the compilation of the spectra are listed in Table 2.

An analysis of the mathematical data of the measured spectra has shown that there exists satisfactory agreement between the results obtained with the various spectrum-recompilation programs. The error which was made in the determination of the spectra amounted to 15–20%
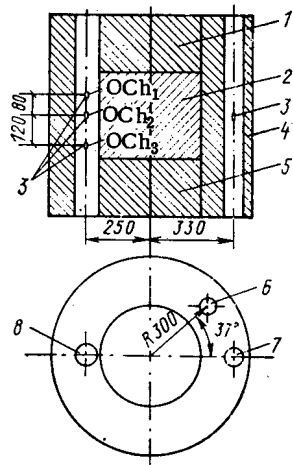

Fig. 2. Position of the experimental channels in the SO-2M neutron breeder reactor: 1) upper graphite shield; 2) core; 3) set of threshold detectors; 4) lateral graphite reflector; 5) lower graphite reflector; 6) VECh-1; 7) VECh-2; 8) OCh.

and reached its maximum in the energy ranges of lowest information value. Let us note that it is important to properly select a priori information on the shape of the unknown spectrum.

The similarity of the conditions leading to the development of the spectra in the experimental channels of the SO-2M neutron breeder reactor manifested itself in the practically identical shapes of the high-energy parts of the spectra. Differences are observed in the initial sections of the spectra at E < 480 fJ (3 MeV).

The measured differential spectra of the fast neutrons can provide information on the neutron radiation field in the graphite reflector of the subcritical SO-2M assembly so that it is possible to improve the selection of the irradiation conditions of the ore and of various samples in the use of the equipment.

LITERATURE CITED

1. Equipment for Ore Enrichment by Neutron Activation [in Russian], Leaflet of the VDNKh of the USSR, Moscow (1976).
2. A. P. Tatarnikov et al., Tsvetnye Met., No. 2, 94 (1980).
3. E. A. Kramer-Ageev, V. S. Troshin, and E. G. Tikhonov, Activation Methods in Neutron Spectrometry [in Russian], Atomizdat, Moscow (1976).
4. E. A. Kramer-Ageev and V. S. Troshin, in: The Metrology of Neutron Measurements in Nuclear Physics Equipment, Reports of the First All-Union School [in Russian], Vol. 1, Press of the Central Scientific Research Inst. of Atomic Information, Moscow (1976), p. 19.
5. A. E. Kramer-Ageev, V. S. Troshin, and G. N. Fateeva, in: Problems of Dosimetry and Radiation Shielding [in Russian], No. 20, Énergoizdat, Moscow (1980), p. 110.

INTRINSIC BACKGROUND OF THE BDÉG-6931-20 DETECTOR

I. F. Lukashin and A. M. Vinnikov   UDC 551.46.084:539.107.43

Large-volume scintillation detectors are at the present time used for in situ investigations of radioactivity fields in natural locations. These detectors have a high efficiency of recording γ radiation, but also have certain shortcomings, especially their high intrinsic background resulting from the concentration of natural radionuclides in the materials of the detector components and in the NaI(Tl) crystal proper (basically ^{40}K and members of the radioactive U and Th series). Since the specific activity of the material to be examined (seawater soil, ocean-bottom deposits) is extremely low, the concentration of the γ emitters in these materials is comparable with that of the detector materials and occasionally can be lower than that of the detector materials. It is therefore very important to have information on the spectral composition of the intrinsic detector background. The intrinsic detector background is usually determined by placing the detector in a passive shield which provides protection against the penetrating radiation of the natural radionuclides and the cosmic radiation [1-3].

A simple experimental scheme is available for detectors of gamma spectrometers used in situ in oceans. It is a well-known fact that the concentration of the salts in the water of open-ocean regions is approximately two times greater than that of the Black Sea. Since the salt composition of the seawater of open ocean areas is constant, we can assume that the spectral composition of the γ radiation of the natural radionuclides in the water of the Black Sea and of the oceans is identical, and that the γ radiation fluxes differ by a factor of two, so that the counting rates of radiation detectors in the Black Sea water and the ocean water are related by the formula

$$2N_{\mathrm{r.B.s.}}(E) = N_{\mathrm{r.oc}}(E). \tag{1}$$

When we assume that the radiation flux recorded by a detector is a superposition of the fluxes caused by the natural radionuclides (r), the cosmic radiation (c), and the intrinsic detector background (idb), the recorded counting rate must be equal (the indices for water
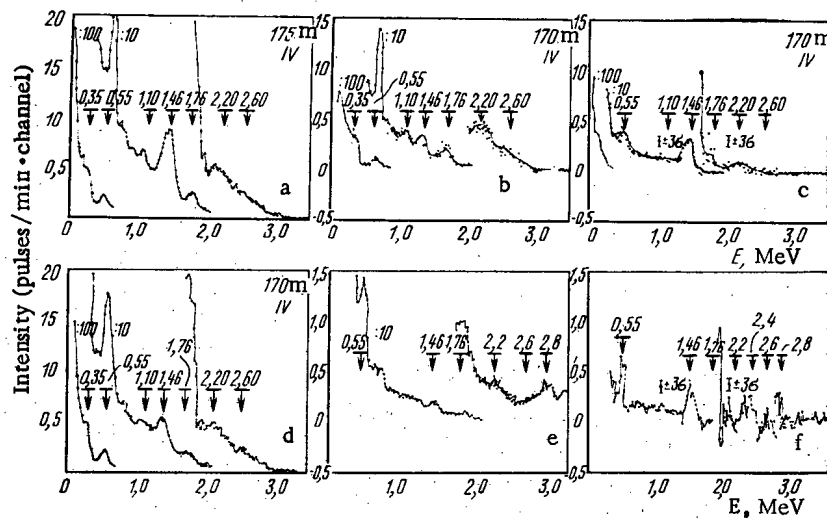
Fig. 1. Spectral composition of γ radiation of seawater and intrinsic radiation of a BD-6931-20 detector.

have been omitted):

$$N(E_1) = N_r(E) + N_c(E) + N_{idb}. \qquad (2)$$

Since for the energy range of the natural radionuclides the component N_c is very small on horizons with H ⩾ 30 m water equiv., it is possible to determine the intrinsic detector background with the formula

$$N_{idb}(E) = 2N_{B.s}(E) - N_{oc}(E). \qquad (3)$$

These formulas are valid for the natural radionuclides of the main salts of seawater. Figures 1a, d show the γ radiation spectra of the water of the Mediterranean (station 2851) and of the Black Sea (station 2853) with salt concentrations of 38‰ and 19‰, respectively, for Δt = 6 h; the spectra were obtained in a 5-day interval with the aid of the γ spectrometer of [4], which worked continuously for 120 days. The total absorption peaks of ^{40}K (1.46 MeV), ^{214}Bi (2.2, 1.76, 1.12, 0.61 MeV), and ^{214}Pb (0.35 MeV) are particularly clearly visible.

The intrinsic background curves of the detector and the emission spectrum of the **seawater** (see Figs. 1b, c) were obtained with this technique for Δt = 6 h. Figures 1e, f depict the results of laboratory experiments made with the same γ spectrometer in a ∿16 m³ tank with fresh water and a KCl solution, respectively; the experiments were made on a polygon for checking and calibrating of the Marine Hydrophysical Institute, Academy of Sciences of the Ukrainian SSR, with Δt = 5.5 h. The KCl concentration was equal to the KCl concentration of seawater with a salt concentration of 18‰. It follows from Fig. 1 that if according to ^{40}K the main γ emitter of **seawater** — the intrinsic detector background is relatively small, the background determined from the natural radionuclides (RaC and RaB) exceeds the seawater radiation by a factor of 8-10.

Our measurements allow the conclusion that with the BDEG-6931-20 scintillation block one can measure the specific activity of ^{40}K with an error of ∿0.7% and make relative measurements of the fluctuations of the specific activity of ^{214}Bi with an error of ∿2-5% for the 95% significance level. Obviously, the intrinsic detector background resulting from the decay products of ^{222}Rn—^{214}Bi and ^{214}Pb must be reduced to increase the range in which measurements on the radionuclides in field sites can be performed.

LITERATURE CITED

1. Yu. V. Sivintsev et al., At. Energ., 49, No. 1, 45 (1980).
2. E. L. Koval'chuk et al., At. Energ., 49, No. 4, 242 (1980).
3. R. A. Govorova et al., in: Single Crystals, Scintillators, and Organic Luminophors [in Russian], Vol. 2, No. 2, Cherkassian Polytechnical Institute, Cherkassy (1972), p. 221.
4. I. F. Lukashin et al., Morski Gidrofiz. Issled., No. 3, 156 (1979).

YIELD OF ^{118}Te (GENERATOR OF ^{118}Sb), ^{119m}Te, ^{121m}Te, ^{121}Te, AND ^{123m}Te IN Sn(α, xn) REACTIONS

P. P. Dmitriev and G. A. Molin   UDC 539.172.12

At the present time, in nuclear medicine and other fields of investigations, radionuclides which have an intense positron emission are widely used. Among the isotopes of antimony, ^{118}Sb (T$_{1/2}$ = 3.6 min, β$^+$ = 77.5%) is of interest and can be obtained as a result of the decay of ^{118}Te (T$_{1/2}$ = 6 days). In an experiment with seven values of α-particle energy for a thick target of tin, the yields of ^{118}Te and also ^{119m}Te, ^{121m}Te, ^{121}Te, and ^{123m}Te were measured, the presence of which determines the radioisotopic purity of ^{118}Te. ^{119m}Te (T$_{1/2}$ = 4.7 days) is also a generator of ^{119}Sb (T$_{1/2}$ = 38.1 h).

A stack of 99.9% pure metallic tin foils was irradiated in the deflected beam of α particles from the cyclotron in the Physicopower Institute. The average thickness of the foil was 40 mg/cm^2 and the thickness of each individual foil was determined with an error of 1.5%. To avoid adhesion of the tin foils during irradiation, aluminum with a thickness of 1.7 mg/cm^2 was placed between them. The integrated irradiation current of the stack of foils was measured by using a copper monitor foil. The stopping of the α particles was determined from data of [1]. The ratio of the measured activity for the whole stack of foils to the integrated irradiation current gives the yield of the isotope for the thick target, with maximum energy of the α particles. This same ratio for the stack, from which the first (in the path of the α-particle beam) tin foil is removed, determines the yield of the isotope for the next lower energy of the α particles, etc. The procedures for measuring the integrated dose and the activity of the nuclides are described in [2]. The radionuclides were identified by the half-life and the γ emission energy. When measuring the activity of the nuclides, the following values of the half-lives, energy, and γ emission quantum yield from [3] were used: ^{118}Te (6 days, γ = 511 keV, 155% — annihilation emission of ^{118}Sb), ^{119m}Te (4.7 days, γ = 1212.6 keV, 68%), ^{121m}Te (154 days, γ = 212.21 keV, 81.3%), ^{121}Te (17 days, γ = 573.08 keV, 79%), and ^{123m}Te (119.7 days, γ = 159 keV, 83.5%). When measuring the annihilation emission of ^{118}Sb, the annihilation emission of the other radionuclides in the foils were excluded or taken into account.

The results of the measurement of the yields are given in Table 1. The error of 14-17% of the values, shown in brackets, is due mainly to the systematic errors in determining the activity of the radionuclides and the integrated current. From the data of the table, curves of the isotope yields can be constructed as a function of the α-particle energy. There are no data whatsoever in the literature about the yields and cross sections of the reactions with the formation of ^{118,119m,121,123m}Te as a result of the irradiation of tin with α particles.

The yields of ^{125m}Te (T$_{1/2}$ = 58 days) and ^{127m}Te (T$_{1/2}$ = 109 days), which are formed by the reactions ^{122,124}Sn(α; n, 3n)^{125m}Te and ^{124}Sb(α; n)^{127m}Te, were not measured. In [4], the

TABLE 1. Yield of Tellurium Isotopes from the Irradiation of Tin with α Particles, kBq/μm Ar

Energy of particles, MeV	^{118}Te	^{119m}Te	^{121m}Te	^{121}Te	^{123m}Te
43,7 (0,5)	2340 (350)	2450 (370)	148 (23)	474 (72)	40,7 (6,2)
40,5 (0,5)	1970 (300)	1870 (270)	115 (18)	368 (56)	33,4 (5,1)
36,6 (0,5)	1470 (220)	1250 (190)	73,4 (11,8)	234 (35)	22,8 (3,6)
32,4 (0,6)	894 (135)	553 (84)	39,7 (6,8)	127 (21)	13,1 (2,1)
27,9 (0,7)	388 (58)	308 (48)	22,2 (3,7)	71 (12)	7,5 (1,3)
23,2 (0,7)	104 (17)	138 (24)	11,8 (1,9)	37,4 (5,8)	5,9 (1,1)
18,1 (0,8)	2,2 (0,4)	16,2 (2,8)	1,3 (0,3)	4,3 (0,8)	2,4 (0,5)

707

excitation functions of these reactions up to $E_\alpha = 39$ MeV were found, and we performed their integration over the mean free path and obtained the following values of the yields for a thick target with $E_\alpha = 39$ MeV: ^{125m}Te = 73 kBq/μm Ar and ^{127m}Te = 2.3 kBq/μm, Ar.

The data given in Table 1 show that the impurities ^{119m}Te, ^{121m}Te, and ^{123m}Te are large. The most efficient method for reducing them and increasing the yield of ^{118}Te is the use of enriched ^{116}Sn as a target, which can be seen **from the following**. ^{118}Te is formed by the reactions $^{115-118}$Sn(α; n, 2n. 3n. 4n) and the maximum yield for this α-particle energy is given by the reactions ^{116}Sn(α2n)^{118}Te and ^{117}Sn(α3n)^{118}Te. By using ^{116}Sn, the impurity ^{119m}Te is produced by the reaction ^{116}Sn(αn) and ^{117}Sn by the reaction ^{117}Sn(α2n) (sic). It is well known that in this mass region of nuclei, the cross section of reactions of the type (αn) is significantly lower than the cross sections of reactions of type (α2n), and consequently by using ^{116}Sn the impurity ^{119m}Te will be considerably lower. Calculations of the theoretical yield curves of ^{118}Te and ^{119m}Te in these reactions (the procedure of the calculations is similar to that given in [5]) allowed the following estimates to be made by comparison with natural tin, the use of ^{116}Sn (95% enrichment) **increases** the yield of ^{118}Te by a factor of 4.4, and the yield of ^{119m}Te is reduced by a factor of 2.6, which reduces the impurity ^{119m}Te by a factor of almost 12. In enriched ^{116}Sn, the content of other tin isotopes is reduced by a factor of approximately 15-20, by comparison with natural tin, and the impurities ^{121m}Te, ^{121}Te, ^{123m}Te, ^{125m}Te, and ^{127m}Te are reduced by a factor of 70-90, as the yield of ^{118}Te is increased by a factor of 4.4.

The impurity ^{119m}Te can be reduced significantly if a thin target of ^{116}Sn is used. It is noted in [5] that a thin rhodium target in the production of ^{105}Ag by the reaction ^{103}Rh(α, 2n) allows the impurity ^{106m}Ag, which is formed in the reaction ^{103}Rh(αn), to be reduced by a factor of six. It may be expected that a thin target of ^{116}Sn, e.g., will also reduce the impurity ^{119m}Te. Then, by comparison with the data of Table 1, the impurity ^{119m}Te is reduced by a factor of 70.

LITERATURE CITED

1. C. Williamson, J. Boujot, and J. Picard, Rap CEA-R 3042 (1966).
2. P. P. Dmitriev et al., At. Energ., **46**, No. 3, 185 (1979); **48**, No. 2, 122 (1980); **48**, No. 6, 402 (1980).
3. N. G. Gusev and P. P. Dmitriev, Quantum Emission of Radioactive Nuclides (Handbook) [in Russian], Atomizdat, Moscow (1977); Quantum Radiation of Radioactive Nuclides (A Data Handbook), Pergamon Press, Oxford, England (1979).
4. R. Hahn and J. Miller, Phys. Rev., **124**, 1879 (1961).
5. P. P. Dmitriev et al., At. Energ., **50**, No. 6, 418 (1981).

708

MEASUREMENT TECHNIQUES
Izmeritel'naya Tekhnika
Vol. 27, 1984 (12 issues) $520

MECHANICS OF COMPOSITE MATERIALS
Mekhanika Kompozitnykh Materialov
Vol. 20, 1984 (6 issues) $430

METAL SCIENCE AND HEAT TREATMENT
Metallovedenie i Termicheskaya Obrabotka Metallov
Vol. 26, 1984 (12 issues) $540

METALLURGIST
Metallurg
Vol. 28, 1984 (12 issues) $555

PROBLEMS OF INFORMATION TRANSMISSION
Problemy Peredachi Informatsii
Vol. 20, 1984 (4 issues) $420

PROGRAMMING AND COMPUTER SOFTWARE
Programmirovanie
Vol. 10, 1984 (6 issues) $175

PROTECTION OF METALS
Zashchita Metallov
Vol. 20, 1984 (6 issues) $480

RADIOPHYSICS AND QUANTUM ELECTRONICS
Izvestiya Vysshikh Uchebnykh Zavedenii, Radiofizika
Vol. 27, 1984 (12 issues) $520

REFRACTORIES
Ogneupory
Vol. 25, 1984 (12 issues) $480

SIBERIAN MATHEMATICAL JOURNAL
Sibirskii Matematicheskii Zhurnal
Vol. 25, 1984 (6 issues) $625

SOIL MECHANICS AND FOUNDATION ENGINEERING
Osnovaniya, Fundamenty i Mekhanika Gruntov
Vol. 21, 1984 (6 issues) $500

SOLAR SYSTEM RESEARCH
Astronomicheskii Vestnik
Vol. 18, 1984 (6 issues) $365

SOVIET APPLIED MECHANICS
Prikladnaya Mekhanika
Vol. 20, 1984 (12 issues) $520

SOVIET ATOMIC ENERGY
Atomnaya Energiya
Vols. 56-57, 1984 (12 issues) $560

SOVIET JOURNAL OF GLASS PHYSICS AND CHEMISTRY
Fizika i Khimiya Stekla
Vol. 10, 1984 (6 issues) $235

SOVIET JOURNAL OF NONDESTRUCTIVE TESTING
Defektoskopiya
Vol. 20, 1984 (12 issues) $615

SOVIET MATERIALS SCIENCE
Fiziko-khimicheskaya Mekhanika Materialov
Vol. 20, 1984 (6 issues) $445

SOVIET MICROELECTRONICS
Mikroelektronika
Vol. 13, 1984 (6 issues) $255

SOVIET MINING SCIENCE
Fiziko-tekhnicheskie Problemy Razrabotki Poleznykh Iskopaemykh
Vol. 20, 1984 (6 issues) $540

SOVIET PHYSICS JOURNAL
Izvestiya Vysshikh Uchebnykh Zavedenii, Fizika
Vol. 27, 1984 (12 issues) $520

SOVIET POWDER METALLURGY AND METAL CERAMICS
Poroshkovaya Metallurgiya
Vol. 23, 1984 (12 issues) $555

STRENGTH OF MATERIALS
Problemy Prochnosti
Vol. 16, 1984 (12 issues) $625

THEORETICAL AND MATHEMATICAL PHYSICS
Teoreticheskaya i Matematicheskaya Fizika
Vol. 58-61, 1984 (12 issues) $500

UKRAINIAN MATHEMATICAL JOURNAL
Ukrainskii Matematicheskii Zhurnal
Vol. 36, 1984 (6 issues) $500

Send for Your Free Examination Copy

RUSSIAN JOURNALS IN THE PHYSICAL AND MATHEMATICAL SCIENCES

AVAILABLE IN ENGLISH TRANSLATION

ALGEBRA AND LOGIC
Algebra i Logika
Vol. 23, 1984 (6 issues) $360

ASTROPHYSICS
Astrofizika
Vol. 20, 1984 (4 issues) $420

AUTOMATION AND REMOTE CONTROL
Avtomatika i Telemekhanika
Vol. 45, 1984 (24 issues) $625

COMBUSTION, EXPLOSION, AND SHOCK WAVES
Fizika Goreniya i Vzryva
Vol. 20, 1984 (6 issues) $445

COSMIC RESEARCH
Kosmicheskie Issledovaniya
Vol. 22, 1984 (6 issues) $545

CYBERNETICS
Kibernetika
Vol. 20, 1984 (6 issues) $445

DIFFERENTIAL EQUATIONS
Differentsial'nye Uravneniya
Vol. 20, 1984 (12 issues) $505

DOKLADY BIOPHYSICS
Doklady Akademii Nauk SSSR
Vols. 274-279, 1984 (2 issues) $145

FLUID DYNAMICS
Izvestiya Akademii Nauk SSSR,
Mekhanika Zhidkosti i Gaza
Vol. 19, 1984 (6 issues) $500

**FUNCTIONAL ANALYSIS AND
ITS APPLICATIONS**
Funktsional'nyi Analiz i Ego Prilozheniya
Vol. 18, 1984 (4 issues) $410

GLASS AND CERAMICS
Steklo i Keramika
Vol. 41, 1984 (6 issues) $590

HIGH TEMPERATURE
Teplofizika Vysokikh Temperatur
Vol. 22, 1984 (6 issues) $520

HYDROTECHNICAL CONSTRUCTION
Gidrotekhnicheskoe Stroitel'stvo
Vol. 18, 1984 (12 issues) $385

INDUSTRIAL LABORATORY
Zavodskaya Laboratoriya
Vol. 50, 1984 (12 issues) $520

**INSTRUMENTS AND
EXPERIMENTAL TECHNIQUES**
Pribory i Tekhnika Éksperimenta
Vol. 27, 1984 (12 issues) $590

**JOURNAL OF APPLIED MECHANICS
AND TECHNICAL PHYSICS**
Zhurnal Prikladnoi Mekhaniki i Tekhnicheskoi Fiziki
Vol. 25, 1984 (6 issues) $540

JOURNAL OF APPLIED SPECTROSCOPY
Zhurnal Prikladnoi Spektroskopii
Vols. 40-41, 1984 (12 issues) $540

JOURNAL OF ENGINEERING PHYSICS
Inzhenerno-fizicheskii Zhurnal
Vols. 46-47, 1984 (12 issues) $540

JOURNAL OF SOVIET LASER RESEARCH
A translation of articles based on the best Soviet research in the field of lasers
Vol. 5, 1984 (6 issues) $180

JOURNAL OF SOVIET MATHEMATICS
A translation of Itogi Nauki i Tekhniki and Zapiski Nauchnykh Seminarov Leningradskogo Otdeleniya Matematicheskogo Instituta im. V. A. Steklova AN SSSR
Vols. 24-27, 1984 (24 issues) $1035

LITHOLOGY AND MINERAL RESOURCES
Litologiya i Poleznye Iskopaemye
Vol. 19, 1984 (6 issues) $540

LITHUANIAN MATHEMATICAL JOURNAL
Litovskii Matematicheskii Sbornik
Vol. 24, 1984 (4 issues) $255

MAGNETOHYDRODYNAMICS
Magnitnaya Gidrodinamika
Vol. 20, 1984 (4 issues) $415

MATHEMATICAL NOTES
Matematicheskie Zametki
Vols. 35-36, 1984 (12 issues) $520